A generalized damage parameterization within the Maxwell Elasto-Brittle rheology: applications to ice fractures and ice arches in landfast ice simulations

Mathieu Plante

Department of Atmospheric and Oceanic Sciences
McGill University, Montréal
Québec, Canada
September 2020

A thesis submitted to McGill University in partial fulfillment of the requirements of the degree of Doctor of Philosophy

Acknowledgements

Behind the completion of this thesis stands an army of colleagues, family and friends who supported me throughout the years. First, I would like to thank my supervisor Prof. Bruno Tremblay for the many discussions, debates, experiences and arguments, all of which necessary for the advancement of this project. Thank you also for believing that experiences are the foundations of expertise: it really made me grow as a researcher. I also want to thank Martin Losch and Jean-François Lemieux for your guidance, support and great advises during my stays in your institutions, and for being much needed motivators and confidence builders throughout the last few years. I am also grateful to the ArcTrain International Training Program for providing travel support and training experiences that I trust will benefit me throughout my future career.

I want to thank many colleagues at McGill for all the conversations and helpful meetings: James Williams, Yukie Hata, Line bourdages, Charles Brunette, Damien Ringeisen and all other members of the Arctic research group. A particular thank you to Amélie Bouchat for being with me every single steps of the way. This work would not have been possible without our science discussions, numerous coffees and your undying moral support. I also want to thank all the ArcTrain students for being such a supportive community, and all the administrative and technical staff at McGill for you help over the years.

The Ph.D. years are full of challenges, and those who bear the grunt of it is our family and close friends. Mom, dad, I am sitting on your shoulders, and in dept to you for teaching me not to focus on failures but on lessons learned. Without this resilience, this thesis would simply not be. Caroline, Carl, Mirella, Cassandra, and so many others: thank you for you unconditional support through these years.

Finally, I would liked to thank the Fonds de recherche du Québec – Nature et technologies (FRQNT) for financial support received during the course of this work. This work is also a contribution with Québec-Océan.

Abstract

In many regions of the Arctic, the landfast ice cover is consolidated by the jamming of ice floes through narrow passages. The resulting ice arches determine the location of semi-permanent polynyi that are key for the Arctic climate, local biology, air-sea interactions and vertical mixing in the ocean. Forecasting their location, formation and break up date however represents a challenge for the standard Viscous-Plastic (VP) sea-ice models commonly used in the community. Recently, new rheologies are being developed using alternative fracture mechanics with the goal of improving the simulated sea-ice deformations. The influence of the different fracture parameterizations on the landfast ice and the formation of ice arches however remains unclear. To address this question, the material behaviour and mechanical strength simulated by a new fracture parameterization, the Maxwell Elasto-Brittle rheology and its damage parameterization, are analysed in the context of ideal landfast-ice simulations and compared with results from the standard VP model.

First, the formation and break-up of landfast ice is observed using satellite imagery to document the formation of ice arches in different marginal seas. The formation of extensive landfast ice cover is shown to depend on the formation of ice arches between areas where ice becomes grounded on the shallow shoals. The ice grounding is also shown to occur earlier in the fall (October-November) and to persist long after the landfast ice break-up, calling for modifications to the ice thickness-based relationship that determines the grounding in the ice grounding parameterization.

Second, the Maxwell Elasto-Brittle (MEB) rheology and its damage parameterization are implemented in the Eulerian, Finite Difference framework commonly used in classical Viscous-Plastic models. The role of the damage parameterization in the formation and collapse of landfast ice in a narrow channel is investigated. Ice bridge simulations are compared with observations to derive constraints on the mechanical properties of sea ice. Landfast channel conditions observed in the Arctic are best simulated using a material cohesion in the range of 5-10 kN/m. Results show that an ice arch easily forms downstream of the channel

in short-term simulations. When its collapses, no arches are formed upstream of the channel. Instead, fracture lines are formed with an orientation that deviates from the Mohr-Coulomb theory. The jamming of ice upstream of the channel in the long term is complicated by the growth of residual errors associated with the damage parameterization during ridging.

Third, a general stress correction scheme is developed in an attempt to reduce the growth of the residual errors in the damage parameterization. A decohesion stress tensor is introduced in order for the super-critical stresses to be corrected back to the yield curve following any path in the stress invariant space. This reduces the growth of residual errors such that longer-term simulations retain their symmetry and limit the development of random fractures. Results show that the angle of fracture in uni-axial loading experiments is sensitive to the magnitude of the decohesion stress tensor. The simulated fracture orientations are in good agreement with observed values when the stress correction follows a line perpendicular to the yield curve. The large deformations simulated by the MEB model are shown to be viscous in nature, to occur post-fractures, and to be dissociated from the fracture process itself. This is an important difference with classical VP models and results in the amount of divergence and shear deformations along the fracture plane to be non-sensitive to the choice of stress correction path.

Finally, we compare the landfast ice fractures simulated by the VP rheology and the generalized MEB rheology. In simple 1D simulations, the different rheologies are shown to yield similar creep behaviour in the landfast ice regime and transition to large deformation rates when the ice fractures. The ideal ice bridge simulations are revisited in longer-term experiments, in which the formation of ice arches upstream of the channel is shown to be sensitive to the yield parameters but not on the fracture parameterization. The large deformation simulated within the fractures are however different, producing smoother and linear ridges in the VP model but non-linear concave ridges with larger local variations in the MEB model. Both the VP and MEB rheology produce stable ice arches upstream of a channel when the (thickness dependent) compressive and shear strength of ice can sustain the external forcing everywhere upstream of the channel, but only if the ice in the channel downstream flows freely. We also find that the ice arch stability is not influenced by the maximum viscosity in the VP model, contrary to what has been previously reported for the VP model.

Résumé

Dans plusieurs régions côtières de l'Arctique, la glace de mer est immobilisée par la formation d'embâcles dans des chenaux étroits. Ces embâcles en forme d'arche déterminent l'emplacement de polynies semi-permanentes qui affectent de manière importante le climat Arctique, la biologie marine, les interactions entre l'air et l'océan, ainsi que le mélange vertical dans l'océan. La prédiction de leur formation, de leur emplacement et de leur débâcle représente toutefois un défi pour les modèles de glace de mer qui utilisent en majorité la rhéologie Visqueuse-Plastique (VP). Récemment, de nouvelles rhéologies ont été développées avec des paramétrisations de fracture alternatives afin de mieux représenter les déformations dans le couvert de glace. L'impact de ces nouvelles paramétrisations sur la représentation de la glace de rive et sur la formation d'arches dans les modèles reste cependant à déterminer. À cette fin, le comportement et la force mécanique de la glace de mer simulée par une de ces nouvelles paramétrisations, la rhéologie Maxwell-Elasto Brittle (ou fragile, MEB), sont analysés dans le contexte de simulations idéalisées et comparés à des résultats provenant d'un modèle VP standard.

En premier lieu, la formation et la débâcle de la glace de rive est observée à l'aide d'images satellitaires afin de documenter la formation d'arches dans différentes régions en marge de l'Arctique. Il est montré que le couvert de glace de rive dépend de la formation d'arches entre des endroits où la glace de mer est ancrée sur des hauts-fonds. L'ancrage de la glace de mer est observé tôt en automne (october-novembre) et persiste longtemps après la débâcle de glace de rive. La paramétrisation simulant l'ancrage de glace dans les modèles devrait donc être modifiée au niveau de la relation entre l'ancrage de la glace et l'épaisseur moyenne du couvert de glace.

En second lieu, la rhéologie MEB et sa paramétrisation du dommage sont implémentées dans le modèle de glace de McGill, dans un schéma numérique Eulérien par Différences Finies tel que couramment utilisé pour les modèles VP. Le rôle de la paramétrisation du dommage dans la formation et la débâcle de la glace de rive dans un chenal est étudié à

l'aide de simulations de pont de glace idéalisées. Les résultats sont comparés aux ponts de glace observés afin d'estimer les propriétés matérielles de la glace de mer. Les conditions observées sont les mieux représentées par le modèle MEB en utilisant une cohésion de 5-20 kN/m. Les résultats démontrent que des arches de glaces se forment facilement en aval d'un chenal dans des simulations à courts termes. En amont du chenal, il se forme plutôt des lignes de fracture dont l'orientation ne concorde pas avec la théorie de Mohr-Coulomb. La formation d'arches de glace en amont d'un chenal à plus long terme est compliquée par la croissance d'erreurs numériques résiduelles causées par la paramétrisation du dommage, spécifiquement lors de la correction des contraintes super-critiques qui s'opère lors de la formation de crêtes de pression.

En troisième lieu, une méthode generalisée pour la correction des contraintes super-critiques est développée afin de réduire la croissance des erreurs résiduelles associée à la paramétrisation du dommage. Un tenseur de contraintes de décohésion est introduit afin de permettre n'importe quel chemin de correction lorsque les contraines super-critiques sont ramenées vers la courbe de contraintes critiques. Ceci réduit l'erreur des contraintes corrigées et permet de prolonger les simulations sur de plus longues échelles de temps. Les résultats démontrent que l'orientation des fractures simulées dans des expérience de chargement uni-axial est sensible à la magnitude du tenseur de stress de décohésion. L'orientation des fractures représente bien les valeurs observées lorsque le chemin de correction des contraintes super-critiques est à 45 degrés dans l'espace des invariants du tenseur des contraintes. Les taux de déformation en divergence et en cisaillement le long des lignes de fractures ne sont pas affectés par le tenseur des contraintes de décohésion, ce qui indique que la nature des déformations post-fractures est dissociée du processus de développement des fractures lui-même, ce qui représente une différence importante avec les modèles standards VP.

Finalement, la déformation de la glace de rive et la formation d'arches en amont d'un chenal simulées par la rhéologie VP et par la rhéologie MEB généralisée (MEBg) sont comparées. Dans des simulations à 1D, il est démontré que les différentes relations constitutives

résultent à un flutage similaire dans la glace de rive. Lorsque la glace se brise, les différences entre les simulations VP et MEB sont faibles, à l'exception du profil des crête simulées qui est linéaire dans les simulations VP et polynomial dans le cas des simulations MEB. Les simulations de ponts de glaces sont aussi revisitées dans le cadre de simulation à plus long-terme, dans lesquelles il est démontré que la formation d'arches en amont d'un chenal dépend de la courbe des contraintes critiques et non de la manière dont la fracture est paramétrisée. Les deux rhéologies présentent des arches similaires lorsqu'elles sont utilisées avec des propriétés mécaniques similaires. Les arches se forment lorsque les contraintes en compression partout en amont du chenal sont inférieures à la force de la glace en compression (qui grandit avec l'épaisseur de la glace) tandis que la glace à l'intérieur du chenal est en dérive. Il est aussi démontré que la stabilité de la glace de rive dans le modèle VP n'est pas sensible à la valeur de viscosité maximale qui détermine son flutage, contrairement à ce qui a précédemment été documenté.

Contribution of Authors

This thesis is an *article-based* thesis and is composed of four main chapters, each representing an article published, submitted or soon to be submitted to a peer review journal. These chapters are preceded by a general introduction and followed by a conclusion and appendix. The first article (Chapter 2) was redacted with the collaboration of Bruno Tremblay. This manuscript is not yet ready but planned for submission in a peer review journal. The second article (Chapter 3) was published as a highlight paper in The Cryosphere (doi:10.5194/tc-14-2137-2020) in collaboration with Bruno Tremblay (my supervisor), Martin Losch (from the Alfred Wegener Institüt, Bremen, Germany) and Jean-François Lemieux (from Environment and Climate Change Canada, Montréal). The third article (Chapter 4) was written with the collaboration of Bruno Tremblay and is under revision in the journal The Cryosphere. The fourth article (Chapter 4) was redacted with the collaboration of Bruno Tremblay and will soon be submitted to the journal The Cryosphere.

Throughout this work, I coded the sea ice rheology, ran all the simulations, analyzed results and led the writing of each chapters of this thesis. My supervisor B. Tremblay participated in regular discussions during the course of my Ph.D. and edited each chapters of this thesis. The other co-authors of the second chapter, Martin Losch and Jean-François Lemieux, participated in regular discussions during my stays in their respective institutions. They both helped during the implementation of the MEB rheology and edited the second chapter of this thesis.

Statement of Originality

The following elements of the thesis are original scholarships and represent original contributions to scientific knowledge:

- The role of ice arching in the formation of landfast ice across the Arctic is characterised based on satellite imagery. In particular, we show that the large landfast ice cover of the Siberian Arctic depends on the formation of ice arches between grounded ice ridges. These observations suggest that in sea-ice models, the grounding is underestimated early in the season but overestimated in winter, and calls for the use of a different relation between the ice thickness and the grounding parameters.

- The MEB rheology is implemented using the framework of a VP rheology in the McGill sea-ice model. This is the first implementation of the MEB rheology and its damage parameterization using a Finite Difference framework, the most commonly used in climate and coupled models. This provides a base for future implementations in community-shared sea-ice models such as CICE or MITgcm, a necessary step for this rheology to become a robust alternative to standard plastic-based models. It also allows for a comparison with other rheologies using a common numerical approach.

- The role of the damage parameterization in the formation and collapse of ice arches and ice bridges in a narrow channel is defined, and used to derive constraints on the mechanical properties of landfast sea ice. In particular, we find that the landfast ice inside the channel is sustained by the formation of an ice arch downstream, until the maximum shear stress along the channel coast exceeds the material cohesion of sea ice. Typical ice bridges observed in the Arctic are best simulated using a material cohesion in the range of 5-10 kN m^{-2}.

- We show that the stress correction scheme in the standard damage parameterization increases the residual errors during ridging. The errors are integrated in the solution and affect negatively the accuracy of longer-term simulations that include post-fracture deformations. We derive a mathematical expression that quantifies this error growth to better define the residual errors in the model when using the damage parameterization.

- A generalized stress correction scheme is developed to reduce the growth or errors by the damage parameterization. The scheme uses a decohesion stress tensor to bring the stress to the yield curve following any stress correction path. This reduces the errors in the model and allows to produce longer-term simulations including post-fracture deformations.

- We define the influence of a decohesion stress tensor on the simulated angle between intersecting lines of fracture in uni-axial compression experiments. The decohesion stress tensor is used to improve the simulated angles of fracture in the MEB model, which are too large when using the standard damage parameterization. The angles of fracture are closer to observations when the generalized stress correction scheme is used with a stress correction path that is normal to the yield curve in the stress invariant space.

- In uni-axial loading experiments, we demonstrate that the production of large deformations in the generalized MEB rheology mostly occurs post fracture and is dissociated from the fracturing process itself. This is a significant difference from the standard VP rheology in which the large deformations only occur when the ice is breaking. In particular, this implies that the stress correction scheme does not influence the type of deformation in the fractures and cannot represent granular behaviour such as dilatancy.

- We use the VP and the generalized MEB model, implemented on the same numerical platform, in 1D uni-axial experiments to document the influence of the fracture parameterization on the simulated deformations. We show that the both models present similar creep behaviour in the landfast ice regime with a similar transition to large deformation rates when the ice fractures. Overall, the use use of a normal flow rule results in smoother (linear) deformations in the VP model, while the non-linear post-fracture viscous relationship causes non-linear deformations with larger local variations in the MEB model.

- We use the VP and generalized MEB rheologies, implemented on the same numerical platform, to investigate the influence of the fracture mechanics on the formation of ice arches that form post-fracture upstream of the channel. We show that the fractures are similar when both rheologies use similar strength parameters and that the inter-model differences are mostly related to the use of different yield criterion and to post-fracture deformations.

- We show that the fractures and the plastic deformations in the VP model are not sensitive to changes in the maximum viscosity defining the transition between the viscous and plastic regimes, contrary to what was previously reported.

- We document the necessary conditions for ice arches to form upstream of a channel in sea-ice models. We find that the ice arches are formed when the material strength exceeds the compression forces upstream of the channel, while the ice in the channel downstream is drifting. In the case of a too-weak ice cover, the first condition can be achieved in the long term with sufficient ridging.

- We show that the tendency of the MEB rheology to produce ice arches downstream of a channel is related to the large post-fracture deformations within the channel providing large ridges with sufficient strength to hold an ice arch within the channel. This is contrary to observations in which the ice arches are usually found upstream of narrow passages.

Contents

List of Figures

List of Tables

Chapter 1

Introduction

The dramatic decline of the Arctic sea-ice extent is emblematic of our changing climate. In the next decades, the sea ice cover is expected to transition from a perennial to a seasonal ice cover, with large implications for the global climate [*Wang and Overland*, 2012; *Vihma*, 2014] and human activities including navigation and tourism [*Pizzolato et al.*, 2016; *Aksenov et al.*, 2017]. Navigation in ice-infested waters yet represents a risk, in particular close to shores where the sea-ice drift interacts with the coastline, creating high sea-ice pressure on vessels [*Mussells et al.*, 2017]. This is especially a concern in the Northwest Passage and Canadian waters, where the presence of sea ice is expected to persist farthest in the future [*Laliberté et al.*, 2016].

In winter, much of the coastal waters become non-navigable due to the presence of landfast (or land-locked) sea ice. The term landfast ice refers to the immobile sea ice that is attached to the coast, acting like an extension of the land, resisting the surface forcing from winds and ocean currents (Eg. see Fig. 1.1a, in the East Greenland sea). In the Arctic the landfast ice cover starts to form in the late fall (October-Novembre), reaches its maximum in early spring (March-April), and breaks-up in June or July [*Yu et al.*, 2014]. At its peak, it covers most channels of the Canadian Arctic Archipelago (CAA) [*Galley et al.*, 2012] and is found along the entire Arctic coastlines [*Yu et al.*, 2014, , see also Fig. 1.1b]. Its offshore extent presents large regional differences, varying from tens of kilometers along the Alaskan and Chukchi coasts [*Mahoney et al.*, 2007, 2014], to hundreds of kilometers offshore in the Siberian peripheral seas [*Reimnitz et al.*, 1995; *Eicken et al.*, 2005; *Haas et al.*, 2005; *Yu et al.*, 2014; *Selyuzhenok et al.*, 2017]. Its presence exerts a significant influence on shore processes and protects the coast from erosion [*Barnes et al.*, 1984]. Seasonally, the formation of landfast ice causes fresh water retention in the Arctic estuaries, influencing the salinity distribution in the marginal seas [*Macdonald*, 2000; *Dmitrenko et al.*, 2005; *Eicken et al.*, 2005], and its melt in summer mixes with the freshwater coming from river discharges [*Bareiss et al.*, 1999; *Eicken et al.*, 2005; *Dmitrenko et al.*, 2005]. Adjacent to the landfast ice edge, recurrent regions of open water called polynya (or flaw lead) form as the wind pushes the pack-ice off or along-shore, contributing to a large portion of the Arctic winter ocean-atmosphere heat fluxes [*Martin and Cavalieri*, 1989; *Dethleff et al.*, 1998]. The presence of landfast ice is also key to marine biology [*Carmack and Macdonald*, 2002], its export being a significant source of offshore sediment transport [*Nürnberg et al.*, 1994; *Pfirman et al.*, 1997].

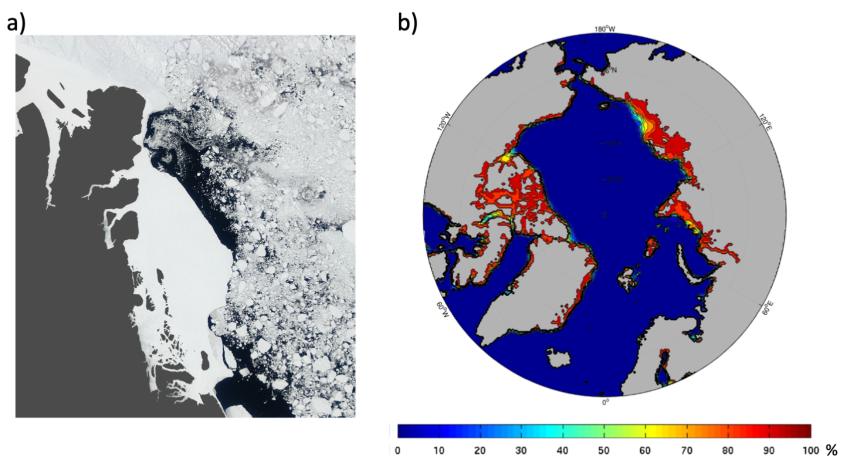

Figure 1.1: a) Greenland sea Landfast ice (June 15th 2014), seen on corrected reflectance imagery from the Moderate Resolution Imaging Spectroradiometer (MODIS) satellites. b) Annual percent probability of landfast ice presence in the Arctic, from the the National Ice Center ice charts in the 1976-2007 period.

The formation of landfast ice is often associated with the grounding of ice keels on the ocean floor. Early observations on the Alaskan coast show evidence of this grounding, such as seabed gouging by large ice keels in the thick multi-year ice [*Barry et al.*, 1979; *Reimnitz et al.*, 1978a]. As the sea ice ridges drift along the shores, the 15-20m isobath becomes a location where successive grounding occurs, effectively creating a barrier (called stamukhi) that protects the shoreward sea ice from the offshore dynamics [*Reimnitz et al.*, 1978b; *Mahoney et al.*, 2007; *Selyuzhenok et al.*, 2017]. This process has since then been documented in many studies in the Beaufort sea [*Mahoney et al.*, 2007, 2014], the Laptev sea [*Haas et al.*, 2005; *Selyuzhenok et al.*, 2017] and the Kara sea [*Divine et al.*, 2004]. The role of grounding has however been disputed in the Siberian Arctic (e.g. Laptev sea), where most of the ice cover is composed of low-salinity first year ice with a surface smoothness that is incompatible with ice grounding [*Reimnitz et al.*, 1994]. Zones of heavy ridging and deformations have however been observed locally in more recent studies [*Haas et al.*, 2005; *Selyuzhenok et al.*, 2017]. In other areas, such as in the Kara and East Siberian seas, the landfast ice cover extends to water depths that are too deep for the grounding of sea ice [*Yu et al.*, 2014]. In the Canadian Arctic Archipelago, the presence of landfast ice is rather associated with the damming of ice floes in narrow passages, creating ice arches (see Fig. 1.2) that can sustain large surface forcings in a manner akin to the arches under a roman bridge [*Melling*, 2002; *Vincent*, 2019]. This behaviour is usually associated with granular materials and to the mechanical strength of sea ice [*Sodhi*, 1997; *Hibler et al.*, 2006]. Ice arches are found in many locations of the CAA [*Melling*, 2002, , see also Fig. 1.2a], with the most well studied located in the Nares Strait [Fig. 1.2b, *Mysak and Huang*, 1992; *Dumont et al.*, 2008; *Ryan and Münchow*, 2017; *Moore and McNeil*, 2018; *Vincent*, 2019].

In sea-ice models, landfast ice has long been under-represented or entirely missing except in the CAA, where land on all sides allows for a stable land-locked ice cover via the compressive strength of sea ice. The absence of landfast ice in dynamical sea-ice models is a major cause of uncertainties in the simulated ice thickness fields, ocean currents, halocline stability

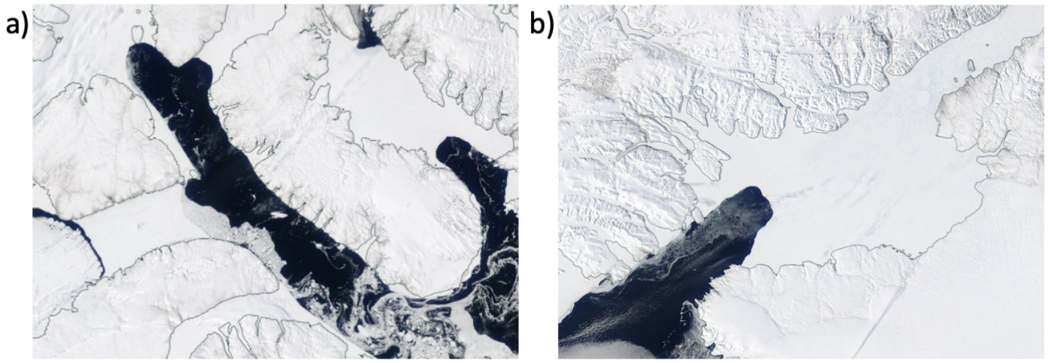

Figure 1.2: Landfast ice arches from MODIS satellite corrected reflectance imagery. a) in the western Canadian Arctic Archipelago (CAA), May 24th 2015. b) In the Nares strait, May 5th 2016.

and salinity distributions [*Johnson et al.*, 2012; *Itkin et al.*, 2015]. Because of this shortcoming, the study of landfast ice in models was usually done by using a landfast ice mask based on either landfast ice observations [*Ernsdorf et al.*, 2011; *Rozman et al.*, 2011], landfast ice climatologies [*Itkin et al.*, 2015] or bathymetric criteria [*Wang et al.*, 2014; *Lieser*, 2004].

The dynamical representation of landfast ice involves the rheology, which determines the material deformation resulting from an applied stress. The rheology includes a material constitutive relation that relates the internal stresses to deformations (elastic) or deformation rates (viscous or plastic), and a yield criterion that determines the maximum stresses for the fracture of ice. Most dynamical models used in the sea ice community are based on the standard Viscous-Plastic (VP) rheology of [*Hibler*, 1979]. In this model, the ice presents negligible viscous creep flow under sub-critical stresses, and large deformation rates governed by a normal flow rule under critical stresses (i.e. on the yield curve). The transition between the viscous and plastic regimes is determined by writing the viscous coefficient as an inverse function of the strain rates when the stress state is critical, allowing for large plastic strain rates. When the deformation rates tend to zero, the viscosity is capped to a maximum value that determines the creep flow in sub-critical stress states [*Beatty and Holland*, 2010]. In its standard formulation, the yield curve takes the shape of an ellipse in the stress invariant space, with zero tensile strength and limited shear strength (set by the ellipse eccentricity).

In the standard VP rheology, the formation of ice arches in narrow channels such as in the Nares Strait are commonly formed by increasing the tensile or shear strength in the yield curve [*Dumont et al.*, 2008; *Beatty and Holland*, 2010; *Olason*, 2016; *Lemieux et al.*, 2016]. Changing the mechanical strength of sea ice alone however is not sufficient to simulate a realistic landfast ice cover in most of the Arctic peripheral seas (Beaufort sea, East Siberian sea, Laptev sea). In these regions, an additional basal stress term to represent ice grounding in the momentum equation is necessary for realistic landfast ice simulations [*Lemieux et al.*, 2015]. The basal stress is parameterized as a function of the mean ice thickness and the local bathymetry. Combining the grounding parameterization with the addition of tensile strength leads to a simulated maximum landfast ice extent in good agreement with observations in most of the Arctic [*Lemieux et al.*, 2016]. Difficulties however remain in simulating the timing of the landfast ice onset and break up, as well as in the variability in areas where landfast ice is less stable, such as in the Kara Sea and in sections of the CAA [*Lemieux et al.*, 2016]. Different studies also present different ranges of cohesion or tensile strength values appropriate for a realistic landfast ice cover [*Dumont et al.*, 2008; *Olason*, 2016; *Lemieux et al.*, 2016]. *Olason* [2016] also reported a sensitivity of the landfast ice cover on the set maximum viscosity, which was not reported in [*Lemieux et al.*, 2016]. These issues raise the question as to whether the landfast ice cover is influenced by the numerical implementation of sea-ice models.

In the last decades, the establishment of sea-ice deformation statistics (e.g. the presence of Linear Kinematic Features, their density, angle and width) was made possible by high-resolution observations from satellites such as RadarSat [*Kwok et al.*, 2008; *Bouchat and Tremblay*, 2017; *Hutter et al.*, 2019]. While the VP models (and modifications thereof) are able to represent these features [*Bouchat and Tremblay*, 2020; *Hutter et al.*, 2018; *Ringeisen et al.*, 2019], a number of new rheologies have been developed in an attempt to improve the representation of sea-ice deformation statistics [*Girard et al.*, 2011; *Rampal et al.*, 2016, 2019], the brittle character of the ice fractures observed in laboratory [*Schreyer et al.*, 2006; *Sulsky et al.*, 2007; *Dansereau et al.*, 2016] or the orientation of LKFs in the field [*Wilchinsky and Feltham*, 2004]. In particular, a damage parameterization inspired from rock mechanics and seismology models [*Amitrano et al.*, 1999; *Amitrano and Helmstetter*, 2006] was developed for the large scale simulation of sea ice as a part of the Elasto-Brittle rheology [*Girard et al.*, 2011; *Bouillon and Rampal*, 2015; *Rampal et al.*, 2016]. This parameterization uses the concept of material memory of past fractures in the sea ice (or damage) to influence the future deformations and the propagation of the fractures in space. A Maxwell viscosity term was later added in the rheology, [the Maxwell Elasto-Brittle (MEB) rheology, *Dansereau et al.*, 2016], to include post-fracture permanent deformations. In the neXtSIM model, the MEB rheology was shown to reproduce well the localisation of the sea-ice fractures in space and time [*Rampal et al.*, 2019], and is considered a promising rheology for the large-scale simulation of sea ice.

The MEB rheology however remains relatively new and has not been used as thoroughly as the plastic rheologies, which is used in most operational and climate models since the late seventies. In ideal experiments, the MEB rheology has been shown to easily produce ice arches in narrow channels such as the Nares strait [*Dansereau et al.*, 2017], and to produce granular fracture angles in uniaxial loading experiments [*Dansereau et al.*, 2019]. However, the ice arches have a tendency to stabilise downstream of narrow channels (hereafter referred to as "downstream ice arch"), as opposed to upstream (hereafter referred to as "upstream ice arch") as seen in observations and simulated by plastic models. In uni-axial loading experiments, the fracture orientation simulated by the MEB rheology [$\theta = 35 - 55°$, *Dansereau et al.*, 2019] also differs from the values predicted by granular theories [$\theta = 25 - 45°$, *Bardet*, 1991] and in the fields [$\theta = 20 - 45°$ *Hutter et al.*, 2019]. While these results indicate important differences with the classical plastic rheologies, the EB and MEB rheologies were up until now implemented using Lagrangian advection schemes and/ or Finite Element Methods, instead of the more common Eulerian Finite-Difference methods. It therefore remains unclear whether the different fracture statistics result from the different physics or the different numerics.

Thesis objectives

In this thesis, we investigate the influence of the rheology on the simulated ice fractures and on the formation of ice arches, using ideal sea ice simulations. The goal is to identify the rheology and strength parameters needed to improve the representation of landfast ice in sea-ice models. We also want to further our understanding of the simulated material behaviour resulting from different fracture physics. This is a necessary step to guide future model development in the context of the increasing demand for high resolution forecasts, in which the fracture definition and physics are important.

In Chapter 2, we present satellite observations to characterize the role of ice arching in the formation of a landfast ice cover in the Laptev Sea, the Kara Sea and the CAA. The goal is to define a landfast ice formation process that can be applied across the Arctic and that integrates seemingly contradicting observations previously reported in the literature. This is a necessary step to identify the model components that need to be improved to better reproduce the onset and break up of the landfast ice and its inter-annual variability. We find that the extensive landfast ice cover of the Siberian Arctic is formed by an inter-play between ice grounding and ice arching, with larger ice arches corresponding to sections of higher landfast ice variability. We also show that the ice grounding occurs early in the season over shallow shoals, which later provide anchor points for ice arches to form. This process explains the presence of landfast ice over deep waters and is in accord with regional differences in the bathymetry and land morphology.

In Chapter 3, we present the implementation of the MEB rheology and its damage parameterization onto the Finite Difference framework of the McGill Sea Ice Model (McGill SIM). This is the first implementation of this rheology on the framework commonly used in coupled models, allowing for a comparison of the model physics independently from the numerics. The goal of this chapter is to test our implementation in the context of ideal ice arch simulations and to determine the material strength parameters that correspond to the ice arches commonly observed in the Arctic. We find that using a material cohesion in the range of 5-10 kN/m best represents the observed conditions, and that the rheology easily forms ice arches downstream of the channel in short-term simulations. We also find that the formation of other ice arches upstream of the channel in the long term is complicated by a fast residual error growth during ridging, originating in the stress correction scheme in the damage parameterization. In the short term, fracture lines along which ridging occurs are created upstream of the channel, forming wedges of landfast ice between which the ice is drifting. The orientation of the fracture lines also differs from that predicted by the Mohr-Coulomb theory.

In Chapter 4, we present a general stress correction scheme that reduces the growth rate of the residual errors in the damage parameterization, and evaluate its influence in the context of uni-axial loading experiments. The goal is to reduce the numerical growth of the residual errors in order to compare the physics with other rheologies in longer-term simulations, and to identify whether modifying the stress correction scheme can bring the fracture orientation closer to the observations. Our generalized stress correction scheme is inspired by the work of *Schreyer et al.* [2006] and involves a decohesion stress tensor, associated with the development of fractures, that is used to bring super-critical stresses back on the yield curve following any correction path. We find that the growth of the residual errors is largely reduced when using the generalized stress correction scheme but that small growth remains. The angle of fracture in the uni-axial loading tests is sensitive to the magnitude of the decohesion stress tensor and represent well the typically observed values when the stress correction follows a path perpendicular to the yield curve. In contrast, the amount of divergence and shear deformations along the fracture plane is not sensitive to the decohesion stress tensor. Results demonstrate that the large deformations in the

MEB rheology occur post-fracture and are dissociated from the fracture process itself, an important difference with classical VP models.

In Chapter 5, we present a comparison of the sea-ice deformations simulated by the VP and the generalized MEB rheology. The goal is to identify the difference in the material behaviour simulated by the different parameterizations and to quantify the influence of the mechanical parameters (e.g. viscosity and strength) in the simulated sea-ice deformations. To this end, the deformations produced by the two rheologies are investigated first in 1D experiments, which show that the differences between the VP and MEB simulations are small except for the shape of the produced ridges, which are linear in the VP and concave in the MEB simulations. We also revisit the ice bridge simulation in the context of a longer-term integration to investigate the tendency of the VP and MEB rheologies to simulate ice arching in different positions in the channels. We show that when the rheologies use similar yield parameters, they both produce ice arches upstream of the channel after 2-3 days of time-integration. However, the post-fracture deformations in the MEB model lead to enhanced local ridging in the channel interior, providing anchor points from which other arches form post-fracture. The opening of a polynya in the channel adjacent to an upstream ice arch requires both a sufficient ice strength to sustain the compression upstream of the channel and free movement of the ice in the channel interior. We also find that the arch in the VP model is not sensitive to the maximum viscosity, contrary to what has been previously reported.

To conclude, a summary of findings is presented in the sixth chapter, and discussed in terms of their implication for future model developments. Note that each chapters are presented as published (Ch. 3), submitted (Ch. 4) or in-preparation (Ch. 2 and 5). Redundancies between these chapter are therefore present due to their self-sufficiency.

Chapter 2

Locating ice arches and ice grounding in landfast ice from satellite observations

This chapter examines the formation of ice arches in the different stages of the land-fast ice formation and break-up in different Arctic peripheral seas. The goal is to define the inter-play between the grounding of ice and ice arching and use this knowledge to guide future model developments. This paper will be submitted for publication in early 2021 in a peer review journal.

Locating ice arches and ice grounding in landfast ice from satellite observations

Mathieu Plante[1] and Bruno Tremblay[1]

[1]Department of Atmospheric and Oceanic Sciences, McGill University, Montréal, Québec, Canada

The manuscript reproduced here is in preparation for submission to a peer-reviewed Journal.

Abstract

The role of ice arching in the formation of the landfast ice cover in the Laptev Sea, the Kara Sea and the Canadian Archipelago is investigated using brightness temperature imagery for the MODerate resolution Imagining Spectroradiometer (MODIS). The ice arches are found to be a key component offshore landfast extensions in the Siberian marginal seas by sustaining ice arches in gaps between grounded ice ridges. The grounding of ice over shallow shoals is found to start early in the freezing season, and provides anchor points from which ice arches can form later in the winter. This inter-play between ice grounding and ice arching integrates contradicting observations previously reported in the literature and explains the presence of landfast ice over deep waters. The regions of higher landfast ice variability from the NIC ice charts are also found to correspond to locations where the landfast ice is sustained by larger ice arches, which are prone for break-up under the passage of weather systems. Based on these observations, we suggest that the ice grounding parameterization in sea-ice models be adapted to allow for an earlier grounding over the shallow shoals but also for their persistence in the melt season long after the collapse of the ice arches.

2.1 Introduction

The presence of landfast ice along the Arctic coastlines exerts a considerable influence on shore processes [*Barnes et al.*, 1984], fresh water retention [*Dmitrenko et al.*, 2005; *Eicken et al.*, 2005] and marine biology [*Carmack and Macdonald*, 2002]. At the landfast ice edge, the surface forcing from the atmosphere and the ocean pushes the free-flowing ice away, creating semi-permanent flaw polynyi that are responsible for a large portion of the winter Arctic ocean-atmosphere heat fluxes [*Dethleff et al.*, 1998]. With these important contributions to the Arctic system, the response of landfast ice to the warming Arctic is determinant for both the future climate and the planning of human activities in the Polar regions.

The formation of landfast-ice is usually associated with the presence of stamukhi, offshore areas where intensive ice ridging and grounding take place [*Reimnitz et al.*, 1978b]. On the

Alaskan coast, multiple observations provided evidence that the 50-100km large bands of landfast ice are being primarily controlled by the grounding of keels on the ocean floor, close to the -20 isobath [*Reimnitz et al.*, 1978b; *Mahoney et al.*, 2007, 2014]. The role of stamukhi is more limited in other areas, where the landfast ice extends to deeper waters. In the the Siberian Arctic, early in-situ observations featured very smooth ice surfaces that are incompatible with the presence of grounding [*Reimnitz et al.*, 1994]. This was later contradicted by the observation of local stamukhi [*Haas et al.*, 2005] and by local differences in the timing at which sea ice becomes immobile [*Selyuzhenok et al.*, 2017]. In the Kara sea, small islands rather act as a barrier that allows for the extension of the landfast-ice cover to deeper waters *Divine et al.* [2004]; *Olason* [2016]. In the Canadian Arctic Archipelago (CAA), the bathymetry is too deep for the grounding of ridges occur and the landfast ice is rather associated to the formation of ice arches in the narrow channels [*Melling*, 2002]. In these areas, the landfast ice cover is known to be sustained by its own mechanical strength [*Sodhi*, 1997; *Dumont et al.*, 2008].

In sea-ice models, the grounding of ice was recently parameterized to improved the simulated land-fast ice extent across the Arctic [*Lemieux et al.*, 2015]. Important discrepancies however remain in the timing of land-fast ice formation and break-up as well as in the land-fast ice stability, especially in regions where grounding seemingly plays a lesser role in the landfast ice formation, such as in the Kara Sea and the CAA [*Lemieux et al.*, 2016]. These difficulties can be attributed to the fact that the models are often tuned to represent the maximum landfast ice extent, but not its onset and break-up [*Olason*, 2016]. Tuning the mechanical strength to capture the landfast ice variability is however difficult [*Lemieux et al.*, 2016], given that the respective role of ice grounding and ice arching in the seasonal formation and break-up of the landfast ice cover remains largely undocumented.

In this analysis, the role of ice arching in shaping the landfast ice cover is analysed using daily satellite imagery. In particular, we study the ice arches in three peripheral seas with different bathymetric environments – the Laptev sea, the Kara sea, and the CAA – to determine a process of landfast ice formation that can be applied pan-Arctic and used to guide future landfast ice model developments.

This paper is organised as follows. The data used in this analysis are described in section 2. The observed landfast ice formation and break-up in the Laptev Sea, the Kara Sea and in the CAA is described in section 3. The results are discussed in section 4 in terms of the observed ice arch characteristics. Conclusions are presented in section 5.

2.2 Data

2.2.1 NIC ice chart gridded data

The ice charts from the National Ice Center [NIC, *National Ice Center*, 2006, updated 2009] are used to examine the probability of landfast ice occurrence in the Laptev Sea, the Kara Sea and the CAA over the 1976-2007 time period. This product consist of two sets of ice charts (from the NIC for the 1972-1994 period and from the Environmental System Research Institute (ESRI) for the 1995-2007 period) where the sea ice conditions, including fast-ice, were recorded in delimited polygons. The charts were produced weekly (from 1972 to June 2001) or biweekly (June 2001 through December 2007) for the primary purpose of navigation planing, and were generated by the analysis of a variety of data sources such as observations from ships, air reconnaissance, remote sensing and model outputs. These charts are produced over several days and do not represent a snapshot of the pan-Arctic sea ice conditions, although they are assembled to be valid on a given day. The polygon information from these ice charts, which include land-fast ice areas but also sea ice concentration and age, were later re-gridded on the Equal Area Scalable Earth Grid (EASE-grid) with a spatial resolution of 25 km. See *Dedrick et al.* [2001] for more details.

The monthly probability of occurrence is defined at the grid-scale as the fraction of years where landfast ice conditions were reported in the ice charts in the given month.

2.2.2 MODIS data

The seasonal formation of landfast sea ice is investigated using brightness temperature imagery from the MODIS (MODerate resolution Imagining Spectroradiometer) Terra and Aqua satellites (Band-31 Day and Night). Daily images are analysed from NASA Worldview (https://earthdata.nasa.gov/labs/worldview/), an open data tool that retrieves and maps data from the Global Imagery Browse Services (GIBS).

During the Arctic polar night and under clear sky conditions, the position of leads and polynyi are detectable in the brightness temperature imagery by the contrast between the warm sea water and the cold adjacent ice surface. The presence of landfast or grounded ice can be identified by the relatively large and semi-permanent polynyi that form as wind forcing pushes the mobile ice away from the landfast ice edges. These trailing polynyi are easily distinguished from the thin, short-lived and moving leads that characterise the deformations in the pack ice. Note that the trailing polynyi are only indicative of ice held immobile against a surface forcing, from which the presence of grounding can be inferred but not asserted.

2.3 Results

2.4 Laptev Sea

The Laptev Sea is characterised by a very shallow shelf offshore of the Lena delta (Fig. 2.1). Most of the landfast ice cover in the Laptev Sea is situated in the estuary-like confinement between the New Siberian Islands (N.S.I.) to the East and the Lena delta to the West [*Yu et al.*, 2014]. Although extensive, this section of the Laptev Sea is particularly shallow, with depth <20m except for a channel of somewhat deeper (<30m) waters. A few extensive shoals (with $\leq$10m depth) are also present (indicated by numbers in Fig. 2.1), of which the most extensive (point 2 in Fig. 2.1), reaches a depth $\leq$5m.

The NIC ice charts show that the landfast ice in the Southeastern Laptev sea starts to form in the fall and eventually extends hundreds of kilometers offshore (Fig 2.2). The maximum extent is usually reached January in a rapid extension that brings the landfast ice edge levelled with the N.S.I. (Fig 2.2, MAM), with a characteristic protrusion West of the N.S.I. The maximum extent shows very little inter-annual variability and changes very little once completed. The break up of landfast ice in the Laptev sea is also rapid, usually in July. Persistant landfast ice areas are found close to the N.S.I.

Based on the MODIS images, the large extent of landfast ice in the Laptev sea is created by a combination of ice grounding ice and ice arching (Fig. 2.3). At the earliest stage of the land-fast ice formation, the Laptev sea is covered by thin and mobile pieces of new ice, and the landfast ice is limited to a narrow band a few kilometers wide close to the coast, especially along the Lena delta (Fig. 2.3a). The extent of this narrow band more or less corresponds to the 10m bathymetry and to the fresh water landfast ice extent documented in *Eicken et al.* [2005]. Farther offshore, the trailing polynyi provide evidence of ice grounding in locations coinciding with the shallowest shoals in Fig. 2.3b. These locations also correspond to the position of early immobile ice floes in *Selyuzhenok et al.* [2017] and to the reported stamukhi in *Haas et al.* [2005]. As ice thickens in the Laptev sea, the grounded ice area expends to cover the entire shoals, the biggest reaching an area of more than 1500 km^2 (Fig 2.3c) and the farthest corresponding to the location of characteristic protrusions in the NIC charts landfast ice edge (Fig 2.3d). Later in the winter, ice arching occurs between the grounded ice areas, occasionally breaking under external forcings (Fig 2.3e) but eventually settling as the contiguous and stable Laptev sea landfast ice cover. The characteristic shape of the landfast ice edge in the Laptev sea thus corresponds to the grounded ice locations furthest from the shore, connected together by ice arches (Fig 2.3f).

The landfast ice break up is largely determined by the strength of the ice arches maintaining the landfast ice cover. Early in the melt season, water discharge from the Lena river floods the land-fast over a band tens of kilometer wide along the delta [Fig. 2.4a, also documented in *Bareiss et al.*, 1999; *Bareiss and Gorgen*, 2005]. The collapse of the ice arches however occurs weeks later, beginning with smaller-scale fractures that weakens the ice arches and increase their curvature (Fig. 2.4b). Following their collapse, the ice upstream breaks into smaller floes (Fig. 2.4b). Large areas of immobile (thus most likely grounded) sea ice remain over the largest ice shoals, only slowly depleting over time (Fig. 2.4c).

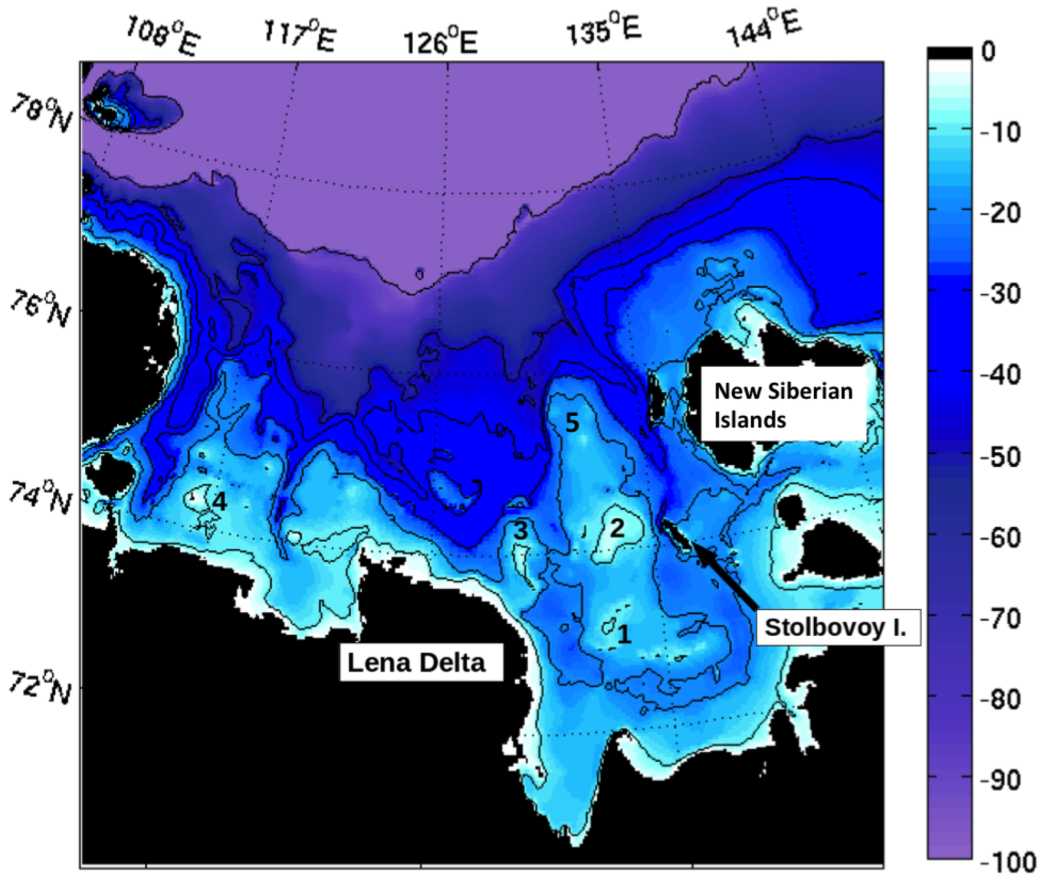

Figure 2.1: Bathymetry (in meters) of the Laptev sea from the International Bathymetric Chart of the Arctic Ocean (IBCAO) Version 3.0, at 500m resolution [*Jakobsson et al.*, 2012]. Black contour lines indicate the 10, 20, 30, 40, 50, and 100m isobaths. Numbers indicate the position of the shallowest shoals that are key for the formation of the Laptev sea landfast ice.

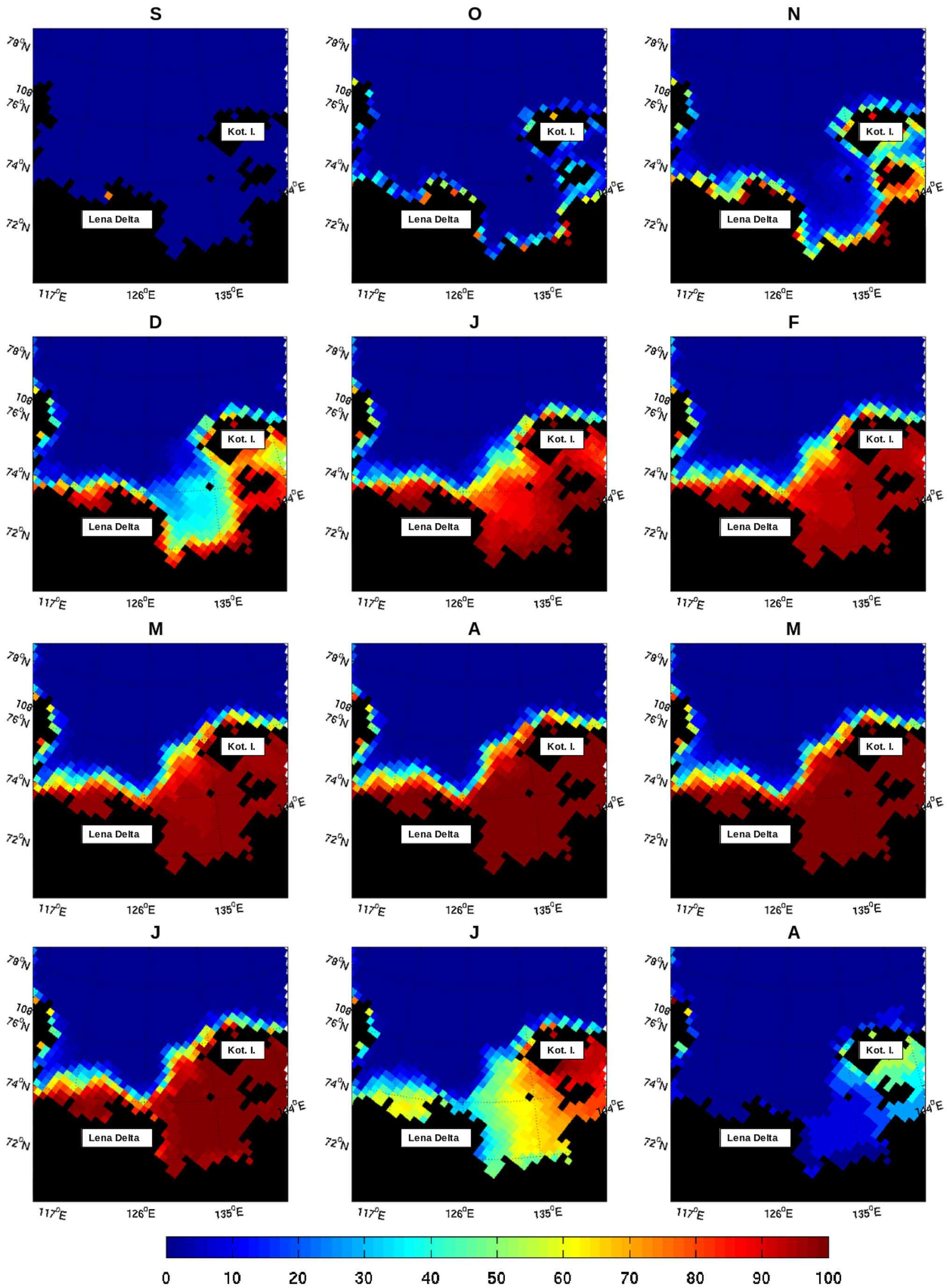

Figure 2.2: Monthly landfast ice occurence (in % years) in the Laptev sea for the 1976-2007 period, from the NIC ice charts [*National Ice Center*, 2006, updated 2009].

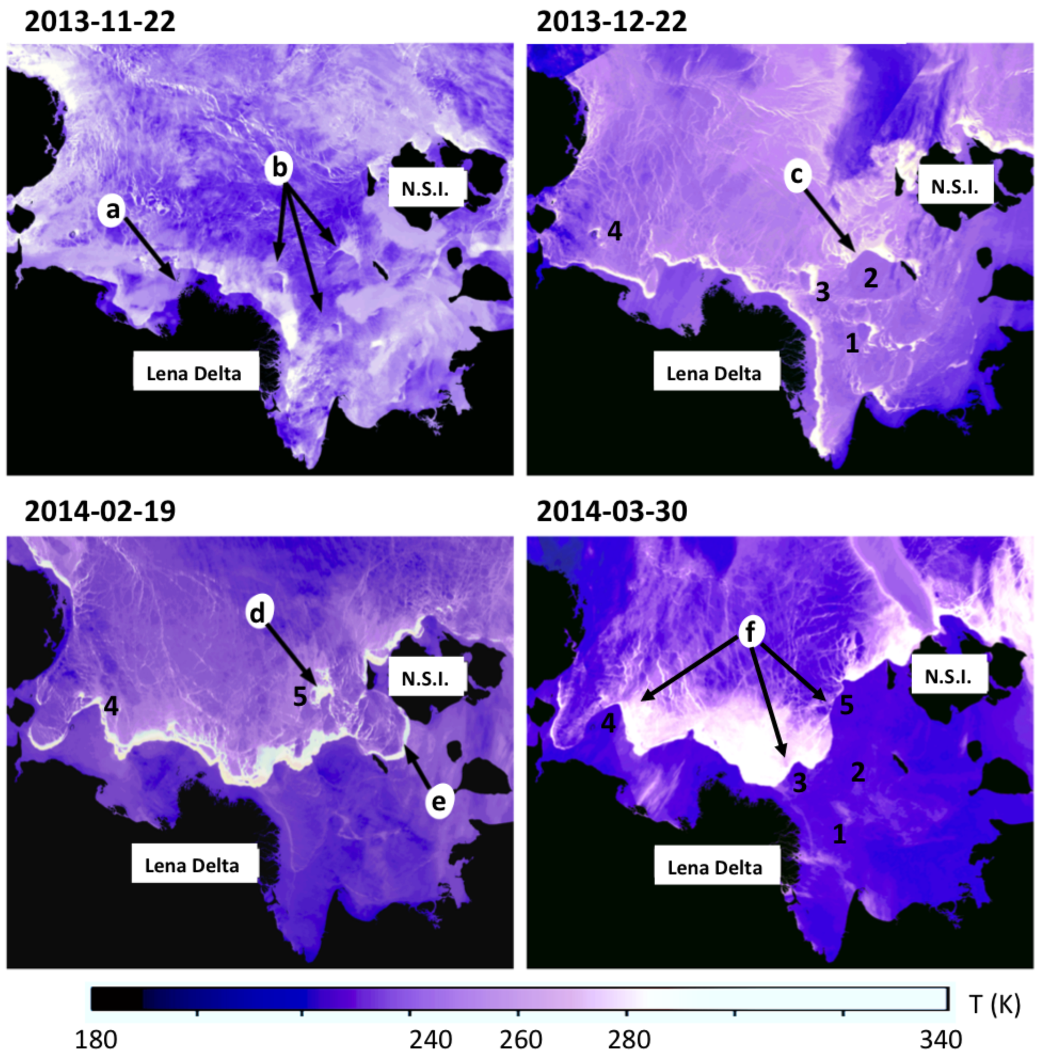

Figure 2.3: NASA Worldview brightness temperature imagery from the Moderate Resolution Imaging Spectroradiometer (MODIS) showing the different stages of landfast ice formation in the Laptev sea. Numbers refer to the numbered shoals in Fig. 2.1. a) narrow band of landfast ice about the Lena Delta, b) grounded ice identifiable from trailing polynya downwind of the shallow shoals numbered in Fig 2.1, c) extensive offshore grounding over the largest shoal, d) ice grounding evidence corresponding to the protrusion of landfast ice in the NIC charts, e) temporary collapse of landfast ice between the N.S.I and the large grounded shoal, f) grounded ice shoals providing anchor points for the landfast ice formation.

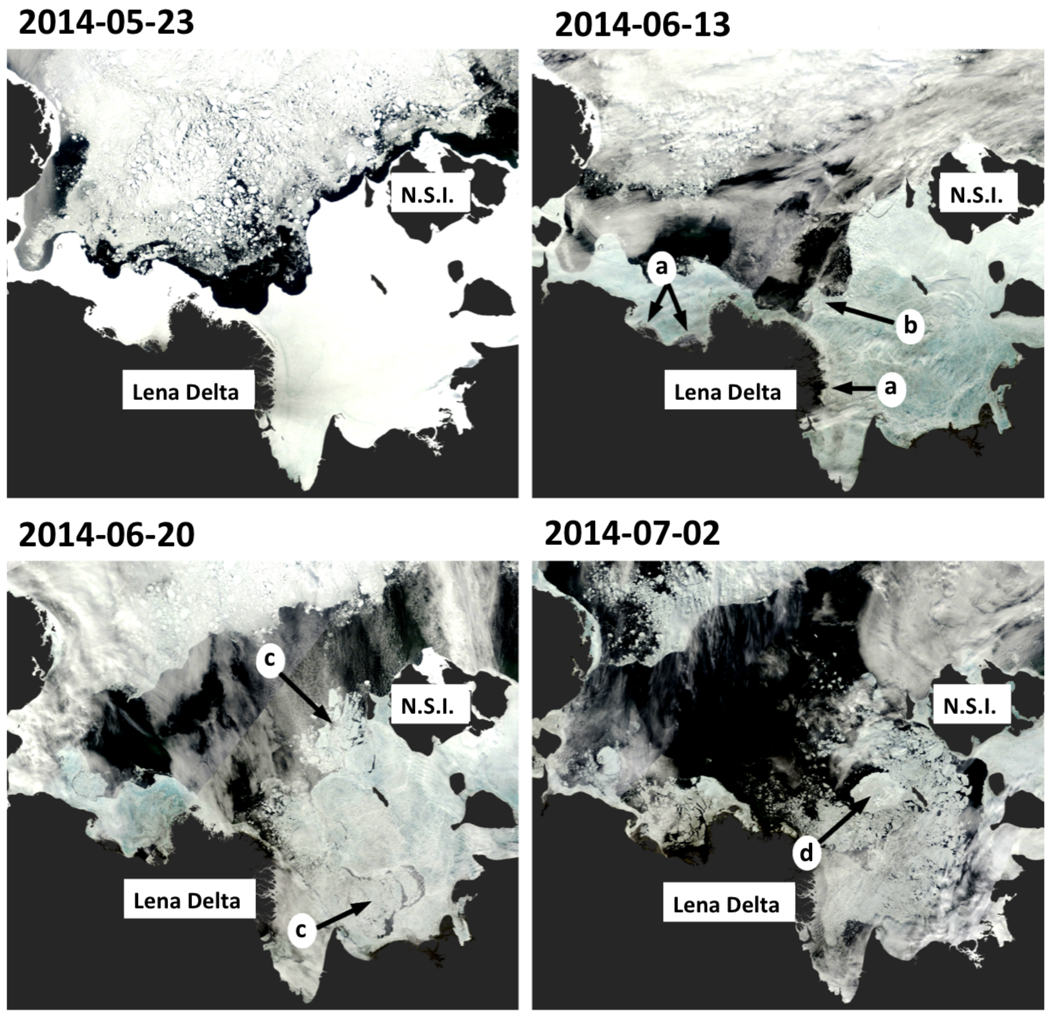

Figure 2.4: NASA Worldview Corrected Reflectance imagery (True Color) from the Moderate Resolution Imaging Spectroradiometer (MODIS) showing the different stages of landfast ice break-up in the Laptev sea. a) Plume of river discharge from the Lena river flooding the landfast ice, b) small scale fractures weakening the ice arches, c) broken ice floes following the collapse of the ice arches, d) large area of grounded ice persisting over the largest shoals.

2.4.1 Kara sea

The Kara Sea corresponds to the marginal Siberian waters confined by Severnaya Zemlya to the East and Novaya Zemlya to the West (Fig. 2.5). Most of the landfast ice area is located in the Southeastern portion of the sea, directly North of the Taymyr Peninsula [*Yu et al.*, 2014]. The bathymetry of the South-eastern Kara Sea is overall deeper but also rougher than in the Laptev sea, with a collection of archipelagos punctuating the sea bed between deeper channels that reach >50m depths (see number 1 and 2 in Fig. 2.5). The distance between the islands vary from tens to ∼ 100 kilometers.

Based on the NIC charts, the landfast ice cover in the Kara sea starts to form in October and reaches its full extent in February (Fig. 2.6). The landfast ice extent features significant inter-annual variability, with only a thin band along the coast presenting 100% occurrence in late winter. It nonetheless usually extends to the archipelagos offshore of the Taymyr Peninsula. The most variable location is located to the East of the Arctic Institute Island (A.I.I.) where landfast ice is only reported half of the years covered by the data set. The break-up of landfast ice is rapid and usually completed before July.

In the MODIS observations, trailing polynyi indicate grounding around the different offshore islands early in the season, significantly expanding the surface of immobile ice over the shallowest waters (Fig. 2.7a). As in the Laptev sea, evidence of grounding are present early in the freezing season (early November). As the ice thickens, ice arches are eventually able to form between these extended islands (see Fig. 2.7b). The ice arches are however unstable and prone to break up upon the passage of storms, after which the landfast ice is often limited to the likely grounded areas (see Fig. 2.7d). The frequent ice arch break-ups correspond well with the reported variability in the NIC ice charts. Based on these observations, the area of 50% occurrence in the NIC ice charts corresponds to the widest gap between the grounded ice areas, where an unstable ice arch regularly forms but breaks more easily than the smaller arches to the East (number 4 in 2.7c). These observations are in accord with the fact that the landfast ice extension usually follows cold and calm weather in the Kara sea [*Divine et al.*, 2004], allowing from the refreezing of leads and consolidating the ice cover. Note that in stormy conditions, the landfast ice may not reform long enough to be recorded in the ice charts, but nonetheless temporarily reforms in all observed winters.

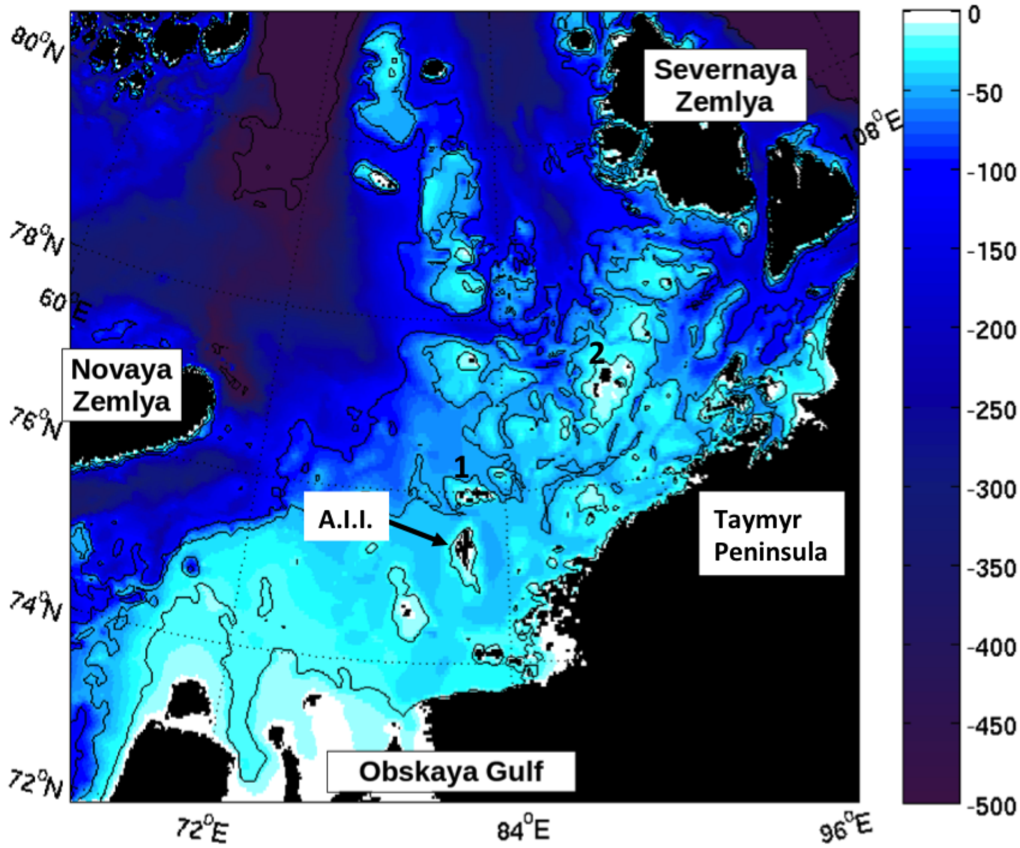

Figure 2.5: Bathymetry (in meters) of the Kara sea from the International Bathymetric Chart of the Arctic Ocean (IBCAO) Version 3.0, at 500m resolution [*Jakobsson et al.*, 2012]. Black contour lines indicate the 20, 50, 100, and 500m isobaths. Numbers indicate the position of islands that are key for the formation of the Laptev sea landfast ice.

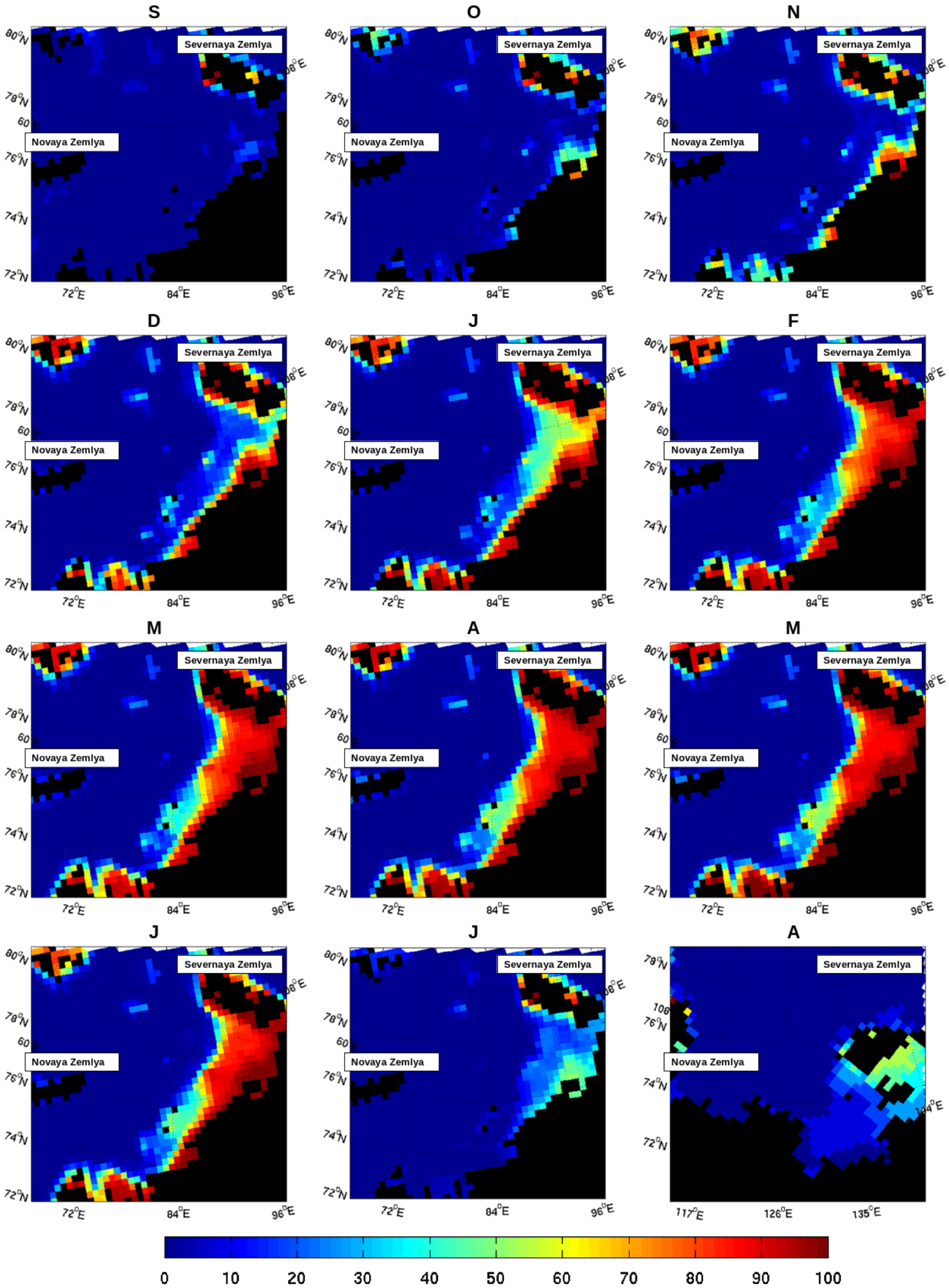

Figure 2.6: Monthly landfast ice occurrence (in % years) in the Kara sea for the 1976-2007 period, from the NIC ice charts [*National Ice Center*, 2006, updated 2009].

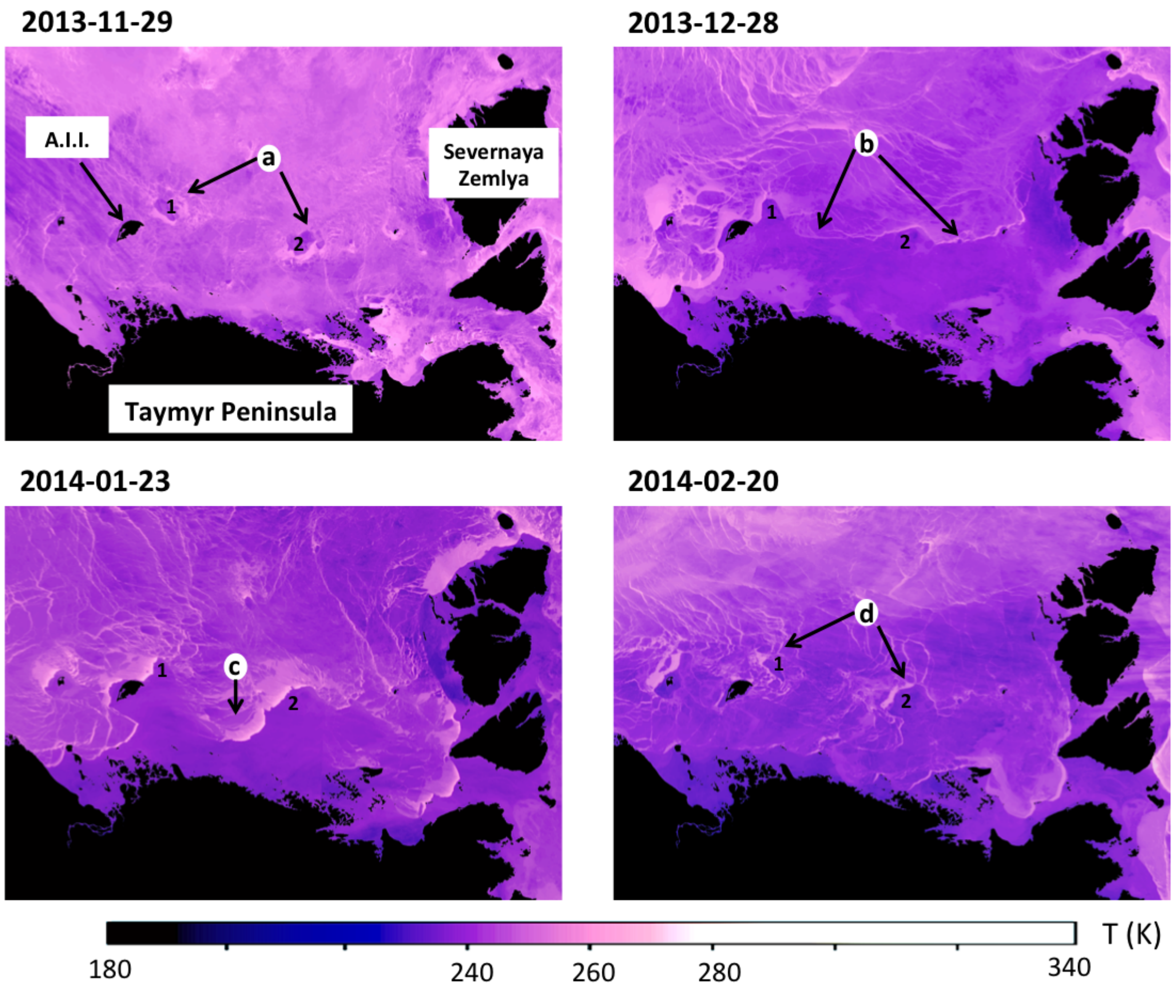

Figure 2.7: NASA Worldview brightness temperature imagery from the Moderate Resolution Imaging Spectroradiometer (MODIS) showing the different stages of landfast ice formation in the Kara sea. Numbers refer to the numbered islands in Fig. 2.5. a) ice grounding expending the area of immobile ice around small archipelagos, b) arching fracture between the different archipelagos, c) collapse of a large ice arch corresponding to the location of higher landfast ice variability in the NIC charts, d) extensive offshore grounding over the largest shoal, d) areas of immobile ice persisting after the collapse of the ice arches.

2.4.2 Canadian Arctic Archipelago

The Canadian Arctic Archipelago is largely different from the other marginal seas, being characterised by a large network of islands separated by extensive channels tens of kilometers wide and several hundreds kilometers long (Fig. 2.8). The water depth in the channels vary from ~ 100 meters to several hundred meters close to the Baffin Bay, such that the grounding of sea ice is impossible. The formation of landfast ice mostly depends on the sea ice becoming land-locked in the channels and the formation of ice arches.

The seasonal presence of landfast ice in the CAA from the NIC ice charts is presented in Figure 2.9. As extensively documented in [*Galley et al.*, 2012], the CAA landfast ice forms early in the fall season in the northern portion of the CAA, and rapidly covers most of the CAA expect for the Barrow Strait the Prince Regent Inlet and the Gulf of Boothia, where significant inter-annual variability is present. Most years, the landfast ice reaches the Lancaster Sound, occasionnally extending East of the Prince of Wales Island. We refer the reader to [*Galley et al.*, 2012] for more details.

The MODIS observations show that the progression of landfast ice towards the Lancaster Sound in the Barrow Strait depends on the formation of ice arches at key locations of the CAA (Fig. 2.10). Going eastward from Resolute, the gap between the islands increases such that the stabilisation of landfast ice depends on larger ice arches. The smallest ice arches, between islands offshore from Resolute, are formed early the winter (Fig. 2.10a and b). The channel section to the North of the Prince of Wales island later becomes landfast when a larger ice arch forms between Devon Island and a small island close to the Prince of Wales island (2.10d). This ice arch corresponds to the most common location of the landfast ice edge. The occasional extension of the landfast ice further east in the Lancaster Sound relies a large ice arches that is prone to collapse under the strong tidal forcing in the region.

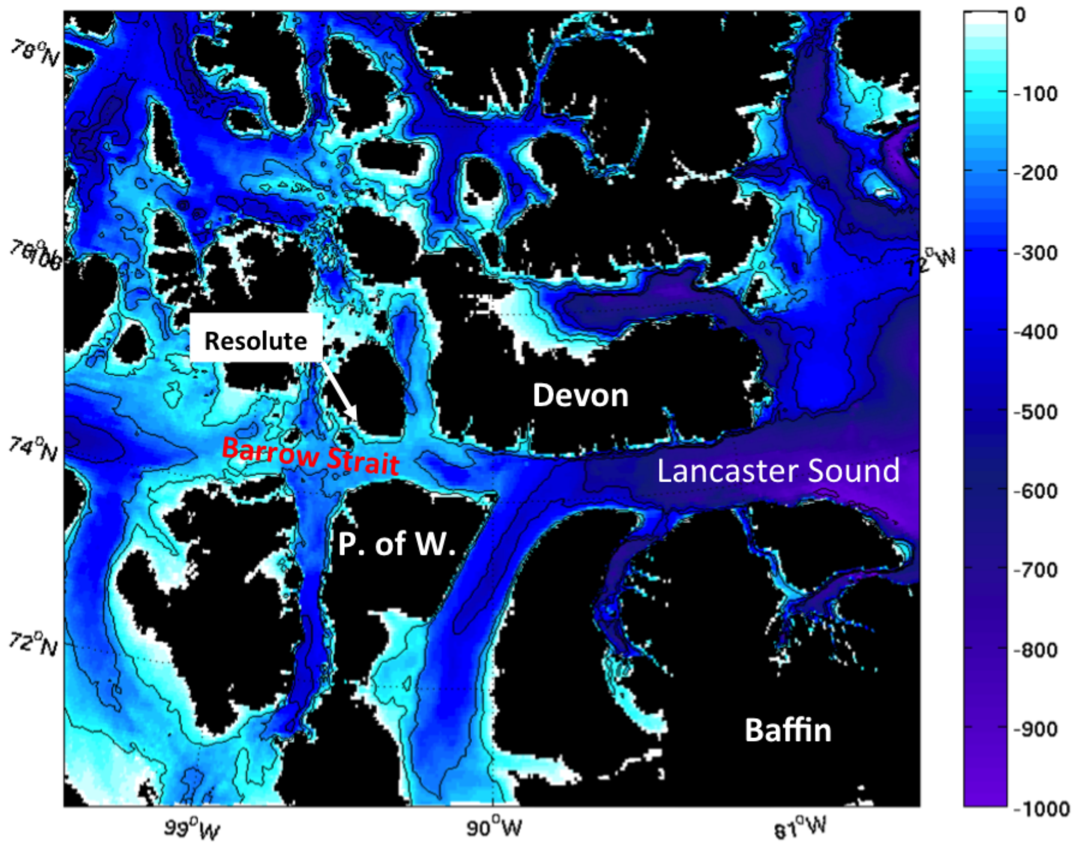

Figure 2.8: Bathymetry (in meters) of the CAA from the International Bathymetric Chart of the Arctic Ocean (IBCAO) Version 3.0, at 500m resolution [*Jakobsson et al.*, 2012]. Black contour lines indicate the 100, 200, 400, 600 and 1000m isobaths.

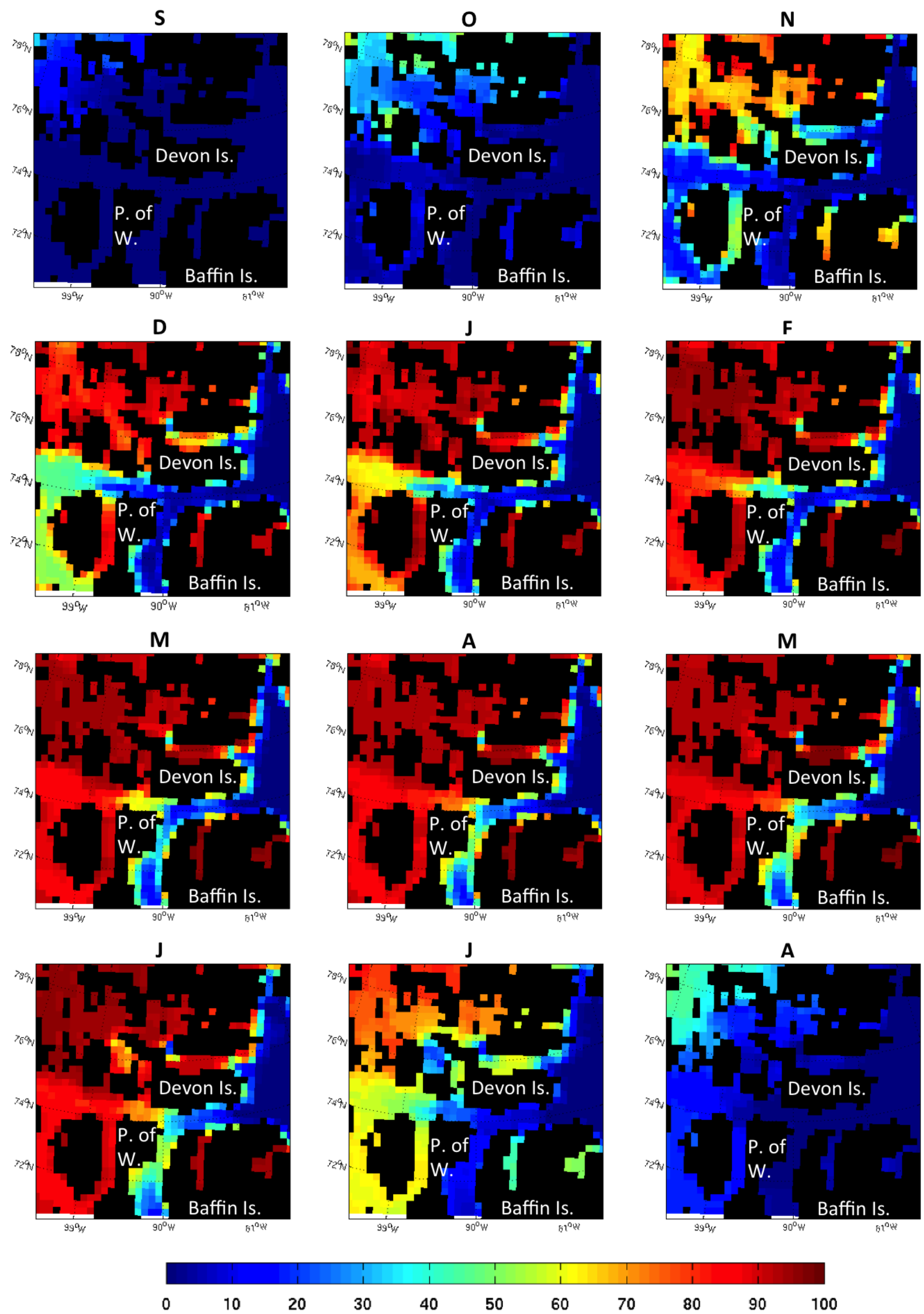

Figure 2.9: Monthly landfast ice occurrence (in % years) in the CAA for the 1976-2007 period, from the NIC ice charts [*National Ice Center*, 2006, updated 2009].

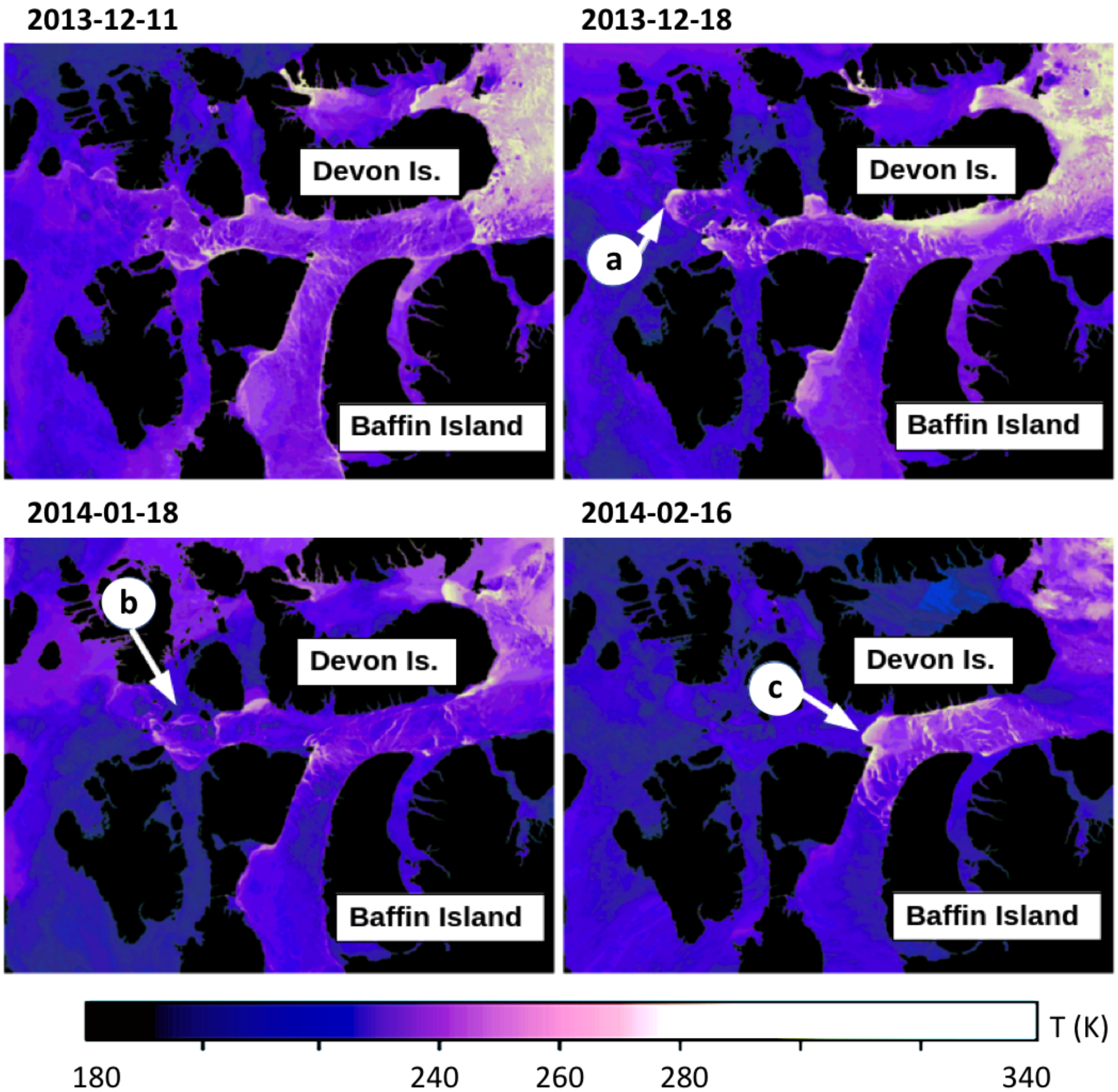

Figure 2.10: NASA Worldview brightness temperature imagery from the Moderate Resolution Imaging Spectroradiometer (MODIS) showing the different stages of landfast ice formation in the CAA. a) Formation of small ice arches in the Parry Channel, b) consolidated land-fast ice up to the Barrow Strait, c) formation of the ice arch between the Prince of Wales and Devon islands.

2.5 Discussion

Our results show that the formation of ice arches plays a crucial role for the extension of landfast ice to deeper waters in each of the investigated marginal seas. Although only images from the 2013-2014 winter are presented, the sequence of events leading to the maximum landfast ice extent in each regions are observed in all years with available imagery from NASA Worldview (2012-2020). Our analysis was also repeated in the East Siberian and Greenland seas (not shown for conciseness), and showed similar results, with large offshore shoals (or islands) providing anchor points from which ice arches can form and eventually sustain a landfast ice cover. The presence of immobile ice above shallow shoals in many locations suggests that the grounding of ice occurs early in the Arctic freeze-up and indicates a large contribution of hummocks. The formation of ice arches only plays a later role in the extension of the landfast ice cover. We speculate that the stabilization of the largest ice arches depends on the presence of large consolidated ice floes, in accord with the observation that the Kara sea landfast ice extensions usually occurs during particularly cold and calm conditions.

Note that the combination of ice grounding and ice arching in the formation of large landfast ice extents is compatible with the large variety of coastal-morphologies across the Arctic, from the grounding-dominated Beaufort Sea coast to the large Siberian landfast ice covers, and with the landfast ice channels of the CAA. In the Laptev sea, this mechanism is also compatible with the observation of a thin and smooth landfast ice edge [i.e. along the ice arch sections, *Reimnitz et al.*, 1994], the reports of the local stamukhi zones over shallow shoals [i.e. betwen the ice arches, *Haas et al.*, 2005], and with the varying timing of the local onset and end of the ice movement [*Selyuzhenok et al.*, 2017].

The ice arches reported in this analysis vary in scales but all are limited to $<$ 100 km wide channels. In general, the ice arches $<$ 50 km are more stable and sustain a solid landfast ice cover until the spring break up. Larger ice arches correspond to areas with larger landfast ice instability in the NIC ice charts. Note that most of the ice arches are formed at narrowing points between islands or areas of grounded ice, leaving the downstream passages ice-free. The observation of tensile ice arches downstream of the channels [*Dansereau et al.*, 2017; *Plante et al.*, 2020] are rare due to the irregular land morphologies which provide many convergent points making it easier for ice arches to form. The fact that landfast ice channels upstream of the ice arches sustain the forcing related to weather systems is nonetheless indicative of the cohesion of sea ice [*Plante et al.*, 2020].

Based on these observations, we suspect that the miss-representation of the landfast ice onset and break-up in sea ice models relates to the grounding parameterization of *Lemieux et al.* [2015] underestimating the amount of grounding both early in the freezing season and during the melt season. That is, associating the grounding to the average ice thickness under-estimates both the influence of hummocks when the ice is yet very thin, and removes the grounding too early as the mean ice thickness decreases during the melt season. The absence of a simulated landfast ice cover in areas where it depends on the formation of large ice arches is also indicative of an insufficient material strength, or to the need for higher resolution land morphology and bathymetry (for grounding) to provide the compressive conditions needed for their formation.

2.6 Conclusions

We document the role of ice arches in the formation of the landfast ice cover based on satellite observations in the Laptev sea, the Kara sea and the CAA. The presence of grounded ice is identified in the brightness temperature imagery by the trailing polynya downwind of immobile ice floes. We find that grounding occurs early in the freezing season over shallow shoals, which later provide anchor points from which ice arches can form, sustain landfast ice over deeper regions. We also find that regions of higher landfast ice variability correspond to the position of larger ice arches in wider gaps between the grounded ice ridges, which are more prone to break under stormy weather. These observations show that ice arching is part of the landfast ice process, not only in the CAA, but across all of the Arctic, including in shallow regions where grounding is prominent such as in the Laptev sea. The location of ice arching and grounding are also in accord with contradicting observations previously reported in the literature. Based on these observations, we suggest that the parameterized relationship between the ice grounding and the mean ice thickness be revisited, to produce grounding early in the season, without over-estimating its presence in the winter but also allowing its persistence into the melt season.

Chapter 3

Landfast sea ice material properties derived from ice bridge simulations using the Maxwell Elasto-Brittle rheology

In this chapter, the implementation of the Maxwell Elasto-Brittle rheology on the numerical framework of the McGill Sea-Ice Model is presented. The new rheology and its damage parameterization are used to simulate the formation and collapse of ice arches in a landfast ice channel and to determine the material strength associated with stable landfast ice channels commonly observed in the Arctic. This is published as highlight paper in the journal The Cryosphere: Plante, M., Tremblay, B., Losch, M., and Lemieux, J.-F. (2017), Landfast sea ice material properties derived from ice bridge simulations using the Maxwell elasto-brittle rheology, The Cryosphere, 14, 2137–2157, https://doi.org/10.5194/tc-14-2137-2020.

Landfast sea ice material properties derived from ice bridge simulations using the Maxwell Elasto-Brittle rheology

Mathieu Plante[1], Bruno Tremblay[1], Martin Losch[2] and Jean-FrançoisLemieux[3]

[1]Department of Atmospheric and Oceanic Sciences, McGill University, Montréal, Québec, Canada [2]Alfred Wegener Institute for Polar and Marine Research, Bremerhaven, Germany [3]Recherche en prévision numérique environnementale, Environnement et changement climatique Canada, Dorval, Québec, Canada.

The original publication is available at https://tc.copernicus.org/articles/14/2137/2020/tc-14-2137-2020-discussion.html

Abstract

The Maxwell Elasto-Brittle (MEB) rheology is implemented in the Eulerian, Finite Difference (FD) modeling framework commonly used in classical Viscous-Plastic models. The role of the damage parameterization, the cornerstone of the MEB rheology, in the formation and collapse of ice arches and ice bridges in a narrow channel is investigated. Ice bridge simulations are compared with observations to derive constraints on the mechanical properties of landfast sea ice. Results show that the overall dynamical behavior documented in previous MEB models is reproduced in the FD implementation, such as the localization of the damage in space and time, and the propagation of ice fractures in space at very short time-scales. In the simulations, an ice arch is easily formed downstream of the channel, sustaining an ice bridge upstream. The ice bridge collapses under a critical surface forcing that depends on the material cohesion. Typical ice arch conditions observed in the Arctic are best simulated using a material cohesion in the range of 5-10 kN m^{-1}. Upstream of the channel, fracture lines along which convergence (ridging) takes place are oriented in an angle that depends on the angle of internal friction. Their orientation however deviates from the Mohr-Coulomb theory. The damage parameterization is found to cause instabilities at large compressive stresses, which prevents the production of longer term simulations required for the formation of stable ice arches upstream of the channel, between these lines of fracture. Based on these results, we propose that the stress correction scheme used in the damage parameterization be modified to remove numerical instabilities.

3.1 Introduction

The term landfast ice designates sea ice that is attached to the coastlines, acting as an immobile and seasonal extension of the land. It starts to form in shallow water in the early stages of the Arctic freeze up [*Barry et al.*, 1979; *Reimnitz et al.*, 1978a] and grows throughout the Arctic winter, usually reaching its maximum extent in early spring [*Yu et al.*, 2014]. Typically, large landfast ice areas can form and remain stable due to the presence of

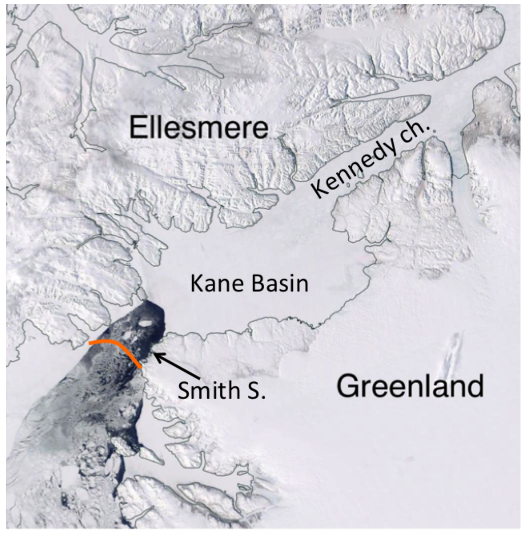

Figure 3.1: NASA Worldview image of a stable landfast ice arch in Nares Strait, from Moderate Resolution Imaging Spectroradiometer (MODIS) Corrected Reflectance imagery (True Color), on May 1st 2018. The orange curve indicates the position of the stable ice in [*Dansereau et al.*, 2017].

islands or by the grounding of ice keels on the ocean floor [*Reimnitz et al.*, 1978a; *Mahoney et al.*, 2007; *Selyuzhenok et al.*, 2017]. Where the water is too deep for grounding, landfast ice can also form where ice floes are jammed in narrow passages between islands or pieces of grounded ice. In the Canadian Arctic Archipelago (CAA), this type of ice is referred to as land-locked. The resulting ice bridges, also called ice arches for their characteristic arching edges (Fig. 3.1), can have a profound influence on sea ice circulation by the closure of gateways [*Melling*, 2002; *Kwok*, 2005], and on regional hydrography by the formation of winter polynyas downstream of the arches [*Barber and Massom*, 2007; *Dumont et al.*, 2010; *Shroyer et al.*, 2015]. Most studies about ice arches focused on the Nares Strait (Fig. 3.1) and Lincoln Sea ice bridges [*Kozo*, 1991; *Dumont et al.*, 2008; *Dansereau et al.*, 2017; *Moore and McNeil*, 2018; *Vincent*, 2019], which affect the export of thick multi-year ice into the Baffin Bay [*Kwok and Cunningham*, 2010; *Ryan and Münchow*, 2017]. Ice arches however are a seasonal feature in several locations of the Canadian Arctic Archipelago [*Marko and Thomson*, 1977; *Sodhi*, 1997; *Melling*, 2002] and are also present in the Kara and Laptev seas [*Divine et al.*, 2004; *Selyuzhenok et al.*, 2015; *Olason*, 2016] where they play a role in the formation of extensive landfast ice covers.

Despite decades of observations [*Melling*, 2002; *Kwok*, 2005; *Moore and McNeil*, 2018; *Ryan and Münchow*, 2017], the formation, persistence and break up of ice arches remain difficult to predict. It is however clear from modeling studies that the ability of sea ice to form arches relates to the material properties of sea ice. A number of studies showed that ice arches are produced if the rheology includes sufficient material cohesion [*Ip*, 1993; *Hibler et al.*, 2006; *Dumont et al.*, 2008]. Using the ellipse yield curve of *Hibler* [1979], this can be achieved either by decreasing the yield curve ellipse aspect ratio [*Kubat et al.*, 2006; *Dumont et al.*, 2008] and/or by extending the ellipse towards larger isotropic tensile strength [*Beatty and Holland*, 2010; *Olason*, 2016; *Lemieux et al.*, 2016]. The range of parameter values that are appropriate for the production of ice bridges varies between different numerical studies, suggesting that different forcing or model implementations may influence the ice arch formation [*Olason*, 2016; *Lemieux et al.*, 2016, 2018].

In recent years, new rheologies were proposed to reproduce the observed characteristics of ice failure, such as the preferred orientation of the lines of fracture [*Wilchinsky and Feltham*, 2004; *Schreyer et al.*, 2006], or the brittle behavior of sea ice at small scales [*Girard et al.*, 2011; *Dansereau et al.*, 2016]. Among this effort, a brittle damage parameterization [*Amitrano et al.*, 1999] was implemented in the neXtSIM model [*Rampal et al.*, 2016], as part of the Elasto-Brittle [*Girard et al.*, 2011, EB] and Maxwell Elasto-Brittle [*Dansereau et al.*, 2016, MEB] rheologies. The MEB rheology was shown to produce ice arches in the Nares Strait region that remain stable for several days, and arch fractures that are part of the landfast ice break up process [*Dansereau et al.*, 2017]. The simulated stable ice arches in *Dansereau et al.* [2017] are located downstream of either Smith Sound or Kennedy channel (see orange curve in Fig 3.1). These locations differ from the observed ice arch positions in Nares Strait upstream of these channels (e.g., see Fig 3.1) or in the Lincoln Sea [*Vincent*, 2019], which are well reproduced by standard VP or EVP models [e.g., *Dumont et al.*, 2008;

Rasmussen et al., 2010]). Whether this difference in behavior stems from the different physics of MEB and VP rheologies or whether it is just due to the different numerical framework used in both models remains an open question.

The EB/MEB models so far have been implemented using Lagrangian advection schemes and/or finite element methods (e.g. *Rampal et al.* 2016; *Dansereau et al.* 2017). These numerical features, however, make it difficult to compare the different MEB/EB physics with that of the standard VP or EVP rheologies of the modeling community, as these are usually implemented on Eulerian Finite Difference (FD) numerical frameworks. In this paper, we present our implementation of the MEB rheology on the FD numerical framework of the McGill VP sea ice model [*Tremblay and Mysak*, 1997; *Lemieux et al.*, 2008, 2014]. To our knowledge, it is the first time the MEB rheology is implemented on the numerical platform of a VP model such that its different physics can be assessed independently from the numerical implementation. With this model, we investigate the role of the damage parameterization and the material strength parameters in the formation of ice arches, using an idealized model domain capturing the basic features of real-life geometries where ice arches are observed. We also identify a numerical issue associated with the damage parameterization, which significantly impacts long simulations.

The paper is organised as follows. In section 2, we present the implementation of the Maxwell Elasto-Brittle rheology in our FD numerical framework. A detailed analysis of the break up of the ice bridge simulated by the MEB rheology is presented in section 3, along with a sensitivity analysis of the results with respect to the material parameters. The MEB model performance in simulating compressive fractures is discussed in section 4, with summarized conclusions in section 5.

3.2 Maxwell Elasto-Brittle Model

3.2.1 Momentum and continuity equations

The 2D momentum equation describing the motion of sea ice is written as:

$$\rho_i h \frac{\partial \boldsymbol{u}}{\partial t} = \nabla \cdot \sigma + \tau, \tag{3.1}$$

where ρ_i is the ice density, h is the mean ice thickness, $\mathbf{u}$ $(= u\hat{\mathbf{i}} + v\hat{\mathbf{j}})$ is the ice velocity vector, σ is the vertically integrated internal stress tensor and τ $(= \tau_a + \tau_w)$ is the total external surface forcings from winds and ocean currents. Note that we write the momentum equation in terms of the vertically integrated internal sea ice stresses (i.e., $\nabla \cdot \boldsymbol{\sigma}$) as standard in VP models [e.g., *Hibler*, 1979; *Hunke and Dukowicz*, 1997; *Wilchinsky and Feltham*, 2004], as opposed to the mean internal sea ice stresses (i.e., $\nabla \cdot (h\boldsymbol{\sigma})$) used in previous implementations of the MEB rheology [*Dansereau et al.*, 2016; *Rampal et al.*, 2016]. We assume no grounding of ice on the ocean floor and neglect the Coriolis term. This omission is appropriate for landfast ice, but can result in small errors in drifting ice [*Turnbull et al.*, 2017]. The advection of momentum (which scales as $\rho_i H[U]^2/L$, where H, $[U]$ and L are the characteristic ice thickness, velocity, and length scales) is three orders of magnitude smaller than a characteristic air or ocean surface stresses [*Zhang and Hibler*, 1997; *Hunke and Dukowicz*, 1997]. At the edge of an ice arch where a discontinuity in sea ice drift is present at the grid scale (2 km in our case), it remains two orders of magnitude smaller than other terms in the momentum equation.

The total surface stress is defined in terms of an effective stress (τ_{LFI}) that represents the combined wind and ocean forces acting on the landfast ice, and an additional water drag term that only acts on the drifting ice. That is, using the standard bulk formula [with air and water turning angles set to zero, *McPhee*, 1979], we have:

$$\boldsymbol{\tau} = \rho_a C_{da} |\boldsymbol{u}_a| \boldsymbol{u}_a + \rho_w C_{dw} |\boldsymbol{u}_w - \boldsymbol{u}| (\boldsymbol{u}_w - \boldsymbol{u}), \tag{3.2}$$

$$\approx \rho_a C_{da} |\boldsymbol{u}_a| \boldsymbol{u}_a - \rho_w C_{dw} |\boldsymbol{u}_w| \boldsymbol{u}_w - \rho_w C_{dw} |\boldsymbol{u}| \boldsymbol{u}, \tag{3.3}$$

$$\approx \tau_{LFI} - \rho_w C_{dw} |\boldsymbol{u}| \boldsymbol{u}, \tag{3.4}$$

where ρ_a and ρ_w are the air and water densities, C_{da} and C_{dw} are the air and water drag coefficients (see values in Table 3.2), and $\boldsymbol{u}_a$ and $\boldsymbol{u}_w$ are the surface air and water velocities. Note that the cross terms $\boldsymbol{u}_w \boldsymbol{u}$ have been neglected. This equation is therefore exact for landfast ice, the focus of this study, and constitutes an approximation only for ice drifting over an ocean current. Below, we specify τ_{LFI} and give the characteristic wind speed and ocean current equivalent to this forcing for reference.

The continuity equations used for the temporal evolution of the mean ice thickness h (volume per grid cell area) and concentration A ($0 < A < 1$) are written as:

$$\frac{\partial h}{\partial t} + \nabla \cdot (h\boldsymbol{u}) = S_h, \tag{3.5}$$

$$\frac{\partial A}{\partial t} + \nabla \cdot (A\boldsymbol{u}) = S_A, \tag{3.6}$$

where S_h and S_A are thermodynamic sink and source terms for ice thickness and compactness respectively. As we are only interested in the dynamical behavior of the sea ice model, all thermodynamics are turned off so that $S_h = 0$ and $S_A = 0$. Mechanical redistribution (i.e. ridging) is taken into account by capping the ice concentration at 1 (or 100%) in convergence. As the mean ice thickness h is allowed to grow, the capping increases the actual ice thickness [*Schulkes*, 1995].

Table 3.1: Material strength parameters from observations

Parameter	Reference	Parameter	Value
Young Modulus	*Langleben* [1962]	Y	$6.5 - 10$ GN m^{-2}
	Weeks and Assur [1967]		$1 - 9$ GN m^{-2}
	Tabata [1955]		$7 - 18$ GN m^{-2}
Poisson ratio	*Weeks and Assur* [1967]	ν	$0.33 - 0.4$
Viscosity	*Tabata* [1955]	η_0	$0.6 - 2.4$ TNs m^{-2}
Viscous relaxation time	*Tabata* [1955] [a]	λ_0	$14 - 40$ min
	Weeks and Assur [1967][a]		$28 - 32$ min
	Sukhorukov [1996][a]		66 h
	Hata and Tremblay [2015a]		10^5 s
Angle of internal friction	*Schulson et al.* [2006]	ϕ	$\sim 42°$
	Weiss et al. [2007]		$\sim 44°$
Compressive strength	*Weiss et al.* [2007]	σ_{c_0}	50 kN m^{-2}
	Tremblay and Hakakian [2006][b]		$30 - 100$ kN m^{-2}
	Tucker and Perovich [1992][c]		30 kN m^{-2}
	Richter-Menge et al. [2002][c]		$30 - 50$ kN m^{-2}
	Richter-Menge and Elder [1998][c]		$100 - 200$ kN m^{-2}
Tensile strength	*Weiss et al.* [2007]	σ_{t_0}	50 kN m^{-2}
	Tremblay and Hakakian [2006][b]		$25 - 30$ kN m^{-2}
	Tucker and Perovich [1992][c]		30 kN m^{-2}
	Richter-Menge and Elder [1998][c]		50 kN m^{-2}
Cohesion	*Sodhi* [1997][b]	c_0	1.99 N m^{-1}
	Weiss et al. [2007]		40 kN m^{-2}

[a] From small scale measurements in the field.
[b] Estimate from satellite observations.
[c] Observed peak stresses.

Table 3.2: Default Model Parameters

Parameter	Definition	Value
Δx	Spatial resolution	2 km
Δt	Time step	0.5 s
T_d	Damage time scale	2 s
Y	Young Modulus	1 GN m^{-2}
ν	Poisson ratio	0.3
λ_0	Viscous relaxation time	10^5 s
ϕ	Angle of internal friction	45°
c_0	Cohesion	10 kN m^{-2}
σ_{c_0}	Isotropic compressive strength	50 kN m^{-2}
ρ_a	Air density	1.3 kg m^{-3}
ρ_i	Sea ice density	9.0×10^2 kg m^{-3}
ρ_w	Sea water density	1.026×10^3 kg m^{-3}
C_{da}	Air drag coefficient	1.2×10^{-3}
C_{dw}	Water drag coefficient	5.5×10^{-3}

Table 3.3: Material properties used in sea ice models (VP,EVP and MEB)

Parameter	Reference	Parameter	Value
Young Modulus	*Hunke* [2001]	$E = \zeta/T$	1060 GN m^{-2}
	Bouillon and Rampal [2015]	Y	9 GN m^{-2}
	Dansereau et al. [2016]	E_0	0.585 GN m^{-2}
	Sulsky and Peterson [2011]	E	1 MN m^{-2}
	Tran et al. [2015]	E	1 MN m^{-2}
Maximum Viscosity	*Olason* [2016]	ζ_{max}	378×10^{15} kg s^{-1}
	Dansereau et al. [2016][a]	$\eta_0 = 10^7 E_0$	5.85×10^{15} kg m^{-1} s^{-1}
	Hunke [2001]	ζ_{max}	1375×10^{12} kg s^{-1}
	Tremblay and Mysak [1997]	η_{max}	1×10^{12} kg s^{-1}
	Hibler [1979]	ζ_{max}	125×10^{9} kg s^{-1}
	Dumont et al. [2008]	ζ_{max}	4×10^{8} kg s^{-1}
Compressive strength	*Tran et al.* [2015]	f_c'	125 kN m^{-2}
	Sulsky and Peterson [2011]	f_c'	125 kN m^{-2}
	Lemieux et al. [2016][a]	P_p	100 kN m^{-2}
	Olason [2016]	p^*	40 kN m^{-2}
	Dansereau et al. [2016]	σ_c	$48 - 96$ kN m^{-2}
	Hunke [2001][a]	P	27.5×10^4 kN m^{-2}
	Dumont et al. [2008]	P^*	27.5 kN m^{-2}
	Bouillon and Rampal [2015]	$\sigma_{Nmin} = -\frac{5}{2}c$	$1.25 - 20$ kN m^{-2}
	Tremblay and Mysak [1997]	P_{max}	7 kN m^{-2}
	Hibler [1979]	P^*	5.0 kN m^{-2}

Table 3.3: Table 3.3 continued

Parameter	Reference	Parameter	Value
Shear strength :	*Hibler* [1979]	e	2
	Hunke [2001]	e	2
	Dumont et al. [2008]	e	$1.2 - 1.6$
	Lemieux et al. [2016]	e	$1.4 - 1.6$
	Olason [2016]	e	$1.3 - 2.1$
	Dansereau et al. [2016]	C	$25 - 50$ kN m^{-2}
	Olason [2016][b]	σ_{uc}	$16 - 22$ kN m^{-2}
	Tran et al. [2015]	τ_{sf}	$15 - 75$ kN m^{-2}
	Sulsky and Peterson [2011]	τ_{sf}	15 kN m^{-2}
	Bouillon and Rampal [2015]	c	$0.5 - 8$ kN m^{-2}
Tensile strength	*Olason* [2016][b]	Pk_t	$3.4 - 5$ kN m^{-2}
	Lemieux et al. [2016]	$k_t P_p$	$10 - 20$ kN m^{-2}
	Beatty and Holland [2010]	k_t	27.5 kN m^{-2}
	Dansereau et al. [2016]	$\sigma_t = 0.27\sigma_c$	$12.96 - 25.92$ kN m^{-2}
	Tran et al. [2015]	τ_{nf}	25 kN m^{-2}
	Sulsky and Peterson [2011]	τ_{nf}	25 kN m^{-2}
	Bouillon and Rampal [2015]	$\sigma_{Nmax} = \frac{5}{4}c$	$0.6 - 10$ kN m^{-2}

[a]for 1m thick ice

[b]Using the Mohr-Coulomb curve with $\phi = 45°$

3.2.2 Rheology

3.2.2.1 Visco-elastic regime

Following *Dansereau et al.* [2016], we consider the ice as a visco-elastic-brittle material behaving like a stiff spring and strong dash-pot in series if the stresses are relatively small. The corresponding stress-strain relation is that of a Maxwell visco-elastic material:

$$\frac{\partial \boldsymbol{\sigma}}{\partial t} + \frac{1}{\lambda}\boldsymbol{\sigma} = E\mathbf{C} : \dot{\boldsymbol{\epsilon}}, \tag{3.7}$$

where λ is the viscous time relaxation ($\lambda = \frac{\eta}{E}$, η being the vertically integrated viscosity), E is the vertically integrated Elastic Stiffness, $\mathbf{C}$ is the elastic modulus tensor and ":" denotes the double dot product of tensors. In generalized matrix form, the tensors $\mathbf{C}$ and $\dot{\epsilon}$ are written as:

$$\mathbf{C} = \frac{1}{1-\nu^2}\begin{pmatrix} 1 & \nu & 0 \\ \nu & 1 & 0 \\ 0 & 0 & 1-\nu \end{pmatrix} = \begin{pmatrix} C_1 & C_2 & 0 \\ C_2 & C_1 & 0 \\ 0 & 0 & C_3 \end{pmatrix} \tag{3.8}$$

$$\begin{pmatrix} \dot{\epsilon}_{11} \\ \dot{\epsilon}_{22} \\ \dot{\epsilon}_{12} \end{pmatrix} = \begin{pmatrix} \frac{\partial u}{\partial x} \\ \frac{\partial v}{\partial y} \\ \frac{1}{2}\left(\frac{\partial u}{\partial y} + \frac{\partial v}{\partial x}\right). \end{pmatrix} \tag{3.9}$$

where ν ($= 0.33$) is the Poisson ratio. The components of the elastic modulus tensor $\mathbf{C}$ are derived using the plane stress approximation (i.e., following the original assumption that the vertical stress components are negligible, see for instance *Rice* 2010). Note that we neglect the advection of stress in the time derivative of Eq. 3.7 as we focus on landfast ice.

The visco-elastic regime of the MEB model (before fracture) is dominated by a fast and reversible elastic response (first term on the left hand side of Eq. 3.7), with a slow viscous dissipation acting over longer time scales (second term on the left hand side). The reversibility of the elastic deformations implies that the elastic strains return to zero if all loads are removed. This results from a memory of the previous elastic stress and strain states given by the time-derivative in Eq. 3.7. The Maxwell viscosity term, although orders of magnitude lower than the other terms in the visco-elastic regime, leads to a slow viscous dissipation of this elastic stress memory over long timescales determined by λ (days in our case).

While Eq. 3.7 is similar in form to the stress-strain relationship of the Elastic Viscous Plastic (EVP) model [*Hunke*, 2001], the elastic component in the EVP model was introduced to improve the computational efficiency of the VP model by allowing for an explicit numerical scheme and efficient parallelization [*Hunke and Dukowicz*, 1997]. In the MEB model, the elastic component represents the elastic behavior of sea ice while the viscous relaxation component is introduced to dissipate the elastic strains into permanent deformations. The use of a viscous component is consistent with the observation of viscous creep [*Tabata*, 1955; *Weeks and Assur*, 1967] and viscous relaxation in field experiments [*Tucker and Perovich*, 1992; *Sukhorukov*, 1996; *Hata and Tremblay*, 2015a]. The viscous relaxation term is also analogous to the viscous term in the thermal stress models of *Lewis* [1993] and *Hata and Tremblay* [2015b].

3.2.2.2 Damage parameterization

In the MEB model, the brittle fracture is simulated using a damage parameterization, which is based on progressive damage models originally developed in the field of rock mechanics to reproduce the non-linear (brittle) behavior in rock deformation and seismicity [*Cowie et al.*, 1993; *Tang*, 1997; *Amitrano and Helmstetter*, 2006]. In these models, the material damage associated with microcracking is simulated by altering the material properties (e.g. the Young Modulus or the material strength) at the model element (or local) scale. If heterogeneity is present in the material, the damage parameterization simulates the self-organisation of the microcracks in a macroscopic line of fracture, as observed in laboratory experiments. It was first used for large scale sea ice modeling by *Girard et al.* [2011] and is now implemented in the Lagrangian dynamic-thermodynamic sea ice model neXtSIM [*Rampal et al.*, 2019].

The sea ice deformations associated with the brittle fractures are parameterized by a gradual decrease in the elastic stiffness E and viscosity η at the local scale, and consequently as a local increase in the magnitude of the deformation associated with a given stress state. The local increase in deformations results in the concentration of internal stresses in adjacent grid cells, leading to the propagation of the fractures in space. The decrease in elastic stiffness and viscosity is set by a damage parameter d representing the weakening of the ice upon fracturing [*Bouillon and Rampal*, 2015]. The damage parameter has a value of 0 for undamaged sea ice and 1 for fully damaged ice.

The damage increases when the stress state exceeds a critical stress, defined by the Mohr-Coulomb criterion. This yield criterion is standard for granular materials and in agreement with laboratory experiments [*Schulson et al.*, 2006] and field observations [*Weiss et al.*, 2007]. We also investigate the use of a compressive cut-off to limit the uniaxial compression ($\sigma_2 = \sigma_I - \sigma II$, see Fig. 3.2). In terms of the stress invariants σ_I and σ_{II}, this can be written as:

$$F(\sigma) = \begin{cases} \sigma_{II} + \mu\sigma_I - c \quad < \quad 0 & \text{Mohr Coulomb} \\ \sigma_I - \sigma_{II} \quad > \quad \sigma_c h e^{-C(1-A)} & \text{Compression cut-off} \end{cases} \tag{3.10}$$

where

$$c = c_0 h e^{-a(1-A)}, \tag{3.11}$$

$$\sigma_c = \sigma_{c0} h e^{-a(1-A)}, \tag{3.12}$$

σ_I is the isotropic normal stress (defined as negative in compression), σ_{II} is the maximum shear stress, c is the vertically-integrated cohesion, μ ($= \sin\phi$) is the coefficient of internal friction of ice, ϕ is the angle of internal friction and σ_c is the vertically-integrated uniaxial compressive strength. The parameterization of c and σ_c follows the form of the internal

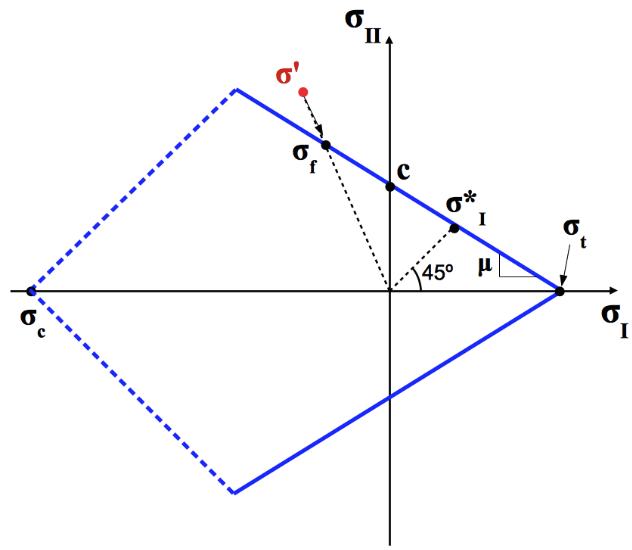

Figure 3.2: Yield criterion (Mohr-Coulomb and compressive cut-off) in stress invariant space (σ_I,σ_{II}) with the mechanical strength parameters: compressive strength (σ_c), cohesion (c), coefficient of internal friction ($\mu = \sin\phi$, ϕ being the angle of internal friction), isotropic tensile strength (σ_t) and uniaxial tensile strength (σ_I^*, where the second principal stress invariant σ_2 is zero, or $\sigma_I = \sigma_{II} = \sigma_I^*$). The stress before and after the correction (see Eq. 3.13) is denoted by σ', and σ_f respectively. The correction from σ' to σ_f is done following a line going through the origin.

sea ice pressure in the standard VP model with the ice concentration parameter a set to 20 [*Hibler*, 1979]. The cohesion c_0 and compressive strength σ_{c_0} are the material properties derived from in-situ observations (see Table 3.1 for values and references) and laboratory experiments [*Timco and Weeks*, 2010]. Model parameters used in this and other studies are listed in Tables 3.2 and 3.3.

Following *Rampal et al.* [2016], the introduction of damage upon failure is proportional to the local stress in excess of the yield criterion. A damage factor Ψ ($0 < \Psi < 1$) is used to scale the stress back on the yield curve. It is defined as (see appendix 3.6.1 for the derivation Ψ) :

$$\boldsymbol{\sigma}_f = \Psi\boldsymbol{\sigma}' \qquad \text{with} \qquad \Psi = \min\left(1, \frac{c}{\sigma'_{II} + \mu\sigma'_I}, \frac{\sigma_c}{\sigma'_I - \sigma'_{II}}\right), \tag{3.13}$$

where $\boldsymbol{\sigma}_f$ is the corrected stress lying on the yield curve and $\boldsymbol{\sigma}'$ is the prior stress state that exceeds the yield criterion. Note that the stress components are all scaled by the same damage factor, such that the path of the stress correction in stress invariant space follows a line from the uncorrected stress state to the origin (see Fig. 3.2). The stress correction path does not correspond to a flow rule: the magnitude of the excess stress is only used to increase the damage parameter. It determines the magnitude of the strain associated with a stress state, but otherwise does not change the visco-elastic relationship in Eq. 3.7.

The temporal evolution of the damage parameter follows a simple relaxation with a damage time scale T_d [*Dansereau et al.*, 2016]:

$$\frac{\partial d}{\partial t} = \frac{(1-\Psi)(1-d)}{T_d}, \tag{3.14}$$

where T_d is set to the advective time scale associated with the propagation of elastic waves in undamaged ice (i.e., $T_d = \Delta x / c_e$, Δx being the spatial resolution of the model and c_e the elastic wave speed). Consequently, the damage at any given time is a function of the previously accumulated damage. No damage healing process was included in this study as we focus on the break up of ice bridges at small time scales. For the same reason, the advection of damage is neglected. The relaxation time scale ($T_d/(\Psi - 1)$) in Eq. (3.14) is time-step dependent via its dependency on the damage factor Ψ. That is, a larger time step yields larger stress increments and larger excess stresses at each time-level, decreasing the time scale for the damage relaxation. The sensitivity of the damage parameterization on the model time step led *Dansereau et al.* [2016] to suggest that the model time step be set to exactly T_d, otherwise the damage could travel faster than the elastic waves. We argue that while this point is true when using a fixed damage reduction parameter (as in *Amitrano et al.* 1999; *Girard et al.* 2011), the use of a damage factor Ψ relates the damage parameter to the rate of changes in the stress state, which is associated with the propagation of elastic waves. The propagation of damage in space is thus bounded by the elastic wave speed, and a smaller time-step (0.5 s in this study) should be used to respect the CFL criterion associated to the elastic waves.

The Elastic stiffness E and Maxwell viscosity η are written as a non-linear function of d, with a dependency on the ice thickness and sea ice concentration inspired by the ice strength parameterization of *Hibler* [1979]:

$$E = Yhe^{-a(1-A)}(1-d), \tag{3.15}$$

$$\eta = \eta_0 h(1-d)^{\alpha}, \tag{3.16}$$

where Y (= 1 GN m^{-2}, smaller than in *Bouillon and Rampal* 2015 and similar to *Dansereau et al.* 2016, see Table 3.3) is the Young Modulus of undeformed sea ice, η_0 is the viscosity of undeformed sea ice and α is an integer set to 4 that determines the smoothness of the transition from visco-elastic behavior to the post-fracture viscous behavior [*Dansereau et al.*, 2016]. Note that E and η are defined as in previous implementations except for the linear dependence in ice thickness required because of the use of vertically integrated stress σ.

The relaxation time constant λ in Eq. 3.7 is then written as:

$$\lambda = \frac{\eta}{E} = \frac{\lambda_0(1-d)^{\alpha-1}}{e^{-a(1-A)}}, \tag{3.17}$$

where λ_0 [$= \eta_0/Y = 10^5$ s, smaller than in *Dansereau et al.*, 2016, but in agreement with observations, see Table 3.1] is a parameter that corresponds to the viscous relaxation time scale in undamaged sea ice. In the limit when λ_0 tends to infinity, the MEB rheology tends to the Elasto-Brittle rheology [*Girard et al.*, 2011].

Note that when a fracture is developing, the stress state is constantly brought back to the yield curve while the damage and the deformation increase. This is comparable to the plastic regime of the standard VP model of *Hibler* [1979]: in the VP model, the non-linear bulk and shear viscous coefficients reduce with increasing strain rates, such that the stress state (the product of the two) remains on the yield curve while the deformation increases. However, the plastic deformations in the VP model are defined by a normal flow rule, which also determines the orientation of the strain rate tensor [*Bouchat and Tremblay*, 2017; *Ringeisen et al.*, 2019]. In the MEB model, the large deformation associated to the damage is governed by the visco-elastic relationship of Eq. 3.7 and the yield curve does not directly determine the orientation of the strain rate tensor. The two models also differ post fracturing: the VP model does not have a memory of past deformations other than via the continuity equation and its impact on the ice thickness and concentration. In the MEB rheology, the damage corresponds to a material memory of past deformations even if the thickness and concentration remain unchanged.

The non-linear relationship of the viscous relaxation time scale on d and A ensures that the viscous term is very small in undamaged ice, and dominant in heavily damaged ice (see Eq. 3.7, where λ appears in the denominator). In this case, the deformations are large, irreversible and viscous. This is different from the standard VP and EVP models in which there is no change in the constitutive equation before or after the ice fracture. The dependency of λ on the ice concentration also ensures that the total stress tends toward zero for low concentration (i.e. in free drift), but not in a continuous ($A \sim 1$) but heavily damaged ice.

3.2.3 Numerical approaches

This model was coded using an Eulerian, FD, implicit numerical scheme, and is the first implementation of the MEB model on the same numerical framework as the standard VP model. This implementation was motivated by the need for a direct comparison between the VP and the MEB rheologies independently from the different numerical approaches. It presents a significant change from previous implementations that use Finite Element methods with a triangular mesh [*Rampal et al.*, 2016; *Dansereau et al.*, 2016] and/or Lagrangian advection scheme [*Rampal et al.*, 2016]. In the standard VP numerical framework, the stress components do not appear explicitly in the momentum equation. Instead they are written in terms of the non-linear viscous coefficients and strain-rates. For the MEB model, this is accomplished by treating the stress memory term from the time derivation of Eq. 3.7 as an additional forcing term. The damage parameterization is therefore the only new module to be coded.

3.2.3.1 Time discretization

The model equations are discretized in time using a semi-implicit backward Euler scheme. The uncorrected stress at time level n can then be written using Eq. 3.7, as:

$$\begin{aligned}\boldsymbol{\sigma}'^{n} &= \frac{1}{1+\Delta t/\lambda^{n}}\left[E^{n}\Delta t\mathbf{C}:\dot{\boldsymbol{\epsilon}}^{n}+\boldsymbol{\sigma}^{n-1}\right]\\ &= \xi^{n}\mathbf{C}:\dot{\boldsymbol{\epsilon}}^{n}+\gamma^{n}\boldsymbol{\sigma}^{n-1},\end{aligned} \tag{3.18}$$

where $n-1$ is the previous time level and where:

$$\xi^{n}=\gamma^{n}E^{n}\Delta t \qquad ; \qquad \gamma^{n}=(1+\Delta t/\lambda^{n})^{-1}. \tag{3.19}$$

Note that σ'^{n} is a function of σ^{n-1}, which we refer to as the stress memory. Equation 3.18 is then substituted in the stress divergence term of Eq. 3.1, so that the x and y components of the momentum equation can be expanded as :

$$\rho_i h^{n}\frac{u^{n}-u^{n-1}}{\Delta t} = \frac{\partial}{\partial x}\left(\xi^{n}C_1\epsilon^{n}_{xx}\right)+\frac{\partial}{\partial x}\left(\xi^{n}C_2\epsilon^{n}_{yy}\right)+\frac{\partial}{\partial y}\left(\xi^{n}C_3\epsilon^{n}_{xy}\right)+\tau^{n}_{x}, \tag{3.20}$$

$$\rho_i h^{n}\frac{v^{n}-v^{n-1}}{\Delta t} = \frac{\partial}{\partial y}\left(\xi^{n}C_1\epsilon^{n}_{yy}\right)+\frac{\partial}{\partial y}\left(\xi^{n}C_2\epsilon^{n}_{xx}\right)+\frac{\partial}{\partial x}\left(\xi^{n}C_3\epsilon^{n}_{xy}\right)+\tau^{n}_{y}, \tag{3.21}$$

where C_1, C_2, and C_3 are the components of the tensor C (Eq. 3.8) and where the stress memory terms have been included in the forcing, that is :

$$\tau_x^n = \frac{\partial\left(\gamma^n \sigma_{xx}^{n-1}\right)}{\partial x} + \frac{\partial\left(\gamma^n \sigma_{xy}^{n-1}\right)}{\partial y} + \tau_{ax}^n + \tau_{wx}^n, \tag{3.22}$$

$$\tau_y^n = \frac{\partial\left(\gamma^n \sigma_{yy}^{n-1}\right)}{\partial y} + \frac{\partial\left(\gamma^n \sigma_{xy}^{n-1}\right)}{\partial x} + \tau_{ay}^n + \tau_{wy}^n. \tag{3.23}$$

The MEB rheology equations can then be implemented in a VP model by setting the VP bulk and shear viscosity to $\zeta_{VP} = \xi\frac{C_1+C2}{2}$ and $\eta_{VP} = \xi C_3$ respectively, setting the pressure term $P = 0$ and adding the stress memory terms.

The variable E^n and λ^n in Eq. 3.18 to 3.21 are discretized explicitely, as:

$$E^n = E_0 h^n d^n e^{-c(1-A^n)}, \tag{3.24}$$

$$\lambda^n = \frac{\lambda_0 (d^n)^{\alpha-1}}{h^n e^{-C(1-A^n)}}, \tag{3.25}$$

using

$$h^n = h^{n-1} + \nabla \cdot (\mathbf{v}^n h^{n-1} \Delta t), \tag{3.26}$$

$$A^n = A^{n-1} + \nabla \cdot (\mathbf{v}^n A^{n-1} \Delta t), \tag{3.27}$$

$$d^n = d^{n-1} + \frac{d^{n-1}\Delta t}{T_d}(\Psi^n - 1), \tag{3.28}$$

$$\Psi^n = \min\left(1, \frac{c^n}{\sigma_{II}'^n + \mu\sigma_I'^n}, \frac{\sigma_c^n}{\sigma_I'^n - \sigma_{II}'^n}\right), \tag{3.29}$$

$$c^n = c_0 h^n e^{-C(1-A^n)}, \tag{3.30}$$

$$\sigma_c^n = \sigma_{c_0} h^n e^{-C(1-A^n)}, \tag{3.31}$$

3.2.3.2 Space discretization

The model equations are discretized in space using a centered finite different scheme on an Arakawa C-grid. In this grid, the diagonal terms of the σ and $\dot{\epsilon}$ tensors are naturally computed at the cell centers and the off-diagonal terms at the grid nodes. The x-component of the momentum equation are written as :

$$\rho_i h_{i,j}^{n-1} \frac{u_{i,j}^n - u_{i,j}^{n-1}}{\Delta t} = C_1 \frac{\left(\xi^{n-1}\epsilon_{xx}^n\right)_{i,j} - \left(\xi^{n-1}\epsilon_{xx}^n\right)_{i-1,j}}{\Delta x} + C_2 \frac{\left(\xi^{n-1}\epsilon_{yy}^n\right)_{i,j} - \left(\xi^{n-1}\epsilon_{yy}^n\right)_{i-1,j}}{\Delta x} + C_3 \frac{\left(\xi_z^{n-1}\epsilon_{xy}^n\right)_{i,j+1} - \left(\xi_z^{n-1}\epsilon_{xy}^n\right)_{i,j}}{\Delta y} + \tau_{x\,i,j}^n \tag{3.32}$$

where :

$$(\dot{\epsilon}_{xx}^n)_{i,j} = \frac{u_{i+1,j}^n - u_{i,j}^n}{\Delta x}, \tag{3.33}$$

$$(\dot{\epsilon}_{yy}^n)_{i,j} = \frac{v_{i,j+1}^n - v_{i,j}^n}{\Delta y}, \tag{3.34}$$

$$(\dot{\epsilon}_{xy}^n)_{i,j} = \frac{u_{i,j}^n - u_{i,j-1}^n}{2\Delta y} + \frac{v_{i,j}^n - v_{i-1,j}^n}{2\Delta x}, \tag{3.35}$$

$$\tau_{x\,i,j}^n = \frac{\left(\gamma^{n-1}\sigma_{xx}^{n-1}\right)_{i,j} - \left(\gamma^{n-1}\sigma_{xx}^{n-1}\right)_{i-1,j}}{\Delta x} + \frac{\left(\gamma_z^{n-1}\sigma_{xy}^{n-1}\right)_{i,j+1} - \left(\gamma_z^{n-1}\sigma_{xy}^{n-1}\right)_{i,j}}{\Delta y} + \tau_{ax\,i,j}^n + \tau_{wx\,i,j}^n. \tag{3.36}$$

The shear terms in Eq. 3.32 and 3.36 ($\dot{\epsilon}_{xy}$, ξ_z and γ_z) are thus defined at the lower-left grid node rather than at the grid center. The staggering of the stress components is unavoidable when using the C-grid, and requires node approximations for the scalar values h, A and d [*Losch et al.*, 2010]. This is treated on our Cartesian grid with square cells by approximating the scalar prognostic variables at the nodes (h_z, A_z and d_z) using a simple average of the neighbouring cell centres, i.e. :

$$h_z = \overline{h}_{i,j} = \frac{h_{i,j} + h_{i-1,j} + h_{i,j-1} + h_{i-1,j-1}}{4}, \tag{3.37}$$

and similarly for A_z and d_z. The stress-strain coefficients ξ_z and γ_z are then computed using (h_z, A_z and d_z) in Eq. 3.15, 3.17 and 3.19.

The shear stress at the cell centre must also be approximated when computing the stress invariants in the stress correction scheme (Eq. 3.13). Averaging the shear stress components from the neighboring nodes (as in Eq. 3.37 for the scalars) causes a checker board instability in the solution, because of the staggered shear stress corrections and memories. To avoid this, the mean shear stress at the cell center is defined using an average of the neighboring shear stress increments ($\xi_z^n \dot{\epsilon}_{xy}^n$), which are integrated in another shear stress memory term, defined at the grid center. That is:

$$\sigma'^n_{xy\ i,j}|_C = \overline{\left(\xi_z^n \dot{\epsilon}_{xy}^n\right)}_{i,j} + \gamma^{n-1} \sigma^{n-1}_{xy\ i,j}|_C, \tag{3.38}$$

where $\sigma'^n_{xy\ i,j}|_C$ is the uncorrected shear stress at the grid center, $\overline{\left(\xi_z^n \dot{\epsilon}_{xy}^n\right)}_{i,j}$ is the shear stress increment averaged as in Eq. 3.37 and $\sigma^{n-1}_{xy\ i,j}|_C$ is the corrected shear stress at the grid center from the previous time step. Note that the approximations in Eqs. 3.37 and 3.38 are required due to the use of a FD scheme, a notable difference with the other MEB implementations using Finite Element Methods [*Dansereau et al.*, 2016; *Rampal et al.*, 2019].

3.2.3.3 Numerical solution

With nx tracer points in the x-direction and ny in the y-direction, the spatial discretization on our C-grid leads to a system of $N = (ny(nx+1) + nx(ny+1))$ non-linear equations for the velocity components. By stacking all the u components followed by the v ones, we form the vector $\boldsymbol{u}$ of size N. The non-linear system of equations (momentum) for $\boldsymbol{u}^n$ and the other discretized equations (Eqs. 3.24-3.31) are solved simultaneously using an IMplicit-EXplicit (IMEX) approach [*Lemieux et al.*, 2014]. As described in the algorithm below, this procedure is based on a Picard solver [*Lemieux et al.*, 2008] which involves an Outer Loop (OL) iteration. At each OL iteration k, the non-linear system of equations is linearized and solved using a preconditioned Flexible General Minimum RESidual method (FGMRES). The latest iterate $\boldsymbol{u}^k$ is used to solve explicitly the damage and continuity equations. This iterative process is conducted until the L2-norm of the solution residual falls below a set tolerance of $\epsilon_{res} = 10^{-10}$ N m^{-2}. The uncorrected stresses $\boldsymbol{\sigma}'^{n}$ is then scaled by the damage factor Ψ^n and stored as the stress memory $\boldsymbol{\sigma}^n$ for the following time step. This numerical scheme differs from that of *Dansereau et al.* [2017] who solve the equations using tracers (h,A,d) from the previous time level.

1. Start with initial iterate $\mathbf{u}^0$

do $k = 1$, k_{max}

2. Linearize the non-linear system of equations using $\boldsymbol{u}^{n,k-1}$, $h^{n,k-1}$, $A^{n,k-1}$ and $d^{n,k-1}$
3. Calculate $\boldsymbol{u}^{n,k}$ by solving the linear system of equations with FGMRES
4. Calculate $\Psi^{n,k} = f(\boldsymbol{\sigma}'^{n,k})$
5. Calculate $h^{k,n} = f(h^{n,k-1}, \boldsymbol{u}^{n,k})$, $A^{n,k} = f(A^{n,k-1}, \boldsymbol{u}^{n,k})$, $d^{n,k} = f(d^{n,k-1}, \boldsymbol{u}^{n,k}, \Psi^{n,k})$
6. Calculate $E^{k,n} = f(d^{n,k}, h^{n,k}, A^{n,k})$, $\lambda^{n,k} = f(d^{n,k}, h^{n,k}, A^{n,k})$
7. If the Picard solver converged to a residual $< \epsilon_{res}$, stop.

enddo

8. Update the stress memory $\boldsymbol{\sigma}^n = \Psi^n \boldsymbol{\sigma}'^{n}$

where a simple upstream advection scheme is used for $h^{k,n}$ and $A^{k,n}$ in step 5. Note that steps 4, 5, 6 and 8 are performed for all the grid points.

3.3 Results

In the following, we present a series of idealized simulations to document the formation and break-up of ice arches with the MEB rheology, and their sensitivity to the choice of mechanical strength parameters. Results from these simulations and observations are used to constrain the material parameters used in sea ice models. Here, we define an ice arch as the location of the discontinuity in the sea ice velocity (and later in the ice thickness and concentration fields) and the ice bridge as the landfast ice upstream of the ice arch.

Our model domain is 800 x 200 km with a spatial resolution of 2 km (Fig. 3.3). The boundary conditions are periodic on the left and right, closed on the top and open on the bottom. Two islands, separated by a narrow channel 200 km long and 60 km wide, are located 300 km away from the top and bottom boundaries. The initial conditions for sea ice are zero ice velocity, uniform 1m ice thickness, 100 % concentration and zero damage. A southward forcing τ_{LFI} (see Eq. 3.4) is imposed on the ice surface, ramped up from 0 to 0.625 N m^{-2} (corresponding to 20 m s^{-1} winds or 0.33 m s^{-1} surface currents) in a 10h period, a rate well below the adjustment time scale associated with elastic waves. The solution can therefore be considered as steady state at all time, which allows us to determine the critical forcing associated with a fracture event.

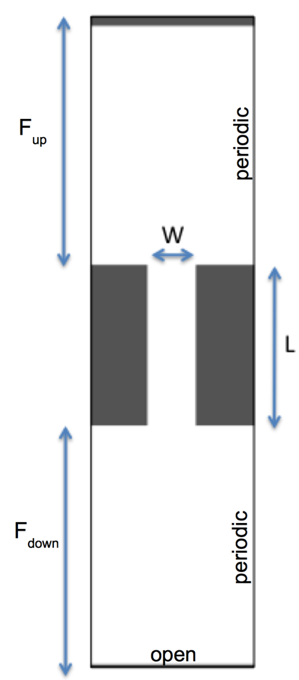

Figure 3.3: Idealized domain with a solid wall to the north, open boundary to the south and periodic boundaries to the East and West. The channel in the control simulation has a width W = 60 km, length L = 200 km and fetch F_{up} and F_{down} = 300 km in the upstream and downstream basins respectively.

3.3.1 Control run

The break up of landfast ice in our simulation proceeds through a series of fracture events that are highly localized in time (see Fig. 3.4) and space (see Fig. 3.5 and 3.6), separated by periods of elastic stress build up (low brittle failure activity). Two major fracture events are seen in the simulation (stage B and D in Fig. 3.4). The first corresponds to the failure of ice in tension with the development of an ice arch on the downstream side of the channel (Fig. 3.5). The damage occurs on very short time scales (within minutes), and preconditions the formation of an arching flaw lead downstream of the ice bridge over longer time scales (Fig. 3.5b), in accord with results from *Dansereau et al.* [2017]. The second event corresponds to the collapse of the landfast ice bridge with the break up of ice within and upstream of the channel (Fig. 3.6). As for the downstream ice arch, the lines of fractures are formed on short time scales and precondition the location of ridging on the advection time scale (Fig. 3.6b). The three remaining periods during which few new brittle fractures occur correspond to an elastic landfast ice regime (stage A), a stable downstream ice arch regime (stage C), and a drift ice regime when ice flows within, downstream and upstream of the channel (stage E).

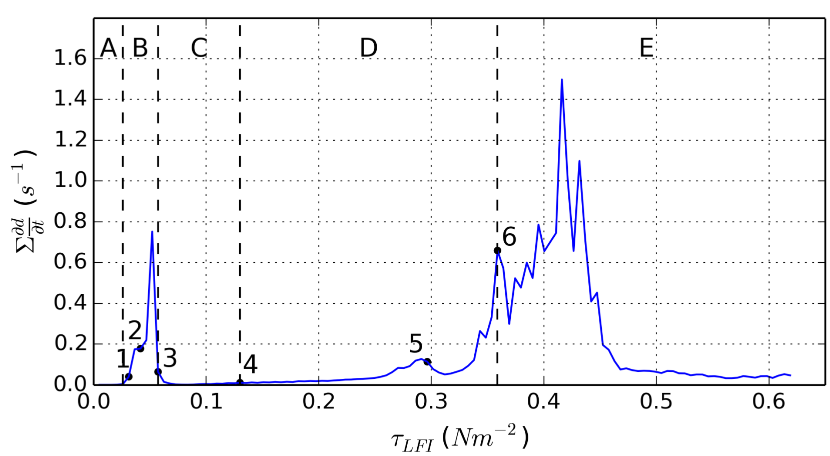

Figure 3.4: Time series of the domain integrated brittle fracture activity ($\partial d/\partial t$) for the control run simulation. Dashed lines indicate the beginning and end of the simulation phases (A,B,C,D,E), and numbers indicate the location of the damage field in Fig. 3.5 and 3.6.

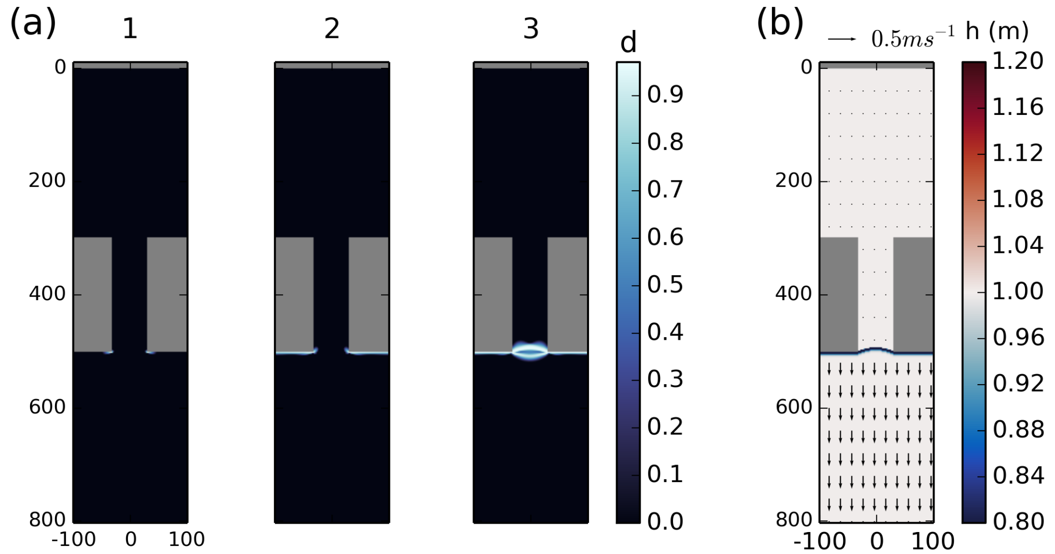

Figure 3.5: a) Damage field at the surface forcing indicated by points 1, 2 and 3 in Fig. 3.4, during the formation of the downstream ice arch. b) Sea ice thickness and drift following the formation of the downstream ice arch, while the ice bridge remains stable (Phase C)

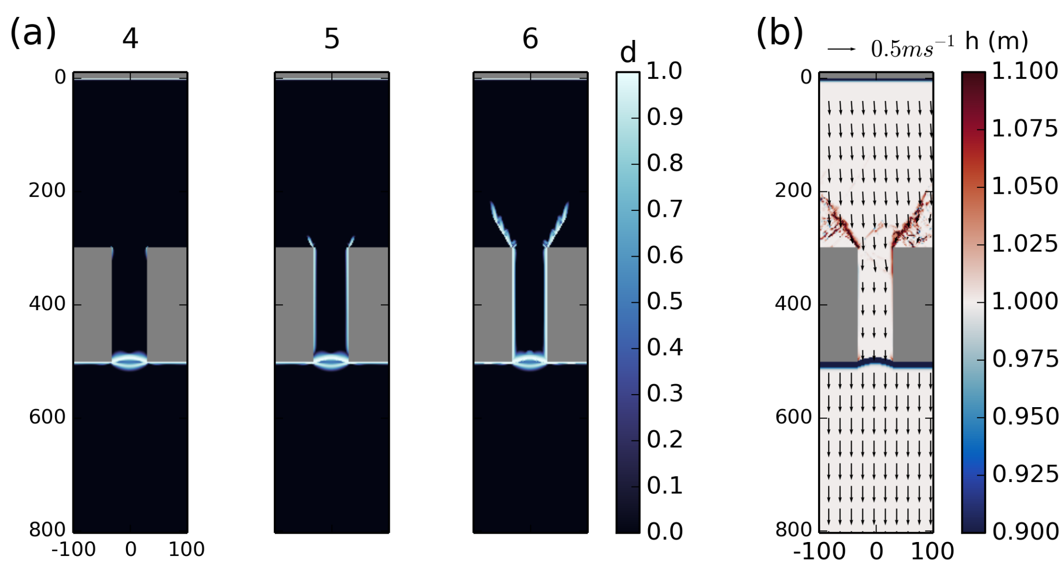

Figure 3.6: a) Damage field at the surface forcing indicated by points 4, 5 and 6 in Fig. 3.4, during the formation of the upstream lines of fracture. b) Sea ice thickness and drift following the ice bridge collapse (Phase E).

In the first stage of the simulation, elastic stress builds up but remains inside the yield curve in the entire domain such that there is no brittle failure activity (Fig. 3.4, stage A). The sea ice in the elastic regime behaves as an elastic plate and deformations are linearly related to the internal stresses. The elastic stresses are determined by the orientation of the surface forcing with respect to the coastlines: there are large tensile stresses on the downstream coastlines, compressive stresses on the upstream coastlines and shear stresses on the four corners of the channel (Fig. 3.7). At the vertical line of symmetry (away from channel openings, Fig. 3.7a, dashed blue line), the simulated stress field is in good agreement with the analytical solutions from a 1D version of the momentum equation, giving us confidence in the numerical implementation of the model (see Appendix 3.6.2 and Figure 3.8). Upstream and downstream of the channel, both stress invariants are important, reaching a maximum in magnitude at the channel corners and decreasing to a local minimum at the center of the channel. In this configuration, the second principal stress alignment (Fig. 3.7c) is along the x-direction downstream of the coastlines (where the ice is in uniaxial tension), and along the y-direction upstream of the coastlines (where the ice is in uniaxial compression). In the downstream end of channel, the second principal stress alignment follows the shape of an arch, transitioning to a vertical alignment towards the upstream channel entrance.

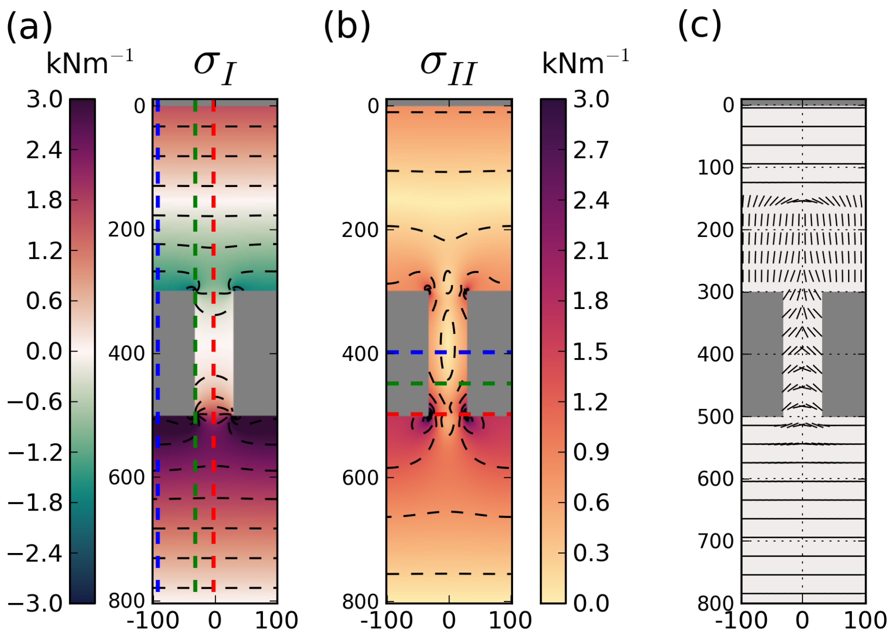

Figure 3.7: Stress fields in landfast ice during Phase A. a) Normal stress invariant (σ_I), with colored dashed lines to indicate the vertical transects used in Fig. 3.8, b) shear stress invariant (σ_{II}), with colored lines to indicate the horizontal transects used in Fig. 3.8, c) orientation of the second principal stress component.

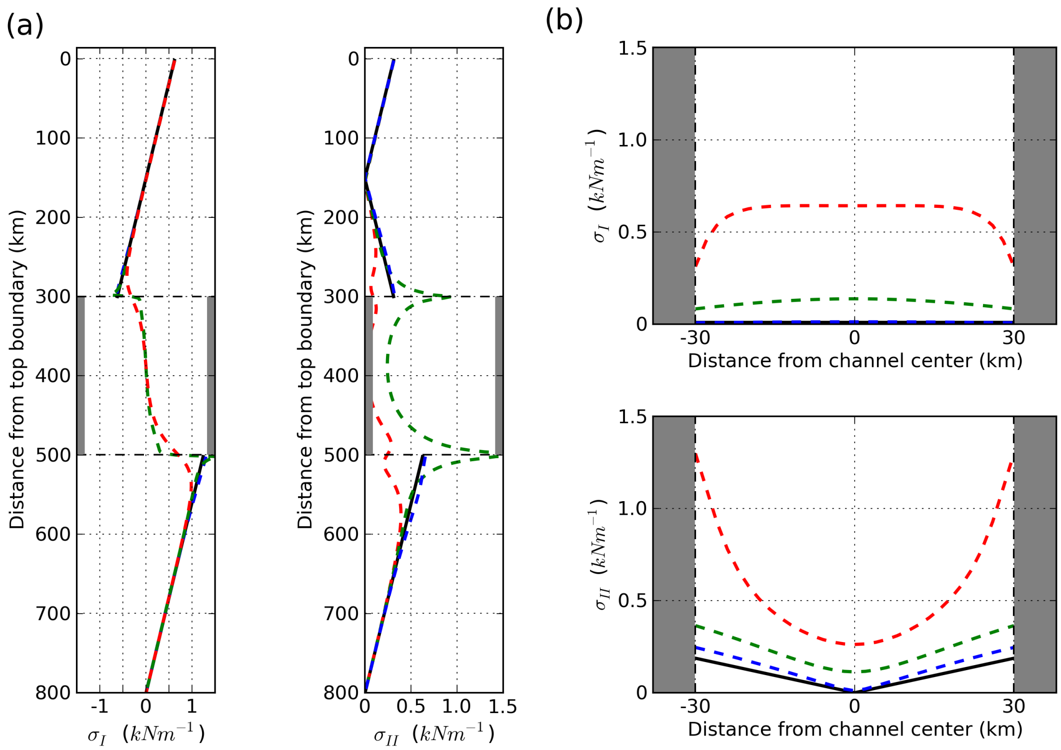

Figure 3.8: Stress invariants (σ_I, σ_{II}) along the transects of corresponding colors in Fig. 3.7: a) transects running along the y-direction and b) transects running along the x-direction. Black solid lines indicate the analytic solutions. Grey area indicate the position of the islands.

3.3.1.1 Downstream ice arch

The formation of the downstream ice arch is initiated at a surface forcing of ~ 0.02 N m^{-2}. The initial fractures are located at the downstream corners of the channel where the stress state reaches the critical shear strength for positive (tensile) normal stresses. The fractures then propagate from these locations and form an arch (see Fig. 3.5a). The progression of the fracture into an ice arch is helped by the concentration of stresses at the channel corners and around the subsequent damage. That is, the damage permanently decreases the elastic stiffness, which leads to locally larger elastic deformations and increases the load in the surrounding areas, leading to the propagation of the fractures in space through regions where the internal stress state was originally sub-critical. To first order, the arching progression of the fracture from the channel corners follows the second principal stress direction (i.e. a failure in uniaxial tension on the plane perpendicular to the maximum tensile stress, see Fig. 3.7c). This differs from the expected angle of fracture in a coulombic material of $\theta = \pm(\pi/4 - \phi/2)$ from the second principal stress orientation [*Ringeisen et al.*, 2019], as reported in *Dansereau et al.* [2019].

A second period of low brittle fracture activity follows the formation of the ice arch (period C in Fig. 3.4). In this stage, the ice downstream of the ice arch is detached from the land boundaries and starts to drift. The non-zero brittle fracture activity in this stage is due to the increased damage in regions of already damaged ice; since the local stress state lies on the yield curve, the increasing forcing constantly increases the stress states beyond the yield criterion, leading to further damage. Upstream of the ice arch, the elastic stresses show little changes from stage A, except for their increase in magnitude due to higher forcing (Fig. 3.9). As the yield parameters (c, σ_c) are not function of the damage, tensile fracturing does not reduce the critical stress. This results in large tensile and shear stresses persisting along and north of the ice arch after its formation. The formation of a stress-free surface could be obtained by modifying the formulations of c and σ_{c0} such that they depend on the damage.

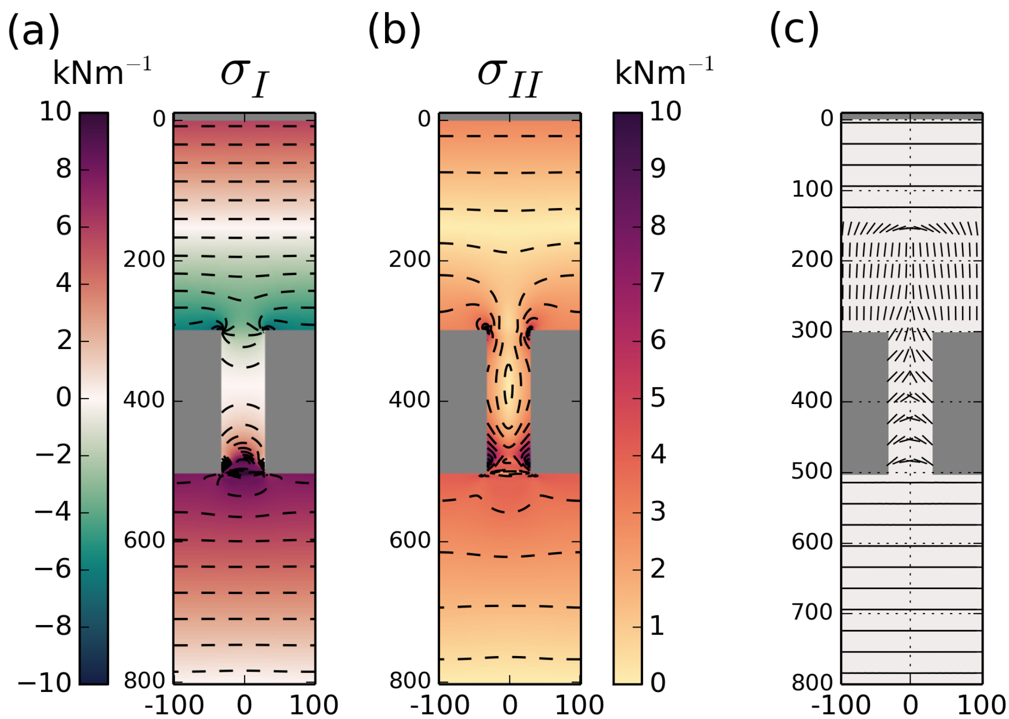

Figure 3.9: Stress fields during Phase C. a) Normal stress invariant (σ_I), b) shear stress invariant (σ_I), c) orientation of the second principal stress component.

3.3.1.2 Ice bridge collapse

The second break-up event (Stage D in Fig. 3.4) corresponds to the fracture of ice upstream of the channel and the collapse of the ice bridge. The fractures are initiated at a surface forcing of $0.13\ \mathrm{N\ m^{-2}}$ on the upstream corners of the islands where the internal stress reaches the critical shear strength for negative (compressive) normal stresses. The propagation of damage from these locations is composed of two separate fractures (see Fig. 3.6a). First, a shear fracture progresses downstream along the channel walls, resulting in the decohesion of the landfast ice in the channel from the channel walls. The decohesion of the ice bridge increases the load on the downstream ice arch and on the landfast ice upstream of the channel. Second, a shear fracture propagates upstream from the channel corners at an angle 58° from the coastline. The shear fracture orientation corresponds to an angle $\theta = 32°$ from the second principal stress orientation (Fig. 3.7c), which also deviates from the theoretical 22.5° in a granular material with $\phi = 45°$ [*Ringeisen et al.*, 2019].

Once the lines of fracture are completed, the ice bridge collapses and the ice in the channel starts to drift (stage E). In this stage, landfast ice only remains in two wedges of undeformed ice upstream from the islands in which high compressive stress remains present (see Fig. 3.10a). The remaining continuous areas of undamaged ice drift downward into the funnel as a solid body with uniform velocity, with ridges building at the fracture lines. The ridge building is highly localised (see Fig. 3.6b), but slowly expands in the direction perpendicular to the lines of fracture. This follows from the increase in material strength with ice thickness, resulting in larger compressive stresses along the ridge such that the ice fracture occurs in the neighboring thinner ice, in a succession of fracture events that are localised in time (see peaks in stage E, in Fig. 3.4).

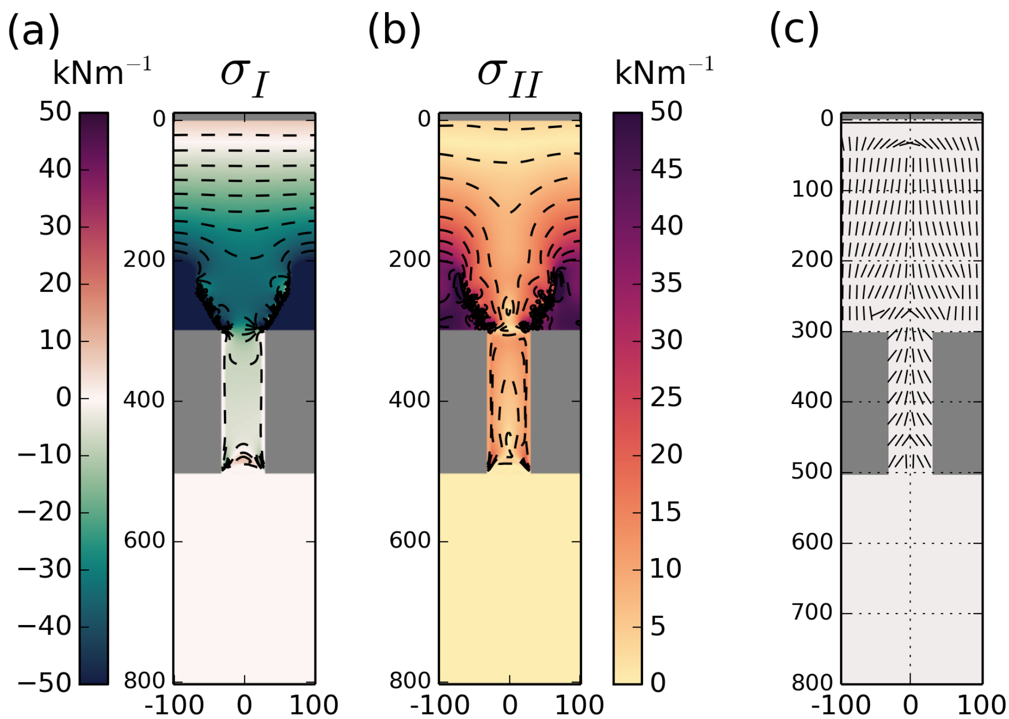

Figure 3.10: Stress fields during Phase E. a) Normal stress invariant (σ_I), b) shear stress invariant (σ_I), c) orientation of the second principal stress component.

3.3.2 Sensitivity to mechanical strength parameters

The Mohr-Coulomb yield criterion defines the shear strength of sea ice as a linear function of the normal stress on the fracture plane. In stress invariant coordinates (σ_I,σ_{II}), this can be written in terms of two material parameters: the cohesion c and the coefficient of internal friction $\mu = \sin\phi$ (Fig. 3.2). The isotropic tensile strength (i.e. the tip of the yield curve) is then a linear function of the two ($\sigma_t = c/\mu$). In this section, we investigate the influence of these material parameters and of the use of a uniaxial compressive strength criterion on the simulated ice bridge.

3.3.2.1 Cohesion

Changing only the cohesion c_0 (with a fixed internal angle of friction ϕ) moves the entire yield curve along the first stress invariant (σ_I) axis. For example, a higher cohesion increases the isotropic tensile strength $\sigma_{t_0} = c_0/\sin\phi$ and also increases the shear strength uniformly for all normal stress conditions. In the ice bridge simulations, the choice of cohesion influences the critical surface forcing associated with the different stages of the simulations but does not change the series of events described in section 3.3.1 or the orientation of the ice fractures. This is in agreement with results from *Dansereau et al.* [2017].

The critical surface forcing associated with the ice bridge break up can be related to the cohesion using the 1D steady state momentum equation (see Appendix 3.6.2 for details). Assuming an infinite channel running in the y-direction, the shear stress along the channel walls (σ_{xy}) is given by:

$$|\sigma_{xy}| = \sigma_{II} = \frac{\tau_{LFI} W}{2}, \tag{3.39}$$

where W is the channel width (see Fig. 3.3). Using the yield criterion (Eq. 3.10) with $\sigma_I = 0$ (i.e. $\sigma_{II} = c$), the maximum sustainable surface forcing τ_{LFIc} can be related to the cohesion as:

$$\tau_{ac} = \frac{2c}{W}. \tag{3.40}$$

In the simulations, the critical forcing for the complete decohesion of ice bridges (point 5 in Fig. 3.4 and 3.6) with different widths follows the simple 1D model (Fig. 3.11). This indicates that although the fracture is initiated at a weaker forcing due to the concentration of stress at the channel corners, the ice arch sustains the increasing load such that the ice bridge remains stable.

Given that ice bridges and arches with a width of $\sim$ 60 km are frequent in the CAA (e.g. Nares Strait, Lancaster Sound, or Prince Regent Inlet), and that the surface stresses regularly exceeds 0.15 N m^{-2} (e.g. corresponding to a wind speed of 10 m s^{-1} or a tidal current of $\sim$ 0.15 m s^{-1}), this suggests a lower bound on the cohesion of sea ice of at least 5 kN m^{-1} (see yellow curve in Fig. 3.11). Similarly, the fact that the ice bridges are rarely larger than 100 km (some are seen intermittently in the Kara Sea, *Divine et al.* 2004) indicates that the cohesion of sea ice should be smaller than 10 kN m^{-1} (see red curve in Fig. 3.11). This range (5-10 kN m^{-1}) is lower than records from ice stress buoys measurements, which measure both thermal and mechanical internal stresses at smaller scales [40kN m^{-2}, *Weiss et al.*, 2007], but agree with estimates from ice arch observations [*Sodhi*, 1997]. Note that higher forcing may be frequent in areas associated with strong tides, although these locations correspond to unstable landfast ice areas and recurrent polynyas [*Hannah et al.*, 2009]. Our estimates therefore provide a meaningful bound to be used in sea ice models.

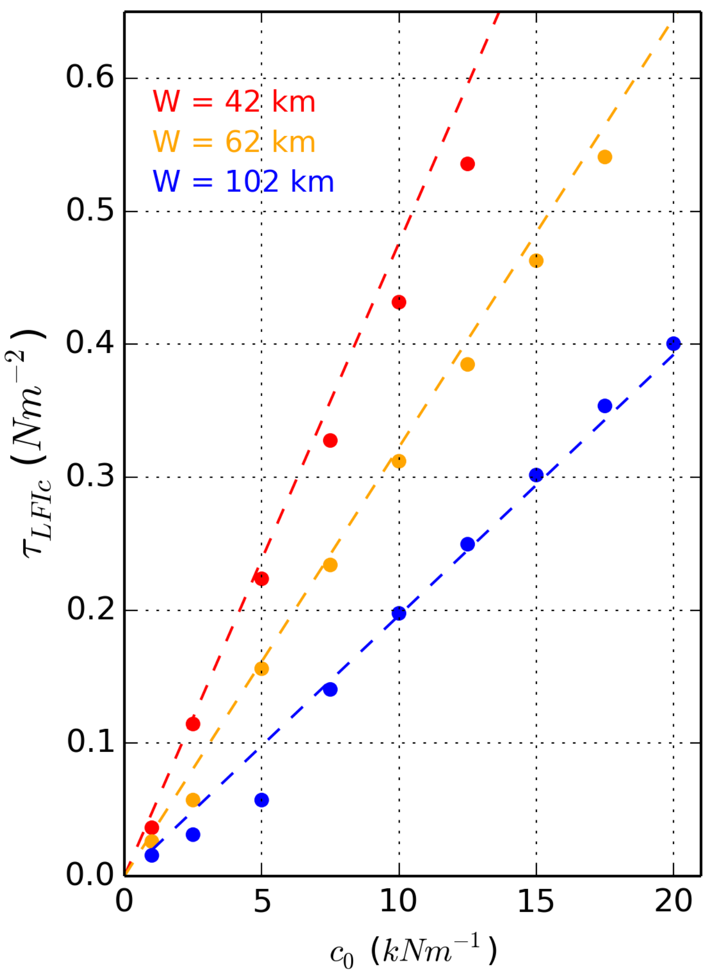

Figure 3.11: Critical surface forcing associated with the second fracture event (stage D) as a function of cohesion and channel width (dots). Dashed lines indicate the analytic solution from the 1D equations.

3.3.2.2 Angle of internal friction

The angle of internal friction ϕ, analogous to the static friction between two solids, determines the constant of proportionality between the shear strength and the normal stress ($\mu = \sin\phi$, see Eq. 3.10 and Fig. 3.2). Varying the angle of internal friction changes in opposite ways the shear strength of ice under tensile and compressive stresses: when increasing the angle of internal friction, the shear strength of ice in tension is reduced while that of ice in compression is increased (and vice versa). This affects the critical forcing associated with the downstream and upstream ice fractures. When decreasing ϕ, the downstream ice arch (stage B) forms under a stronger forcing, and a weaker forcing is required for the development of the upstream lines of fracture. As such, while the cohesion determines the stability of the landfast ice in the channel, the collapse of the ice bridge also requires the uniaxial fracture of ice upstream of the channel, which is sensitive to the angle of internal friction. The angle of internal friction also determines the shape of the ice fractures: decreasing ϕ leads to an increase in the curvature of the downstream ice arch and intensifies the departure of the upstream lines of fracture from the y-axis (see Fig .3.12). The simulated orientations of the fracture lines (32° and 45° for $\phi = 20°$ and 45°) differ from the orientations of 35° and 22.5° predicted by the Mohr-Coulomb theory, and do not vary linearly with the internal angle of friction.

3.3.2.3 Tensile strength

The yield curve modifications discussed above (varying c_0 and ϕ) also change the tensile strength (both uniaxial and isotropic) of ice. The tensile strength determines the magnitude of the critical surface forcing necessary for the formation of the downstream ice arch (stage B). The tensile stresses downstream from the islands can be approximated using the 1D version of the momentum equation as a function of the fetch distance F_{down} (see Fig. 3.3)

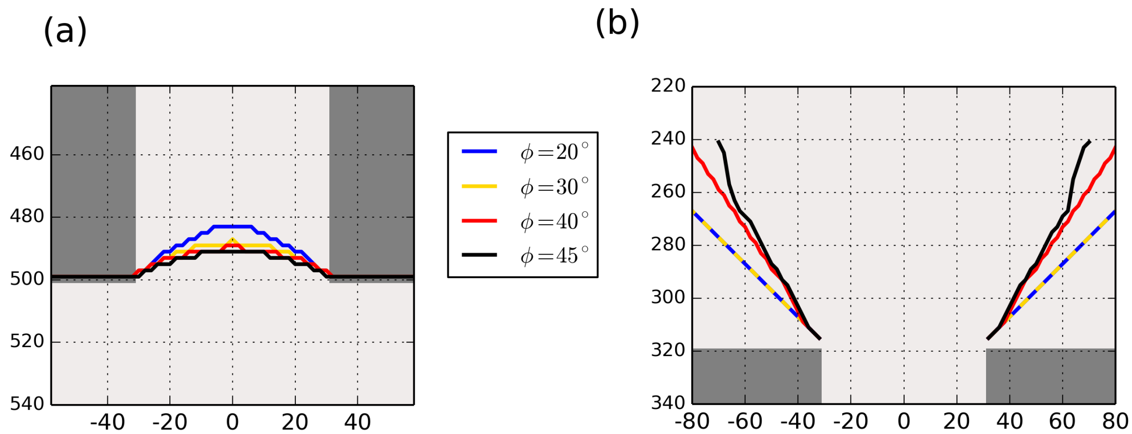

Figure 3.12: Shape of the lines of fracture using different angles of internal friction: a) for the downstream ice arches and b) for the upstream lines of fracture (the yellow and purple lines are superposed).

from the islands to the bottom boundary of the domain (derivation in Appendix 3.6.2):

$$\sigma_{yy} = \tau_{LFI} F_{down}. \tag{3.41}$$

This can be written as a function of the material parameters using a simplified Mohr Coulomb criterion (Eq. 3.10) for the 1D case (Appendix 3.6.2):

$$\sigma_{II} + \mu\sigma_I = \frac{1+2\mu}{3}\sigma_{yy} < c, \tag{3.42}$$

where $\nu = 1/3$ was used. Substituting σ_{yy} from Eq. 3.41 into Eq. 3.42, the yield criterion can be written in terms of the surface forcing and the material parameters:

$$\tau_{LFI} < \frac{3c}{F_{down}(2\mu+1)}, \tag{3.43}$$

Using our cohesion estimates ($5 < c < 10$ kN m^{-1}), angles of internal friction in the range of observations (30 and 45°) and a typical surface forcing of 0.15 N m^{-2} this would suggest stable bands of landfast ice of extent $F_{down} \sim$ 6-13 km to be sustainable. This is similar to observations in the Arctic, where bands of landfast ice rarely exceed a tens of kilometers unless anchor points are provided by stamukhi [*Mahoney et al.*, 2014].

3.3.2.4 Compressive strength criterion

Not used in other MEB implementations [*Dansereau et al.*, 2016, 2017], the compressive cut-off offers a limit on the simulated uniaxial compression, which can reach unrealistically large values and cause numerical instabilities (see section 3.4). Including a compressive strength criterion ($\sigma_I - \sigma_{II} > \sigma_c$) can modify the upstream fracture event (stage D) by the development of uniaxial compression fractures along the upstream coast of the islands, if the uniaxial compressive stress upstream of the islands exceeds the ice strength typically observed in the field ($\sim$ 40 kN m^{-2}, see Table 3.1). The critical surface forcing for the development of a compressive fracture can be approximated using the 1D version of the momentum equation. The maximum normal stress at the upstream coast of the islands is:

$$\sigma_{yy} = \tau_{LFI} F_{up}. \tag{3.44}$$

where F_{up} is the distance between the top boundary of the domain and the upstream coasts of the islands (see Fig. 3.3). In the ideal case, the compression strength criterion is:

$$\sigma_I - \sigma_{II} = \nu \sigma_{yy} > \sigma_c. \tag{3.45}$$

The compression criterion can thus be written as a function of the surface forcing, as:

$$\tau_{LFI} > \frac{\sigma_c}{\nu F_{up}}. \tag{3.46}$$

Whether the ice will fail in shear (Mohr-Coulomb criterion) or in compression can be evaluated by substituting τ_{LFI} from Eq. (3.39) into Eq. 3.46, yielding the criterion:

$$\frac{2\nu F_{up} c}{W} > \sigma_c. \tag{3.47}$$

If this condition is met, the compression strength criterion does not influence the simulation, and the upstream shear fracture lines develop as in the control simulation (Fig. 3.13a). If the left hand side of Eq. 3.47 is much smaller that σ_c, compression fracture occurs before the ice bridge break up and a ridge forms along the upstream coastlines, propagating in the channel entrance while the ice in the channel remains landfast (Fig. 3.13b). If the terms are of similar order, the decohesion of the ice bridge and the compression fractures are initiated simultaneously, such that the compression fracture occurs along the upstream coastlines but not in the channel entrance, as the ice starts to drift in and upstream of the channel (Fig. 3.13c).

3.4 Discussion

In the Arctic, ice arches are commonly observed upstream of narrow channels, where granular floes jam when forced into the narrowing passage. This requires the ice not to be landfast in the channel itself [*Vincent*, 2019], as opposed to the simulations presented above where the ice is initially landfast in the model domain. Contrary to results presented in *Dansereau et al.* [2017] where the presence of floes is simulated by a random seeding of weaknesses in the initial ice field, unstable ice arches upstream of the channel are not present in our simulations. Instead, our experiment simulates the propagation of ice fractures through the landfast ice upstream of a channel, which are akin to a failure in uniaxial compression [*Dansereau et al.*, 2016; *Ringeisen et al.*, 2019].

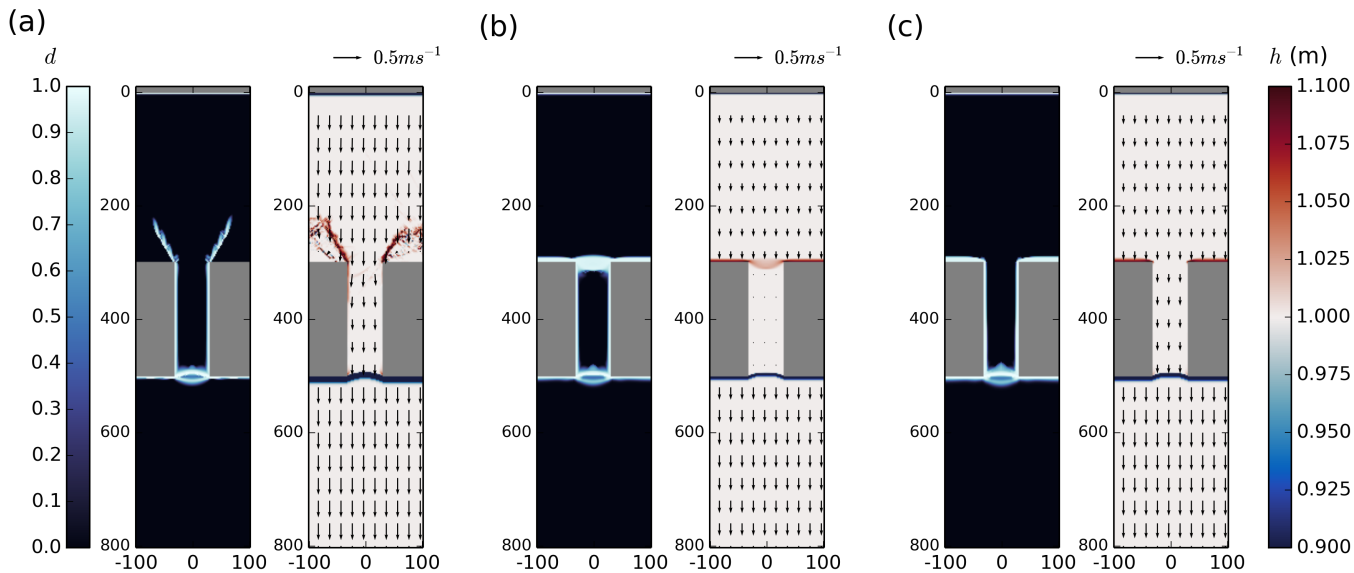

Figure 3.13: Spatial distribution of the damage field at the end of stage D (left) and the sea ice thickness and velocity fields at the end of the simulation (right). For different compressive strength criterion: a) $\sigma_{c_0} = 100.0$ kN m^{-1}, b) $\sigma_{c_0} = 5.0$ kN m^{-1} and c) $\sigma_{c_0} = 25.0$ kN m^{-1}.

In theory, the angle of internal friction governs the intersection angle between lines of fracture [*Marko and Thomson*, 1977; *Pritchard*, 1988; *Wang*, 2007; *Ringeisen et al.*, 2019]. That is, the lines of fracture are oriented at an angle $\theta(= \pi/2 - \phi/4)$ with the second principal stress direction, where the ratio of shear to normal stress is largest. In our simulations, the angles of fracture, although sensitive to the angle of internal friction, do not follow this theory. The fact that different angles of internal friction yield the same fracture orientation (e.g., for $\phi = 20°$ and $\phi = 30°$, see Fig. 3.12) indicates that the orientation is not directly associated to the yield criterion in the MEB rheology (there is no flow rule in the MEB rheology). However, the orientation of the lines of fracture do have a sensitivity to the angle of internal friction, which suggests that the deformations are at least indirectly influenced by the yield criterion. This is in accord with previous results showing that the fracture orientation is determined by the concentration of stress along lines damage instability [*Dansereau et al.*, 2019]. This raises the question whether the lines of fracture may be influenced by the stress correction path used in the damage parameterization, which determines the stress state associated to the fractures. These questions are left for future work and will be addressed using a simple uniaxial loading numerical experiments [e.g. *Ringeisen et al.*, 2019].

We speculate that in a longer simulation, ice would eventually jam between the upstream lines of fracture, resulting in the formation of a stable ice arch upstream of the channel. This is suggested by the orientation of the second principal stress component upstream of the channel (Fig. 3.10c). Longer term simulations, however, are prevented by the presence of numerical instabilities associated with the current damage parameterization. As the integration progresses, the simulated fields loose their longitudinal symmetry about the center line of the domain. This loss of symmetry occurs more rapidly as the residual norm increases (Fig. 3.14), and is not due to a difficulty in solving the equations: the non-linear solver converges rapidly, within 6 iterations, given the small time step required by the CFL criterion to resolve the elastic waves. The errors are rather related to the integration of the residual norms in the model memory terms in the constitutive equation. The integrated error is only dissipated over a large number of time-step, such that the error in the solution is orders of magnitude larger than the set residual norm tolerance. This limits the current analysis to short-term simulations in which this issue remains negligible.

An error propagation analysis shows that the instabilities are largely attributed to the stress correction scheme and the computation of the damage factor Ψ (Eq. 3.13). Assuming that the model is iterated to convergence such that the uncorrected stress state has a relative error ϵ, the error on the corrected stress is (see derivation in Appendix 3.6.3):

$$\epsilon_M = \epsilon\sqrt{1+R}, \tag{3.48}$$

where

$$R = \frac{\sigma_{II}'^2 + \mu^2\sigma_I'^2}{(\sigma_{II}' + \mu\sigma_I')^2}. \tag{3.49}$$

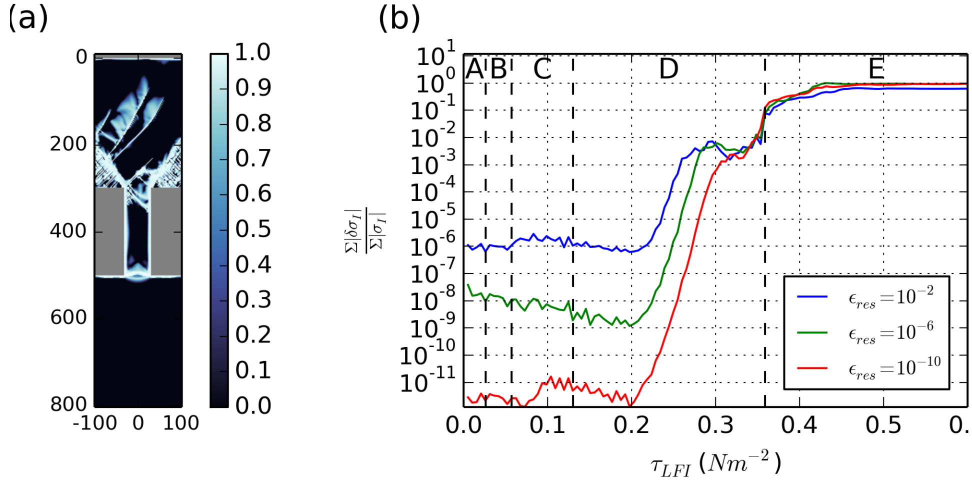

Figure 3.14: a) Asymmetries dominating the damage fields after the ice bridge collapse (Stage E) in Fig. 3.4). b) Evolution of normalized, domain-integrated asymmetries in the σ_I field when using different residual tolerance ϵ_{res} on the solution. Dashed lines indicate the beginning and end of the simulation phases (A,B,C,D,E).

If $\sigma_I' > 0$ (tensile stress state), $0 < R < 1$ (triangle inequality) and the error on the memory terms (ϵ_M) is of the same order as that of the uncorrected stress state ($\epsilon \leq \epsilon_M \leq \sqrt{2}\epsilon$). If $\sigma_I' < 0$ (compressive stress state), we have $R \geq 1$, and the error on the stress memory can become orders of magnitude larger than that of the uncorrected stress state, and the model accuracy and convergence properties are greatly reduced. These errors are stored in the memory terms, and accumulate at each fracture event. Note that as the elastic stress memory is dissipated over the viscous relaxation time scale, and this issue could be mitigated by decreasing the viscous coefficients η_0. Using a compressive strength cut-off capping also offers a limit to the uniaxial compression and reduces this instability. Another solution could be using a non-linear yield curve which converges to the Tresca criterion ($\sigma_{II} = \text{const}$) for large compressive stresses (e.g. the yield criterion of *Schreyer et al.* 2006). We however argue that this issue in the damage parameterization should be treated by bringing the stress back onto the yield curve along a different path (e.g. following a line perpendicular to the curve). It might also be possible to use a different stress correction path to constrain the orientation of the lines of fractures to the yield criterion. This will be assessed in future work.

3.5 conclusions

The MEB rheology is implemented in the Eulerian, FD numerical framework of the McGill sea ice model. We show that the discretized Maxwell stress-strain relationship can be written in a form that resembles that of the VP model, with an additional memory term. The MEB rheology is then simply implemented by redefining the VP viscous coefficients in terms of the MEB parameters and by adding the damage parameterization in a separate module. To our knowledge, it is the first time the MEB rheology is implemented in the same framework of a VP or EVP model. This will allow direct comparison of these models using the same numerical platform in future work.

In idealized ice bridge simulations, we show that the damage parameterization allows the ice fractures in the MEB model to propagate over large distances at short time scales. This process relies on the memory of the past deformations included in the model which causes a concentration of stresses close to the preexisting damage. We also show that while the choice of yield curve influences the localisation and orientation of the ice fractures, the angles of fracture propagation differ from those expected from the Mohr-Coulomb theory. This is consistent with results from [*Dansereau et al.*, 2019] showing that the fracture orientation is determined by the planes of damage instability. Preliminary results suggests that the orientation of the fracture lines are influenced by the stress correction scheme. This will be the subject of future work.

The stress correction scheme in the damage parameterization [*Rampal et al.*, 2016] is also found to cause a problematic increase in the numerical errors in the stress memory terms. The growth of errors depends on the magnitude of the compressive stress associated with the ice failure. These errors accumulate in the memory term at each fracture event, creating numerical artifacts that dominate the solutions over time. We argue that this weakness of the damage parameterization should be treated as a numerical issue. In previous MEB implementations, asymmetries are expected due to either the asymmetric coastlines and forcing [*Rampal et al.*, 2016] or to the material heterogeneity used to initialise the model [*Dansereau et al.*, 2016], such that this instability difficult to detect. A possible solution to this problem would be to use a non-linear yield curve which converges to the Tresca criterion for large compressive stresses (e.g. the yield criterion of *Schreyer et al.* 2006). It may also be possible to eliminate this numerical noise by using a different stress correction scheme that does not follow a path to the origin. This will be assessed in future work.

The simulated break up of the landfast ice bridge occurs with two main fracture events. First, an ice arch develops at the downstream end of the channel, shaping the edge of the ice bridge in the channel. This ice arch forms in all simulations and is stable in shape as long as the ice bridge remains in place, with a curvature that increases for smaller angles of internal friction. Second, shear fractures are formed at the upstream end of the channel, resulting in the decohesion of the channel ice bridge and in the formation of landfast wedges upstream of the islands. Based on the simulation results, we determined that the parameterized cohesion most consistent to the observed ice bridges in the Arctic are in the range of 5-10 kN m^{-2}, lower than stress buoys which measure both dynamical and thermal stresses at smaller scales but in the range of values previously associated to ice arch observations.

3.6 Appendix

3.6.1 Damage factor

Let σ'_I and σ'_{II} be the stress invariant at time level n before the correction is applied, and σ_{If} and σ_{IIf} the corrected stress invariant lying on the yield curve. Following *Bouillon and Rampal* [2015] we use a damage factor Ψ ($0 < \Psi < 1$) to reduce the elastic stiffness and bring the stress state onto the yield curve. I.e. :

$$\sigma_{If} = \Psi \sigma'_I \qquad ; \qquad \sigma_{IIf} = \Psi \sigma'_{II}. \tag{3.50}$$

Substituting these relations into the Morh Coulomb criterion ($\sigma_{IIf} + \mu\sigma_{If} = c$) we solve for Ψ:

$$\Psi = \frac{c}{\sigma'_{II} + \mu\sigma'_I}. \tag{3.51}$$

Note that this relation implies that the stress correction is done following a line from the stress state (σ'_I,σ'_{II}) to the origin (see Fig. 3.2). This scheme stems from applying the damage factor to each individual stress components. Other paths could be used for the correction (e.g. following a vertical or horizontal line), but would require the use of a different stress factor for the different components of the stress tensor. This could be used to cure the error propagation problem when large compressive stresses are present (see Appendix 3.6.3).

3.6.2 Analytical solutions of the 1D momentum equation

Considering an infinite channel of landfast ice ($\mathbf{u} = 0$) along the y-direction with forcing $\tau_{LFY} = \tau_y$, we write the 1D steady state momentum equation as:

$$\frac{\partial \sigma_{xy}}{\partial x} + \tau_y = 0, \tag{3.52}$$

where we have neglected the $\partial/\partial y$ terms. In this case, the normal stress is zero in the entire channel and the stress invariants are $\sigma_I = 0$, $\sigma_{II} = \sigma_{xy}$. The shear stress at any arbitrary point x across the channel can be determined by integrating Eq. 3.52 from the channel center ($x = 0$) to x :

$$\sigma_{xy} = -\tau_y x. \tag{3.53}$$

By symmetry, the maximum shear stresses in the channel are located at the channel walls, at $x = \pm\frac{W}{2}$ where W is the width of the channel. The maximum shear stress invariant on the channel walls is then:

$$\sigma_{II} = \frac{W\tau_y}{2}. \tag{3.54}$$

Similarly, we find the analytical solution for the normal stresses in a band of landfast ice with width L_y along an infinite coastline running in the x direction with a surface forcing $\tau_{LFI} = \tau_y$, by integrating the 1D momemtum equation in which the $\partial/\partial x$ terms are neglected. That is:

$$\frac{\partial \sigma_{yy}}{\partial y} + \tau_y = 0, \tag{3.55}$$

$$\sigma_{yy} = -\tau_y y. \tag{3.56}$$

Placing the landfast ice edge (where $\sigma_{yy} = 0$) at $y = 0$, the largest compressive stresses will be located along the coast, at $y = -L_y$. Note that in this case, shear stress is zero in the entire land-fast ice and the stress invariants are function of both σ_{xx} and σ_{yy}:

$$\sigma_{yy} = EC_1\epsilon_{yy}, \tag{3.57}$$

$$\sigma_{xx} = EC_2\epsilon_{yy} = \nu\sigma_{yy}, \tag{3.58}$$

$$\sigma_I = \frac{\sigma_{xx} + \sigma_{yy}}{2} = \frac{(1+\nu)\sigma_{yy}}{2}, \tag{3.59}$$

$$\sigma_{II} = \sqrt{(\frac{\sigma_{yy} - \sigma_{xx}}{2})^2} = \frac{(1-\nu)\sigma_{yy}}{2}. \tag{3.60}$$

This allows to write the Mohr-Coulomb criterion in terms of σ_{yy}:

$$\sigma_{II} + \sin\phi\sigma_I = \frac{1+2\sin\phi}{3}\sigma_{yy} < c, \tag{3.61}$$

3.6.3 Error propagation analysis

The error δF associated with a function $F(X,Y,Z,...)$ with uncertainties $(\delta x, \delta y, \delta z, ...)$ is given by:

$$\delta F = \sqrt{(\frac{\partial F}{\partial X})^2 \delta x^2 + (\frac{\partial F}{\partial Y})^2 \delta y^2 + (\frac{\partial F}{\partial Z})^2 \delta z^2 + ...} \tag{3.62}$$

In the damage parameterization, the components of the corrected stress tensor used as the memory terms (σ_{ijM}) can be written in terms of the uncorrected stress tensor (σ'_{ij}) and the damage factor Ψ (Eq. 3.13):

$$\sigma_{ijM} = \Psi \sigma'_{ij}. \tag{3.63}$$

Using Eq. 3.51, this can be rewritten in terms of the uncorrected stress invariants (σ'_I, σ'_{II}):

$$\sigma_{ijM}(\sigma'_{ij}, \sigma'_I, \sigma'_{II}) = \frac{c\, \sigma'_{ij}}{\sigma'_{II} + \mu \sigma'_I} \tag{3.64}$$

Assuming that the model has converged to a solution within an error on the stresses $\delta\sigma'_{ij} = \epsilon\sigma'_{ij}$, $\delta\sigma'_I = \epsilon\sigma'_I$, $\delta\sigma'_{II} = \epsilon\sigma'_{II}$, where ϵ is a small number, the model convergence error propagates on the stress memory with an error of :

$$\delta\sigma_{ijM} = \sqrt{(\frac{\partial \sigma_{ijM}}{\partial \sigma'_{ij}})^2 \delta\sigma'^2_{ij} + (\frac{\partial \sigma_{ijM}}{\partial \sigma'_I})^2 \delta\sigma'^2_I + (\frac{\partial \sigma_{ijM}}{\partial \sigma'_{II}})^2 \delta\sigma'^2_{II}}. \tag{3.65}$$

Substituting ($\delta\sigma'_{ij}$, $\delta\sigma'_I$, $\delta\sigma'_{II}$) for ϵ and using Eq. 3.64, we obtain:

$$\delta\sigma_{ijM} = \sqrt{\frac{c^2}{(\sigma'_{II} + \mu\sigma'_I)^2}\epsilon^2\sigma'^2_{ij} + \frac{c^2\sigma'^2_{ij}\mu^2}{(\sigma'_{II} + \mu\sigma'_I)^4}\epsilon^2\sigma'^2_I + \frac{c^2\sigma'^2_{ij}}{(\sigma'_{II} + \mu\sigma'_I)^4}\epsilon^2\sigma'^2_{II}}, \tag{3.66}$$

or:

$$\delta\sigma_{ijM} = \epsilon\sigma_{ijM}\sqrt{1 + \frac{\sigma'^2_{II} + \mu^2\sigma'^2_I}{(\sigma'_{II} + \mu\sigma'_I)^2}}. \tag{3.67}$$

Assuming that the error on the stress memory components (ϵ_M) has the form $\delta\sigma_{ijM} = \epsilon_M \sigma_{ijM}$, we can express the relative error of the stress memory components as a function of of the stress invariants as :

$$\epsilon_M = \epsilon\sqrt{1 + R} \tag{3.68}$$

where

$$R = \frac{\sigma_{II}'^2 + \mu^2 \sigma_I'^2}{(\sigma_{II}' + \mu\sigma_I')^2} \tag{3.69}$$

Chapter 4

A generalized stress correction scheme for the MEB rheology: impacts on sea-ice fracture angles and deformations

In this chapter, a generalized stress correction scheme is developed to reduce the growth of the residual error associated with the damage parameterization. The generalized stress correction scheme is also tested in the context of uni-axial loading experiments and used to bring the orientation of the simulated fractures closer to observations. This chapter was submitted to the journal The Cryosphere Discussions and is currently under review.

A generalized stress correction scheme for the MEB rheology: impacts on sea-ice fracture angles and deformations

Mathieu Plante[1] and Bruno Tremblay[1]

[1]Department of Atmospheric and Oceanic Sciences, McGill University, Montréal, Québec, Canada

The manuscript reproduced was submitted to the journal The Cryosphere Discussions and is currently under revision.

Abstract

A generalized damage parameterization is developed for the Maxwell Elasto-Brittle (MEB) rheology that reduces the growth of residual errors associated with the correction of super-critical stresses. In the generalized stress correction, a decohesive stress tensor is used to bring the super-critical stresses back on the yield curve based on any correction path. The sensitivity of the simulated material behaviour to the magnitude of the decohesive stress tensor is investigated in uniaxial compression simulations. Results show that while the decohesive stress tensor influences the short-term fracture deformation and orientation, the long-term post-fracture behaviour remains unchanged. Divergence first occurs when the elastic response is dominant followed by post-fracture shear and convergence when the viscous response dominates – contrary to laboratory experiment of granular flow and satellite imagery in the Arctic. The post-fracture deformations are shown to be dissociated from the fracture process itself, an important difference with classical Viscous Plastic (VP) models. Using the generalized damage parameterization together with a stress correction path normal to the yield curve brings the simulated fracture angles closer to observations (from $40-50°$ to $35-45°$, compared to $20-30°$ in observations) and reduces the growth of errors sufficiently for the production of longer-term simulations.

4.1 Introduction

Sea ice is a thin layer of solid material that insulates the polar oceans from the cold atmosphere. When sea ice fractures and a lead (or Linear Kinematic Features, LKFs) opens, large heat and moisture fluxes take place between the ocean and the atmosphere, significantly affecting the polar meteorology on short time-scales and the climate system on long time-scales [*Maykut*, 1982; *Ledley*, 1988; *Lüpkes et al.*, 2008; *Li et al.*, 2020]. The refreezing of leads significantly contributes to the sea ice mass balance [*Wilchinsky et al.*, 2015; *Itkin* *et al.*, 2018], and the associated brine rejection drives the thermohaline ocean circulation in the Arctic and vertical eddies in the ocean mixed layer [*Kozo*, 1983; *Matsumura and Hasumi*, 2008]. As such, the production of accurate seasonal-to-decadal projections using coupled models requires an accurate representation of sea ice leads. Furthermore, the presence and deformations along LKFs can influence the pressure on ships and increase the risk of besetting [*Mussells et al.*, 2017; *Lemieux et al.*, 2020]. The increased navigation through the Arctic passages [*Pizzolato et al.*, 2016; *Aksenov et al.*, 2017] thus calls for the development of high-resolution sea ice forecast products that capture the finer-scale lead structures [*Jung et al.*, 2016].

As sea ice models are moving to higher spatial resolutions, they become increasingly capable of resolving LKFs [*Hutter et al.*, 2019; *Bouchat and Tremblay*, 2020]. The simulation of the ice fractures yet represents a challenge. To this day, most sea ice models simulate the motion of sea ice using plastic rheologies or modifications thereof [*Hibler*, 1979; *Hunke*, 2001]. While several improvements were made on the numerics and efficiency of the methods used to solve the highly non-linear momentum equation [*Hunke*, 2001; *Lemieux et al.*, 2008, 2014; *Kimmritz et al.*, 2016; *Koldunov et al.*, 2019], the physics governing the ice fracture remains mostly the same. A number of rheologies have however been developed over the years in an attempt to simulate the observed sea-ice deformations [*Tremblay and Mysak*, 1997; *Wilchinsky and Feltham*, 2004; *Schreyer et al.*, 2006; *Sulsky and Peterson*, 2011; *Rampal et al.*, 2016; *Dansereau et al.*, 2016; *Damsgaard et al.*, 2018]. Among these new approaches, a damage parameterization derived for rock mechanics and seismology models [*Amitrano et al.*, 1999; *Amitrano and Helmstetter*, 2006] was adapted for the large scale modelling of sea ice [*Girard et al.*, 2011; *Bouillon and Rampal*, 2015]. This parameterization uses a damage parameter to represent the changes in material properties associated with fractures. While still based on the continuum assumption, it allows for fractures to propagate on short time-scales in the sea-ice cover. It is used in the Elasto-Brittle [EB *Bouillon and Rampal*, 2015; *Rampal et al.*, 2016] and Maxwell Elasto-Brittle [MEB *Dansereau et al.*, 2016] rheologies, implemented in the large scale sea-ice Finite Element model neXtSIM [*Rampal et al.*, 2019] and, recently, in the Finite Difference McGill sea ice model [*Plante et al.*, 2020].

The damage parameterization is relatively new, and it remains unclear to what extent differences in material behaviour are associated with the damage or to other rheological parameters. One known difference is the fracture development associated with local damage, stress concentration and damage propagation, rather than prescribed by an associative normal flow rule as in the standard VP models. The fracture angle simulated by the MEB and standard VP models are nonetheless in the same range [$\theta = 35 - 55°$, *Dansereau et al.*, 2019; *Hutter et al.*, 2020], which is larger than those derived from high-resolution satellite observations [$\theta = 20 - 45°$ *Hutter et al.*, 2019] and in-situ observations [$\theta = 20 - 30°$ *Marko and Thomson*, 1977; *Schulson*, 2004]. In the standard VP model, modifications of the mechanical strength parameters (compressive and shear) and the use of non-associated flow rules lead to smaller fracture angles that are more in line with observations [*Ringeisen et al.*, 2019, 2020]. In the MEB rheology, the fracture angles can be reduced by increasing the angle of internal friction or the Poisson ratio [*Dansereau et al.*, 2019]. These sensitivities suggest that modifications to the damage parameterization could be used to bring the simulated fracture angles closer to observations, but has not yet been tested.

The MEB rheology also presents some numerical challenges associated with the growth of residual errors associated with the damage parameterization at the grid scale [*Plante et al.*, 2020]. These errors can be attributed to the stress correction scheme, a numerical tool used to define the growth of damage and to bring the super-critical stresses back to the yield curve. Other progressive damage models instead represent the damage parameter as a discrete function of the number of failure cycles [*Main*, 2000; *Amitrano and Helmstetter*, 2006; *Carrier et al.*, 2015]. In continuum damage mechanics, a damage potential derived from thermodynamic laws [*Murakami*, 2012] is used to simulate the material fatigue. In the Elastic-Decohesive (ED) rheology, material damage is not parameterized but a decohesive strain rate explicitly represents the material discontinuity associated with the ice fracture and reduces the material strength of sea-ice [*Schreyer et al.*, 2006; *Sulsky and Peterson*, 2011].

In this paper, we present a generalization of the damage parameterization that reduces the growth of the residual errors associated with the stress correction and brings the simulated fracture angle of sea ice in simple uniaxial loading experiments closer to observations. Inspired by the work of *Schreyer et al.* [2006] and [*Sulsky and Peterson*, 2011], we introduce a decohesive stress associated with the fracture of sea ice and test its influence on the simulated sea-ice fracture and deformations in uniaxial loading experiments.

The paper is organised as follows. In section 4.2, we present the MEB rheology and governing equations. The generalized stress correction scheme is described in section 4.3. The uniaxial loading experimental set-up is presented in section 4.4 along with the definition of diagnostics used to quantify the growth of damage and the growth of residual errors. Results are presented in section 4.5, with a focus on the material behaviour in uniaxial compression experiments and its response to the changes in the damage parameterization. In section 4.6, we discuss the influence of the stress correction and seeded heterogeneity. Conclusions are summarized in section 4.7.

4.2 Model

4.2.1 Momentum and continuity equations

The simulations are run using the MEB model implemented on a Eulerian Arakawa C-grid in the McGill Sea Ice Model Version 5 [McGill SIM5, *Tremblay and Mysak*, 1997; *Lemieux et al.*, 2008; *Plante et al.*, 2020]. The vertically integrated 2D momentum equation for sea ice, forced with surface friction only (i.e. ignoring the sea surface tilt, the coriolis and the ice grounding terms), can be written as:

$$\rho_i h \frac{\partial \boldsymbol{u}}{\partial t} = \nabla \cdot \boldsymbol{\sigma} + \boldsymbol{\tau}, \tag{4.1}$$

where ρ_i is the ice density, h is the mean ice thickness, $\boldsymbol{u}$ $(= u\hat{\boldsymbol{\imath}} + v\hat{\boldsymbol{\jmath}})$ is the ice velocity vector, $\boldsymbol{\sigma}$ is the vertically integrated internal stress tensor and $\boldsymbol{\tau}$ is the net external surface stress from winds and ocean currents. This simplified formulation is appropriate for short term uniaxial loading experiments but can result in small errors in ice velocity when using a realistic model domain and forcing [*Turnbull et al.*, 2017]. Following [*Plante et al.*, 2020], we define the uniaxial loading by a surface wind stress $\boldsymbol{\tau}_a$ and prescribe an ocean at rest below the ice:

$$\boldsymbol{\tau} \approx \boldsymbol{\tau}_a - \rho_w C_{dw} |\boldsymbol{u}| \boldsymbol{u}, \tag{4.2}$$

where ρ_w is the water density, C_{dw} is the water drag coefficient and $\boldsymbol{u}$ is the sea ice velocity (see values in Table 4.1).

The prognostic equations for the mean ice thickness h (volume per grid cell area) and concentration A are written as:

$$\frac{\partial h}{\partial t} + \nabla \cdot (h\boldsymbol{u}) = 0, \tag{4.3}$$

$$\frac{\partial A}{\partial t} + \nabla \cdot (A\boldsymbol{u}) = 0, \tag{4.4}$$

where the thermodynamic source an sink terms are ignored.

Table 4.1: Default Model Parameters

Parameter	Definition	Value
Δx	Spatial resolution	1 km
Δt	Time step	0.2 s
T_d	Damage time scale	1 s
Y	Young Modulus	10^9 n m^{-2}
ν	Poisson ratio	0.33
λ_0	Viscous relaxation time	10^5 s
ϕ	Angle of internal friction	45°
c_0	Cohesion	10 N m^{-2}
σ_{c_0}	Isotropic compressive strength	50N m^{-2}
ρ_a	Air density	1.3 kg m^{-3}
ρ_i	Sea ice density	9.0×10^2 kg m^{-3}
ρ_w	Sea water density	1.026×10^3 kg m^{-3}
C_{da}	Air drag coefficient	1.2×10^{-3}
C_{dw}	Water drag coefficient	5.5×10^{-3}

4.2.2 Maxwell Elasto Brittle Rheology

In the MEB rheology, the ice behaves as a visco-elastic material with a fast elastic response and a viscous response over a longer-time scale. The governing equation for this visco-elastic material can be written as [*Dansereau et al.*, 2016, 2017; *Plante et al.*, 2020]:

$$\frac{\partial \boldsymbol{\sigma}}{\partial t} + \frac{1}{\lambda}\boldsymbol{\sigma} = E\mathbf{C} : \dot{\boldsymbol{\epsilon}}, \tag{4.5}$$

where E is the elastic stiffness defined as the vertically integrated Young Modulus of sea ice, λ is the viscous relaxation time-scale, ":" denotes the inner double tensor product and $\dot{\boldsymbol{\epsilon}}$ is the strain rate tensor. The elastic tensor $\mathbf{C}$ and strain rate tensor $\dot{\boldsymbol{\epsilon}}$ are given by:

$$\mathbf{C} = \frac{1}{1-\nu^2}\begin{pmatrix} 1 & \nu & 0 \\ \nu & 1 & 0 \\ 0 & 0 & 1-\nu \end{pmatrix}, \tag{4.6}$$

$$\begin{pmatrix} \dot{\epsilon}_{11} \\ \dot{\epsilon}_{22} \\ \dot{\epsilon}_{12} \end{pmatrix} = \begin{pmatrix} \frac{\partial u}{\partial x} \\ \frac{\partial v}{\partial y} \\ \frac{1}{2}\left(\frac{\partial u}{\partial y} + \frac{\partial v}{\partial x}\right) \end{pmatrix} \tag{4.7}$$

where ν $(= 0.33)$ is the Poisson ratio, which defines the relative amount of deformation on the plane parallel to the loading.

The relative importance of the elastic and viscous components (first and second terms on the left hand side in Eq. 4.5) are determined by the magnitude of the elastic modulus E and viscous relaxation time-scale λ. E and λ are functions of the ice thickness, concentration and damage resulting in dominant elastic component for small deformations (undamaged ice) and dominant viscous component for large deformations (heavily fractured ice). The elastic modulus E and viscous relaxation time-scale λ are written as:

$$E = Yhe^{-a(1-A)}(1-d), \tag{4.8}$$

$$\lambda = \lambda_0(1-d)^{\alpha-1}, \tag{4.9}$$

where Y (= 1 GPa) is the Young Modulus of undeformed sea ice, d is the damage parameter ($0 < d < 1$), a (= 20) is the standard parameter ruling the dependency of the material strength properties on sea-ice concentration [*Hibler*, 1979; *Rampal et al.*, 2016] and λ_0 (= 10^5s, ≈1 day) is the viscous relaxation time scale for undamaged sea ice.

4.2.3 Yield criterion

Damage (or fracture) occurs when the internal stress state exceeds the Mohr-Coulomb failure criterion,

$$F(\sigma) = \sigma_{II} + \mu\sigma_I - c < 0, \tag{4.10}$$

where σ_I is the isotropic normal stress invariant (compression defined as negative), σ_{II} is the maximum shear stress invariant, μ (= $\sin\phi$) is the coefficient of internal friction of ice, ϕ (= 45°) is the angle of internal friction, and c is the vertically integrated cohesion, defined as:

$$c = c_0 he^{-a(1-A)}, \tag{4.11}$$

where c_0 (= 10 kN m^{-2}) is the cohesion of sea ice derived from observations [*Sodhi*, 1997; *Tremblay and Hakakian*, 2006; *Plante et al.*, 2020] or laboratory experiments [*Timco and Weeks*, 2010]. No compressive or tensile strength cut-off are used in this analysis. The reader is referred to Table 4.1 for a list of default model parameters.

4.2.4 Damage parameterization

The prognostic equation for the damage parameter d in the standard MEB rheology is parameterized using a relaxation term with time scale T_d ($= 1$ s) as:

$$\frac{\partial d}{\partial t} = \frac{(1-\Psi)(1-d)}{T_d}, \tag{4.12}$$

where

$$\Psi = \frac{\boldsymbol{\sigma}_c}{\boldsymbol{\sigma}'} = \min\big(1, \frac{c}{\sigma'_{II} + \mu\sigma'_I}\big) \tag{4.13}$$

is a damage factor ($0 < \Psi < 1$), $\boldsymbol{\sigma}_c$ is the critical stress lying on the yield curve and $\boldsymbol{\sigma}'$ is the uncorrected stress state lying outside of the yield curve. Thermodynamic healing and advection are neglected as we are focusing on the ice fracture.

When the ice fractures, the damage factor Ψ is used to scale the super-critical stresses back towards the yield curve. The prognostic equation for the temporal evolution of the super-critical stress tensor $\boldsymbol{\sigma}'$ is written as a relaxation equation of the same form as in Eq. 4.12:

$$\frac{\partial \boldsymbol{\sigma}'}{\partial t} = -\frac{(1-\Psi)\boldsymbol{\sigma}'}{T_d}. \tag{4.14}$$

4.3 Generalized stress correction

We propose a generalized damage parameterization where the super-critical stresses are corrected back to the yield curve along a line oriented at any angle γ from the y-axis in the stress invariant space (see Fig. 4.1). To this end, we chose to define the damage factor in terms of the shear stress invariant only, as:

$$\Psi = \frac{\sigma_{IIc}}{\sigma'_{II}}, \tag{4.15}$$

where the critical shear stress invariant σ_{IIc} is defined by the intersection point between the correction path and the yield curve (see Fig 4.1). After some algebra, we obtain:

$$\sigma_{IIc} = \frac{c + \mu \tan(\gamma)\sigma'_{II} - \mu\sigma'_{I}}{1 + \mu \tan(\gamma)}. \tag{4.16}$$

The damage factor can then be written in terms of the super-critical stress state invariants (σ'_I,σ'_{II}), the correction path angle γ and the coefficient of internal friction μ, as:

$$\Psi = \frac{c + \mu \tan(\gamma)\sigma'_{II} - \mu\sigma'_{I}}{(1 + \mu \tan(\gamma))\sigma'_{II}}. \tag{4.17}$$

In this manner, the correction of super-critical stresses can follow any line in the stress invariant space provided that the damage increases when ice fractures ($\Psi < 1$, or $\gamma < 90°$). The generalized formulation now allows for the use of a yield curve without cohesion ($c = 0$ kN m^{-1}), something that is not possible in the standard parameterization otherwise Ψ is identically equal to 0 (see Eq. 4.13).

Note that using a stress correction path other than the standard path to the origin means that the corrected normal stress differs from the scaled super-critical stress $\Psi\sigma'_I$. We define this difference as the decohesive stress tensor needed to for the corrected stress to follow the stress correction path γ (see Fig. 4.1). The stress correction equation (Eq. 4.14) then becomes:

$$\frac{\partial \boldsymbol{\sigma}'}{\partial t} = -\frac{(1-\Psi)\boldsymbol{\sigma}' + \boldsymbol{\sigma}_D}{T_d}. \tag{4.18}$$

The invariants of the decohesive stress tensor (σ_{ID},σ_{IID}) are therefore written as:

$$\sigma_{ID} = \sigma_{Ic} - \Psi\sigma'_I = \frac{c - \Psi(\sigma'_{II} - \mu\sigma'_I)}{\mu}, \tag{4.19}$$

$$\sigma_{IID} = 0, \text{ (by definition)}. \tag{4.20}$$

When $\tan\gamma = \sigma'_I/\sigma'_{II}$ and $\sigma_{ID} = \sigma_{IID} = 0$, we obtain the standard damage parameterization of *Dansereau et al.* [2016] as a special case where the stress correction path depends on the super-critical stress state. Note that the decohesive stress tensor used in this parameterization has a similar role as the decohesive strain rates used in the Elastic-Decohesive model *Schreyer et al.* [2006], in that they both determine the change in stress state associated with the development of a fracture. In the present scheme, $\boldsymbol{\sigma}_D$ is derived from the stress correction path, while the decohesive strain rate in *Schreyer et al.* [2006] is derived from the opening of a lead based on granular theory.

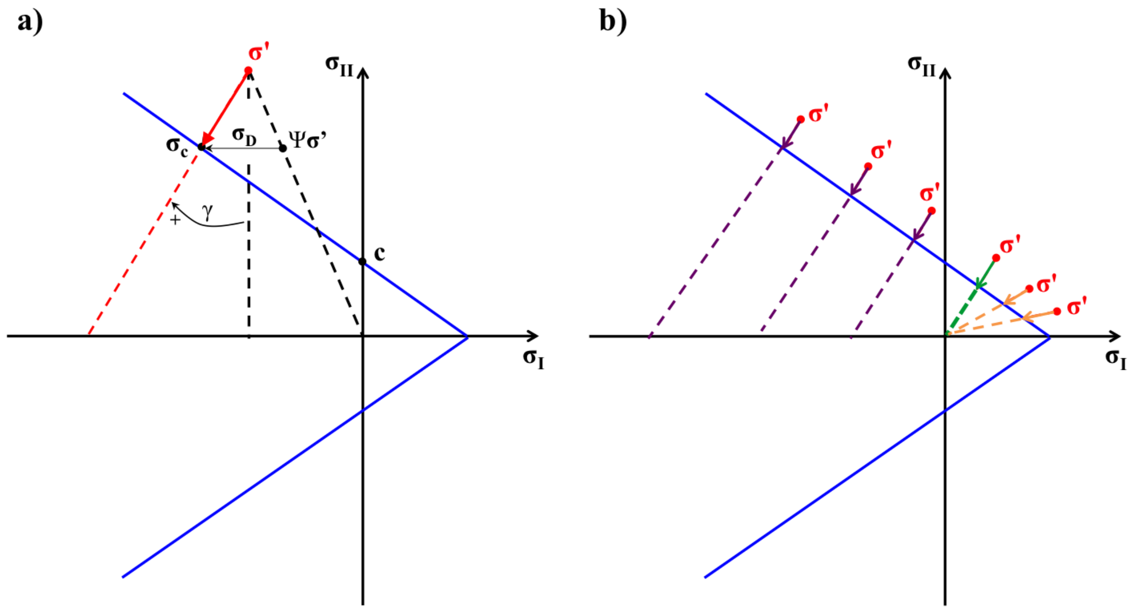

Figure 4.1: a) Mohr-Coulomb yield criterion in stress invariant space. $\boldsymbol{\sigma}'$ is the uncorrected super-critical stress state, $\boldsymbol{\sigma}_c$ the critical stress state for a given correction path angle γ (red dashed line) and c is the cohesion. The decohesive stress tensor $\boldsymbol{\sigma}_D$ is defined as the difference between $\boldsymbol{\sigma}_c$ and the scaled super-critical stress ($\Psi\boldsymbol{\sigma}'$). b) Proposed correction paths for various super-critical stresses $\boldsymbol{\sigma}'$ that minimizes the error amplification ratio (R), which consist of the standard parameterization for large tensile stresses (orange) and a correction path with γ = 45° for small tensile and compressive stresses (purple). The green line indicates the transition between the two formulations.

4.3.1 Projected error

The error $\delta\Psi$ on the damage factor $\Psi(\sigma'_I, \sigma'_{II})$ can be written as:

$$\delta\Psi = \sqrt{\left(\frac{\partial\Psi}{\partial\sigma'_I}\right)^2 \delta\sigma'^2_I + \left(\frac{\partial\Psi}{\partial\sigma'_{II}}\right)^2 \delta\sigma'^2_{II}}, \tag{4.21}$$

where ($\delta\sigma'_I$,$\delta\sigma'_{II}$) are the errors on the calculated stress invariants. Expanding the derivative terms (using Eq. 4.18) and re-writing $\delta\sigma'_I$ and $\delta\sigma'_{II}$ in terms of the relative error ϵ (i.e., $\delta\sigma'_I = \epsilon\sigma'_I$, $\delta\sigma'_{II} = \epsilon\sigma'_{II}$), we obtain:

$$\delta\Psi = \sqrt{\frac{\mu^2}{(1+\mu\tan(\gamma))^2\sigma'^2_{II}}\epsilon^2\sigma'^2_I + \frac{(c-\mu\sigma'_I)^2}{(1+\mu\tan(\gamma))^2\sigma'^4_{II}}\epsilon^2\sigma'^2_{II}}, \tag{4.22}$$

$$= \Psi\epsilon\sqrt{\frac{\mu^2\sigma'^2_I + (c-\mu\sigma'_I)^2}{(c+\mu\tan(\gamma)\sigma'_{II} - \mu\sigma'_I)^2}}, \qquad = \Psi\epsilon R \tag{4.23}$$

where R is the error amplification ratio.

Assuming that the uncorrected stress is close to the yield criterion (i.e. $\sigma'_{II}+\mu\sigma'_I-c \sim 0$), this relation indicates that the error amplification ratio R goes to infinity if:

$$\tan(\gamma) = -1/\mu, \tag{4.24}$$

which corresponds to a path that runs parallel to the yield curve. This result is consistent with the instabilities in the standard stress correction scheme during ridging reported in *Plante et al.* [2020], given that a line passing through the origin is nearly parallel to the Mohr Coulomb yield curve for large compressive stresses. In contrast, the path that maximizes the denominator (smallest error growth) has $\gamma = 90°$. This path, however, correspond to $\Psi = 1$ and does not create damage. The possible stress correction path angles γ thus lie in the range $\arctan(-1/\mu) < \theta < 90°$.

Note that the error amplification ratio R is small for $\sigma_I < 0$, but becomes infinitely large at the yield curve tip when σ'_{II} approaches 0 (see Eq. 4.22). This behaviour is opposite to that of the standard stress correction scheme, which has small R values in tension and large values in compression [*Plante et al.*, 2020]. To minimize the errors for all stress states, we blend the two schemes (i.e. Eq. 4.17 in compression and Eq. 4.13 in tension, see Fig. 4.1b). We set the transition between the two schemes at the points where they are both equal (i.e., at $\sigma'_I/\sigma'_{II} = \tan\gamma$, see green line in Fig 4.1b). The damage factor is then defined as:

$$\Psi = \begin{cases} \frac{c+\mu\gamma\sigma'_{II}-\mu\sigma'_I}{(1+\mu\gamma)\sigma'_{II}}, & \text{if } \sigma'_I < \sigma'_{II}\tan\gamma, \\ \frac{c}{\sigma'_{II}+\mu\sigma'_I}, & \text{otherwise.} \end{cases} \tag{4.25}$$

4.4 Methods

4.4.1 Numerical approaches

The MEB model is implemented in the McGill Sea Ice Model Version 5 (McGill SIM5) using an Eulerian, 2nd order finite difference numerical scheme [*Tremblay and Mysak*, 1997; *Lemieux et al.*, 2014; *Plante et al.*, 2020]. The equations are discretized in space using an Arakawa C-grid and in time using a semi-implicit backward Euler scheme [*Plante et al.*, 2020]. A solution to the non-linear momentum and constitutive equations (Eqs. 4.1 and 4.5) is found using a Picard solver. The Picard solver uses an Outer Loop (OL) in which the equations are linearized and solved at each iteration using a preconditioned Flexible General Minimum RESidual method [FGMRES, *Lemieux et al.*, 2008]. The non-linear terms are then updated and the linear problem solved again until the residual error ϵ_{res}, defined as the L2-norm of the solution vector, is lower than 10^{-8} N/m^2. This strict tolerance on the residual error ϵ_{res} (orders of magnitude smaller than typical in VP model, where ϵ_{res} is rarely smaller than 10^3 N/m^2) is possible given the rapid convergence of the solution to the linear MEB constitutive equation, usually within ∼20-30 OL iterations. In comparison, simulations using the VP model usually need several hundreds of OL to reach a residual error $\epsilon_{res} < 10^{-2}$ N/m^2. The prognostic equations for the tracers (Eq. 4.3, 4.4 and 4.12) are updated within the OL iteration using an IMplicit-EXplicit (IMEX) approach [*Lemieux et al.*, 2014]. The reader is referred to *Plante et al.* [2020] for more details.

4.4.2 Experiment setup

Following *Ringeisen et al.* [2019]; *Dansereau et al.* [2019]; *Herman* [2016], we present results from idealized uniaxial loading experiments and test the sensitivity of the residual error growth on the correction path angle γ in the generalized stress correction scheme. The model domain is 250 x 100 km (with 1km resolution), with sea ice of 1m thickness and 100% concentration in the middle 60 km of the domain and two narrow bands of open water (20 km width) on each sides (Fig. 4.2). A solid Dirichlet boundary condition ($u = v = 0$) is used at the bottom, and open Neumann boundary conditions ($\partial u/\partial n = 0$) are used on the top and sides. In all experiments, the forcing is specified by a surface stress τ_a (see Eq. 4.2). This differs from *Ringeisen et al.* [2019] and *Dansereau et al.* [2016] where the upper boundary is represented by a moving wall acting as external forcing. The forcing τ_a is ramped up from 0 to 0.60 N/m^2 (corresponding to ∼20 m/s winds or ∼0.33 m/s surface currents) in a 2h period, and then remains constant.

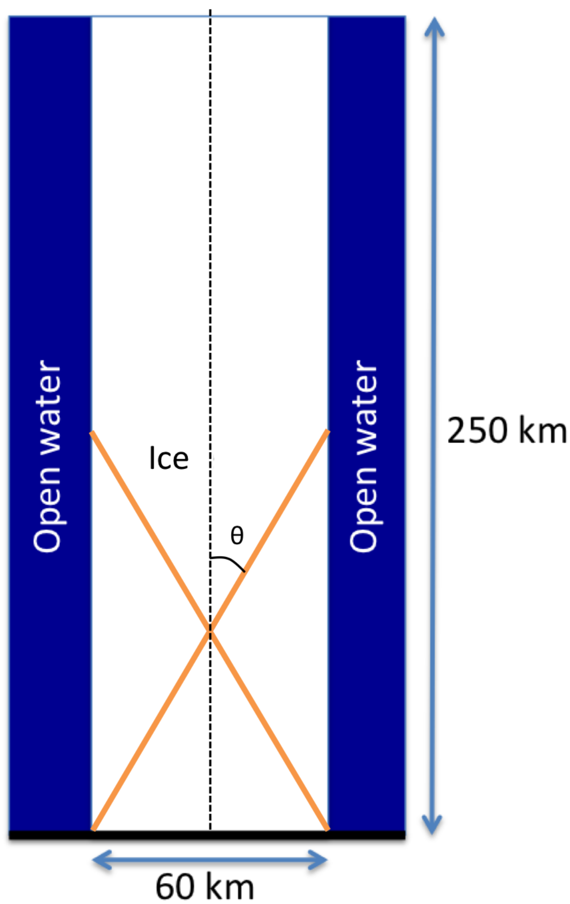

Figure 4.2: Idealized domain for uniaxial compression simulations, with a solid boundary (Dirichlet conditions, $u = v = 0$) at the bottom, and open boundaries (Neumann conditions, $\partial u/\partial n = 0$) on the sides and top. The initial conditions are h = 1m and A = 100% in a region of 250 x 60 km in the center of the domain (white), with two 20 km wide bands of open water on each side (blue). The fracture angle (θ) is defined as half of the angle between conjugate pairs of fracture lines (Orange lines).

4.4.3 Diagnostics definitions

4.4.3.1 Field asymmetry

We monitor the growth of the residual error in the simulations using a normalised domain-integrated asymmetry factor (ϵ_{asym}) in the maximum shear stress invariant field (σ_{II}), defined as:

$$\epsilon_{asym} = \frac{\sum_{i=a}^{b} \sum_{j=1}^{ny} |\sigma_{II}(i,j) - \sigma_{II}(nx-i,j)|}{\sum_{i=a}^{b} \sum_{j=1}^{ny} |\sigma_{II}(i,j)|}, \tag{4.26}$$

where (i,j) are the x-y grid indices respectively, (nx,ny) are the number of grid cells in the x and y-directions and (a,b) are the indices of the first and last ice-covered grid cells on the x-axis.

4.4.3.2 Damage activity

We define the damage activity D as the total damage integrated over the original ice domain in a 1 minute interval:

$$D = \sum_{i=a}^{b} \sum_{j=1}^{ny} \frac{d(i,j)^{t+30s} - d(i,j)^{t-30s}}{60s}. \tag{4.27}$$

This parameter is analog to the damage rate in [*Dansereau et al.*, 2016, 2017]. Note that this definition of damage activity (or damage rate) emphasizes activity in undamaged ice and is not sensitive to activity in already heavily damaged ice.

4.4.3.3 Fracture angle

When loaded in uniaxial compression, a granular material fails in diamond-shaped shear fractures [e.g. see *Marko and Thomson*, 1977; *Ringeisen et al.*, 2019]. We define the fracture angle θ as the angle between the y-axis and the fracture lines (see Fig. 4.2). The orientation of these fracture lines have been measured in laboratory using in uniaxial loading experiments. Several theories were developed to relate the fracture angle in terms of material parameters. The most common is the Mohr-Coulomb theory [*Coulomb*, 1773; *Mohr*, 1900], where the fracture angle is related to the angle of internal friction as:

$$\theta = \frac{\pi}{4} - \frac{\phi}{2}. \tag{4.28}$$

This theory tends to underestimate the fracture angle of granular materials in laboratory experiments [*Bardet*, 1991]. In the *Roscoe* [1970] theory, the fracture angle is defined instead in terms of the angle of dilatancy (δ) of the granular material:

$$\theta = \frac{\pi}{4} - \frac{\delta}{2}. \tag{4.29}$$

If $\delta = \phi$, the two theories give the same fracture angle θ. In general, the fracture angle falls between values predicted by the Mohr-Coulomb and Roscoe theories with zero dilatancy ($\delta = 0$) [*Arthur et al.*, 1977; *Bardet*, 1991].

In our experiment, the fracture angle is calculated graphically for each individual simulation. We define the uncertainty as $\pm\tan(W/L) \sim \pm 2^\circ$, where W is the fracture width (typically a few grid cells wide in our results, or $\sim$ 2-5 km) and L is the fracture length ($\sim$ 45 km). This error increases to $\pm 6^\circ$ for the few cases where the fracture is not well defined.

4.5 Results

4.5.1 Control simulation: standard damage parameterization

In the control simulation, a pair of conjugate fracture lines first appear when the surface forcing $\tau_a = 0.29$ N/m, along with secondary fracture lines that are the results of interactions between the ice floe and the solid boundary that extends across the full width of the domain at the base (Fig. 4.3). All fracture lines are oriented at 39° from the y-axis, smaller than reported by *Dansereau et al.* [2019] using a Finite Element implementation of the same model ($\theta =\sim 43°$) and in the high range seen in observations [θ = ∼20-40° *Marko and Thomson*, 1977; *Hibler III and Schulson*, 2000; *Schulson*, 2004; *Hutter et al.*, 2020]. This orientation also falls in between that predicted by the Mohr-Coulomb ($\theta = 22.5°$) and Roscoe theories ($\theta = 45°$ when $\delta = 0$), in accord with the common observation that both the angle of internal friction and the dilatancy (δ) are important in defining the fracture [*Arthur et al.*, 1977; *Vardoulakis*, 1980; *Balendran and Nemat-Nasser*, 1993].

When the ice fractures, the initial response is mostly elastic with divergence along the fracture line. The resulting stress concentration influences the propagation of the fracture in space over short time-scales (seconds) governed by the elastic waves speed. The sea-ice deformation continues to occur post-fracture in the damaged ice and, over time, the response transitions from elastic to viscous-dominated as the Maxwell viscosity dissipates the elastic stresses and creates permanent viscous deformations. This transition is clearly seen in the development of a linear dependence between stress and strain-rate invariants scaled by $(1 - d)^3$, where the slope corresponds to the viscosity (see for instance 4.4 c,f,i). The simulation reaches steady state with deformations that are fully viscous and localized in the heaviest damage areas (Fig. 4.4g-i). This causes a predominance of shear and convergence deformation along the fracture line throughout the simulation.

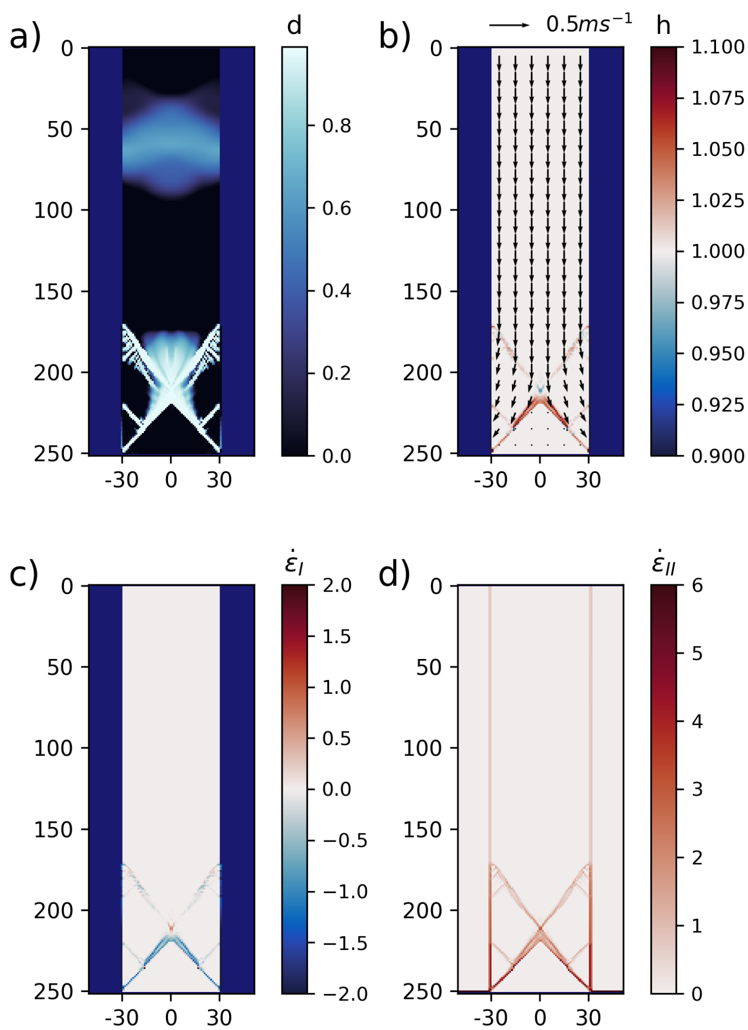

Figure 4.3: a) Damage (unitless), b) ice thickness (m, color) and velocity vectors (m s^{-1}), c) mean normal strain rate invariant ($\dot{\epsilon}_I$, day^{-1}) and d) miximum shear strain rate invariant ($\dot{\epsilon}_{II}$, days^{-1}), after two hours of integration in the control simulation using the standard stress correction scheme.

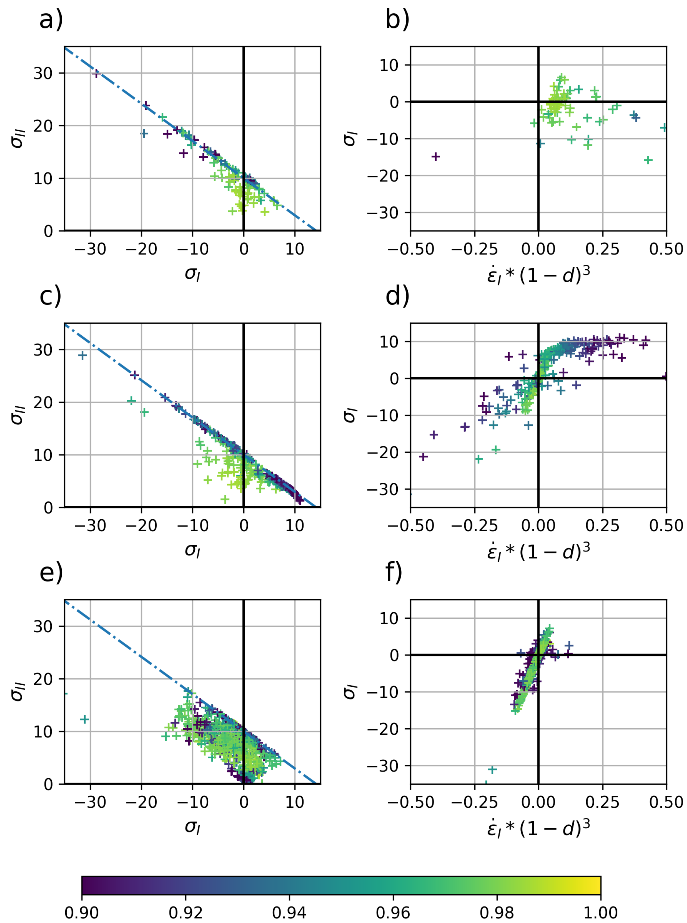

Figure 4.4: Stress invariants (kN m^{-1}, left column) and normal strain rate invariant scaled by the $(1-d)^3$ (day^{-1}x10^3) as a function of the normal stress invariant (kN m^{-1}, right column), in the control simulation for t = 60 min (top row), t = 120 min (middle row) and t = 180 min (bottom row).

The asymmetries in the solution are very small at the beginning of the simulation (t $\leq 57min$), and do not grow until fractures occur (Fig. 4.5a-b). As the fractures develop, small errors grow rapidly with ϵ_{asym} increasing in large steps crossing multiple orders of magnitude. Note that the model is always iterated to convergence with a strict residual error tolerance ($\epsilon_{res} = 10^{-6}Nm^{-2}$). The growth in ϵ_{asym} are associated with large values of damage error amplification ratio R (reaching ∼20, Fig. 4.5b). Since ϵ_{asym} is a domain-integrated quantity, it increases in time following large local error growths R. This illustrates the long-range and long-term influence of residual errors, which act on the development of the future fractures. Note that ϵ_{asym} saturates when the σ_{II} field is no longer symmetric, and becomes insensitive to additional error growth. We assess the precision of the solution using the maximum error amplification ratio R_{max}, which indicate the level of amplification of residual errors in the simulations, at times by more than one order of magnitude locally ($R_{max} > 10$).

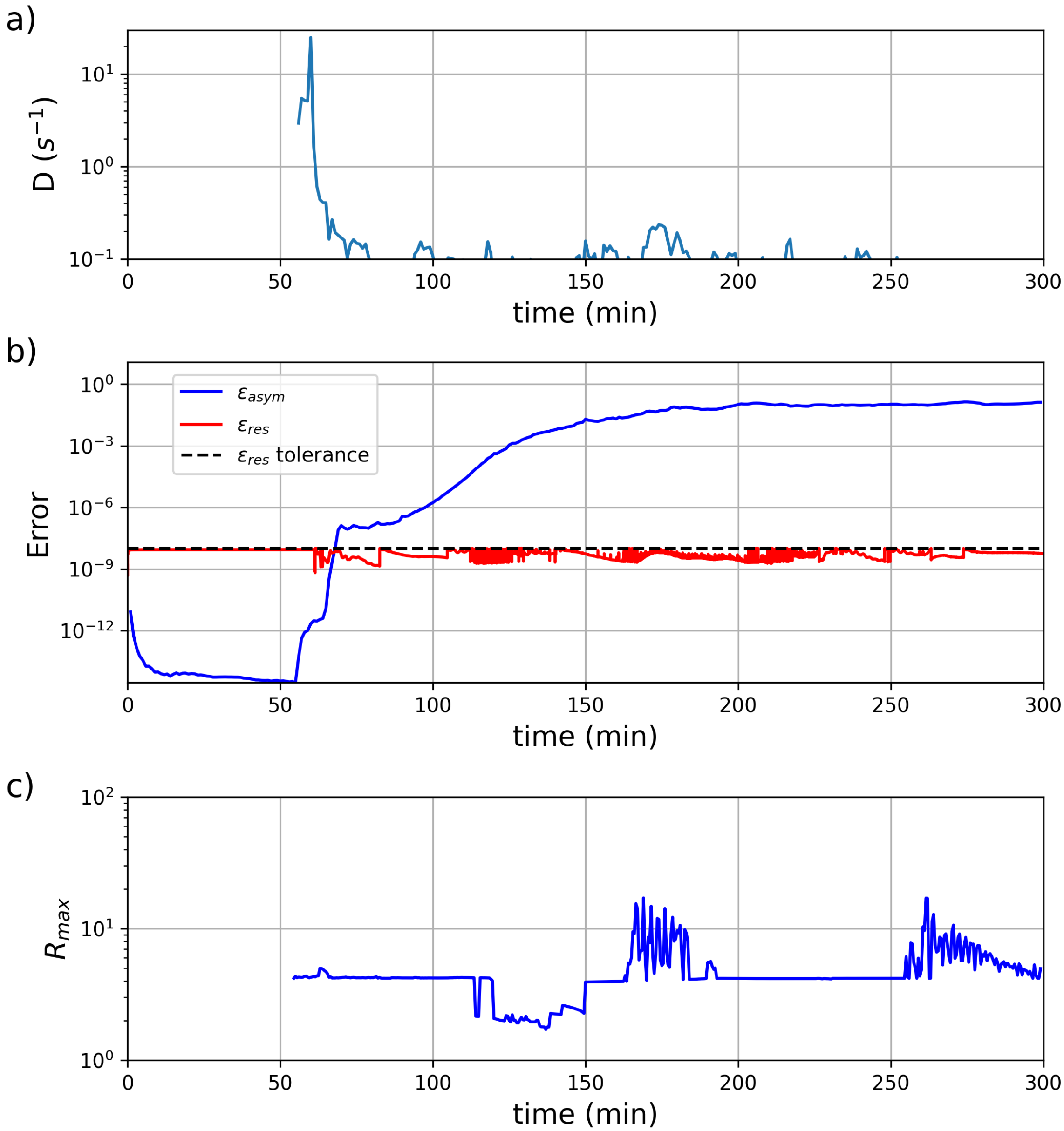

Figure 4.5: a) Temporal evolution of the damage activity D, b) the solution residual ϵ_{res}, asymmetry factor ϵ_{asym} and convergence criterion on ϵ_{res}, and c) the maximum error amplification ratio R_{max}, in the control simulation using the standard stress correction scheme.

4.5.2 Generalized stress correction

The generalized damage parameterization reduces the growth of residual errors, with decreasing error amplification ratio R_{max} for increasing path angle γ (Fig. 4.6a). This results in an overall reduction of the asymmetry factor ϵ_{asym} (Fig. 4.6b), allowing for the production of longer-term simulations that include post-fracture deformations. This improvement is only significant when using $\gamma > 0$. For $\gamma < 0$, the maximum error amplification ratio R_{max} remains important with periods when the residual error increases by up to two orders of magnitude locally.

Results show that the fracture angle is sensitive to the decohesive stress tensor, with decreasing fracture angle θ for increasing stress correction path angle γ (Fig. 4.7). This finding is in line with results from *Dansereau et al.* [2019], where the fracture angle was related to the far-field stress associated with the collective damage. In the MEB model, the far-field stresses directly depends on corrected stress state, including $\boldsymbol{\sigma}_D$ in the generalized damage parameterization. Increasing the correction path angle γ reduces the fracture angles in better agreement to observations.

Along the fracture lines, the correction path angle γ influences the time-integration required to reach the same damage and deformation rates (Fig. **??**). This due to the fact that increasing the angle γ reduces the amount of damage for the same super-critical stress state because the stress correction path approaches the horizontal and Ψ is closer to 1. The simulated ice deformations are otherwise mostly insensitive to the correction path angle; i.e. all simulations have divergence during the initial elastic response when the ice fractures followed by a transition to viscous deformations where shear and convergence deformations are predominant (Fig. **??**a). In contrast with results from the VP model and from typical granular material behaviour, divergent post-fracture deformation is only present when tensile stresses develop, e.g. at the intersection between conjugate lines of fracture.

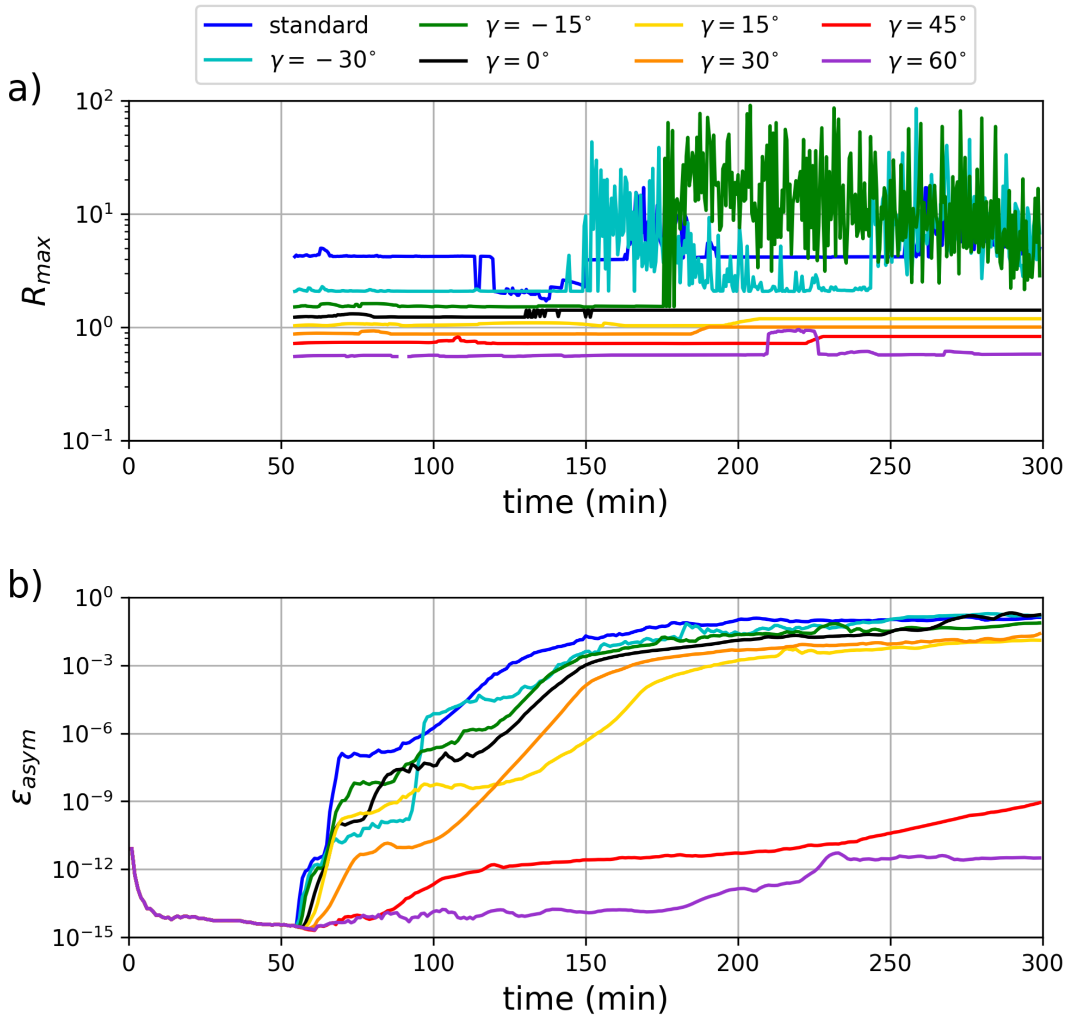

Figure 4.6: a) Temporal evolution of the maximum error amplification ratio R_{max} and b) the asymmetry factor ϵ_{asym}, in a sensitivity experiment on the stress correction path angle γ, using the generalized stress correction scheme.

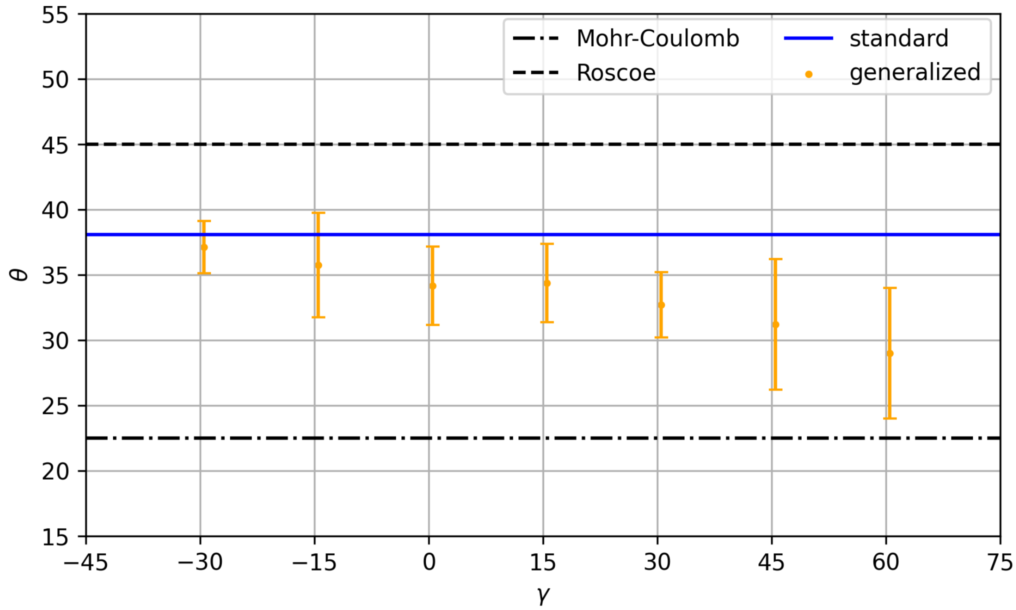

Figure 4.7: Sensitivity of the fracture angle θ on the stress correction path angle γ (degrees) in uniaxial loading experiments using the generalized stress correction schemes.

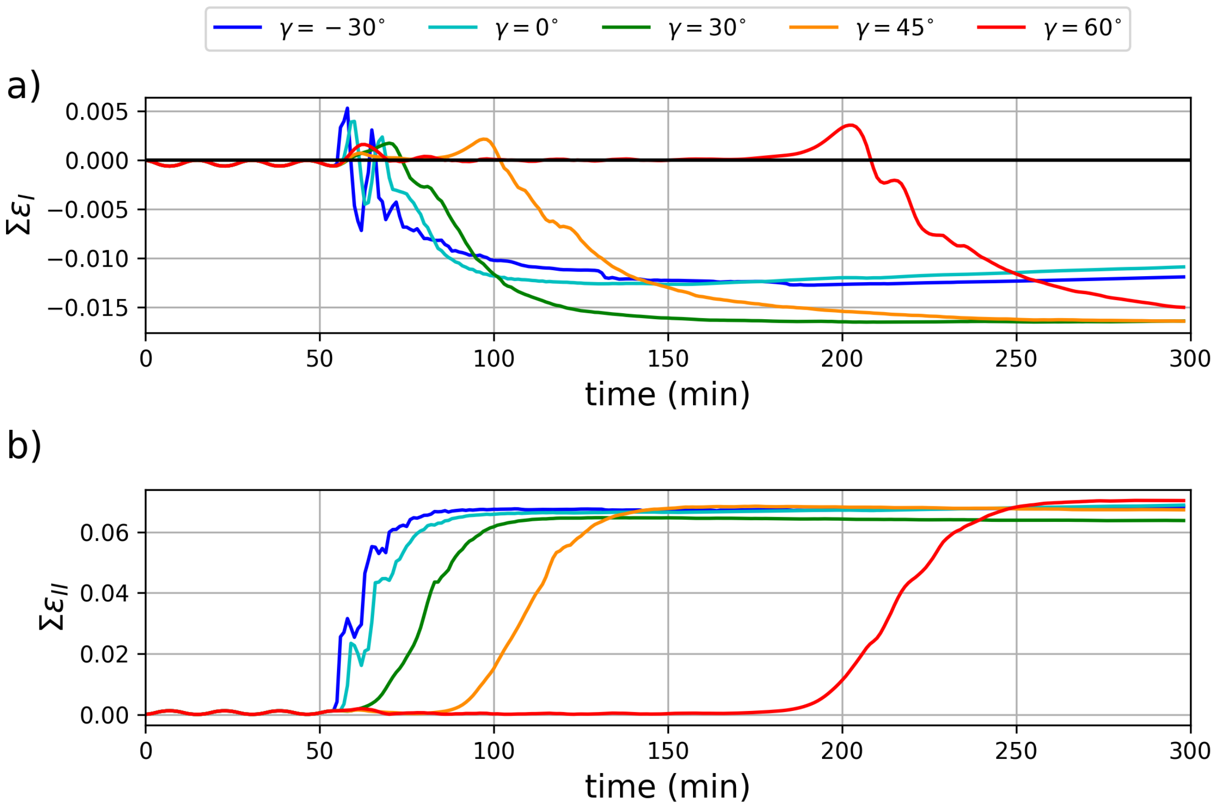

Figure 4.8: Time evolution of the mean normal (a) and maximum shear (b) strain rate invariants integrated over the ice cover, in simulations using the generalized damage parameterization with different stress correction path γ.

4.5.3 Angle of internal friction and Poisson ratio

Repeating the experiment using different angles of internal friction (ϕ) shows that the fracture angle decreases with increasing ϕ. The simulated fracture angles fall within the envelope from the Mohr-Coulomb and Roscoe theories, except for small angles of internal friction ($\phi < 20°$), a value that is rarely observed for granular materials (Fig. 4.9). Note that the sensitivity of the fracture angle to the coefficient of internal friction also disappears for small angles of internal friction ($\phi < 20°$) when using a large correction path angle ($\gamma = 60°$ in Fig. 4.7). When both the stress correction path and the yield criterion approaches the horizontal, fracture yields large stress corrections but small damage increases (i.e., $\Psi = 1$), such that the angle of fracture is governed by the stress correction and is weakly sensitive other model parameters. Based on these results, we suggest the use of a correction path that is normal to the yield criterion ($\gamma = \arctan \mu$, see black points in Fig. 4.9).

Decreasing the angle of internal friction reduces the shear strength of sea ice for a given normal stress, such that the fracture develops earlier in the simulation (i.e. under smaller surface forcing, Fig. 4.10). It also reduces the divergence associated with the elastic response when ice fractures and increase the convergence in the post-fracture viscous regime. This result is typical for granular material, with smaller fracture angles associated with larger angles of dilatancy and divergence during the fracture development.

The fracture angle is not sensitive to the Poisson ratio when the generalized stress correction scheme is used with a fixed stress correction path angle γ (Fig 4.11). This is in contrast with simulations using the standard stress correction scheme, where the fracture angle decreases with increasing ν [see blue points in Fig. 4.11, and also in *Dansereau et al.*, 2019]. Note that the Poisson ratio also affects the amount of shear and normal stress concentration associated with a local discontinuity in material properties [*Karimi and Barrat*, 2018]. The fact that the fracture angle is not affected by the changes in Poisson ratio thus indicates that the stress concentration and propagation of the fracture in space is mainly controlled by the stress correction rather than by the relaxation of material properties with damage. We speculate that the sensitivity of the fracture angle to the Poisson ratio in the standard stress correction scheme stems from the dependency of the stress correction path angle to the super-critical stress state (i.e. $\gamma = tan^{-1}(\sigma'_I/\sigma'_{II})$).

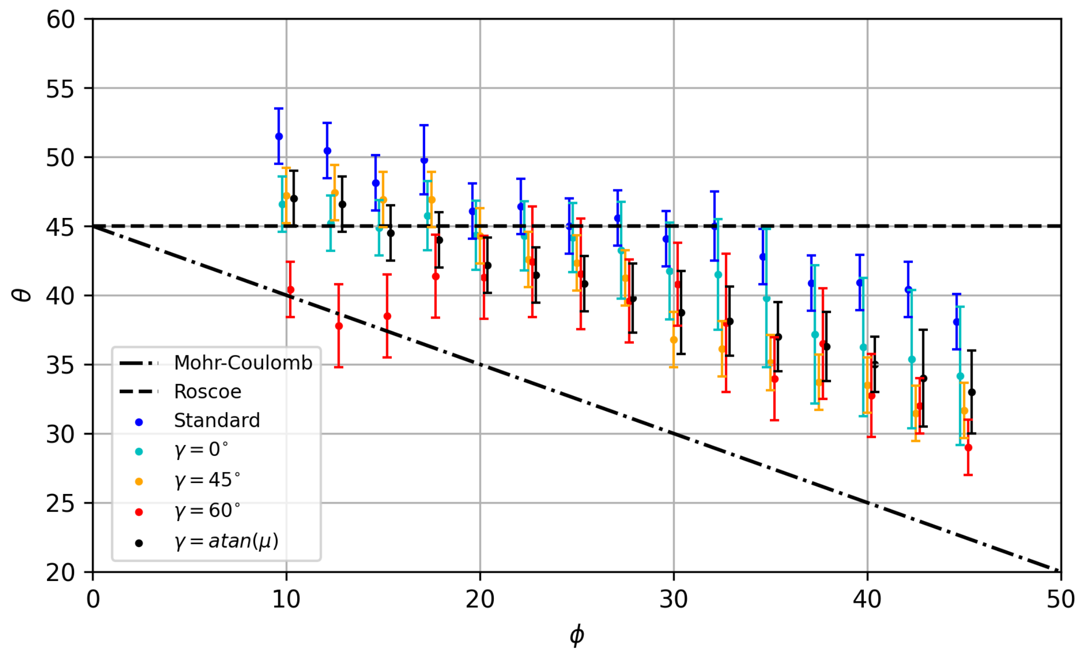

Figure 4.9: Sensitivity of the fracture angles (θ, degrees) on the angle of internal friction (ϕ, degrees), in uniaxial loading experiments using different correction path angle (γ). The correction path angle $\gamma = atan(\mu)$ implies that the stress correction path is perpendicular to the yield curve. The theoretical fracture angle from the Mohr-Coulomb and Roscoe theories are indicated by dashed and dash-dotted lines for reference.

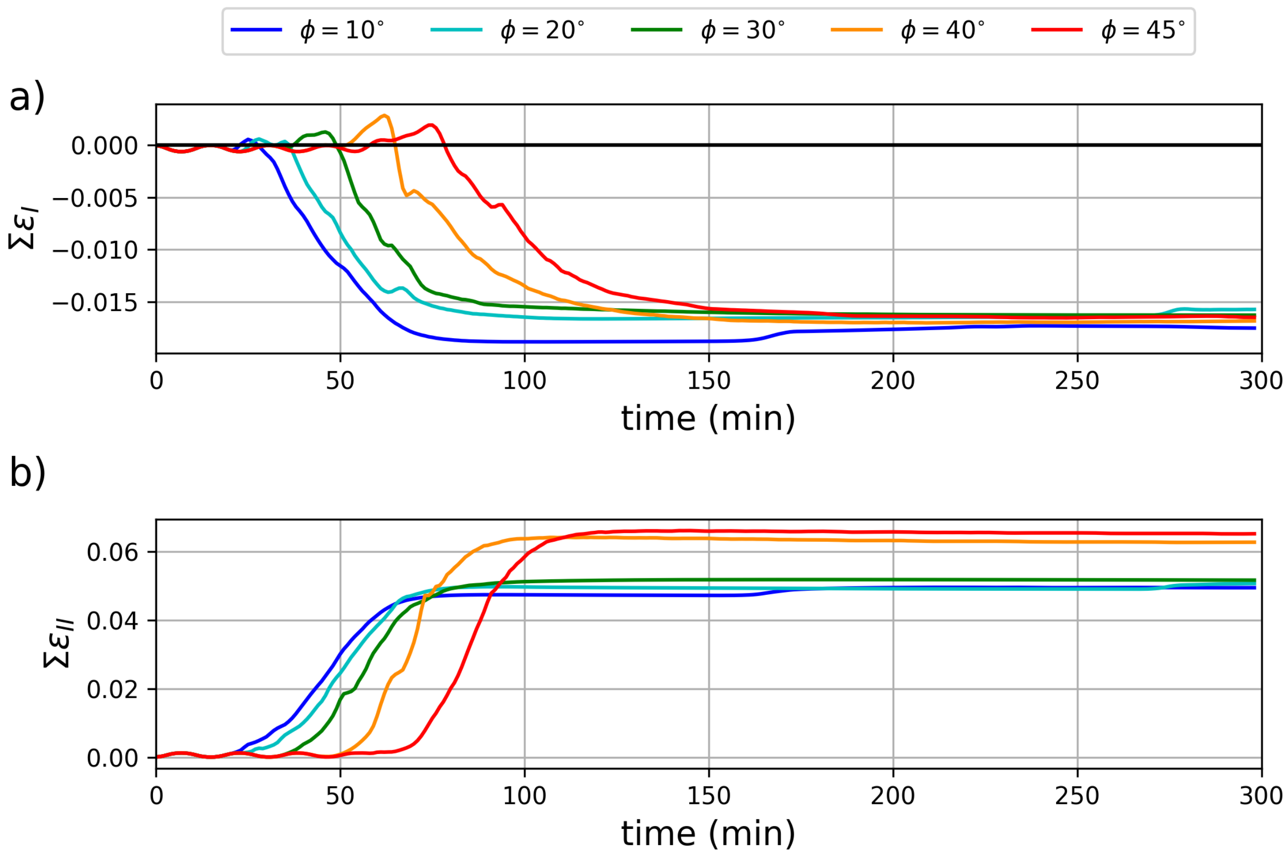

Figure 4.10: Time evolution of a) the mean normal strain rate invariant integrated over the ice cover (day^{-1}) and b) the maximum shear strain rate invariant integrated over the ice cover (day^{-1}), when using different angles of internal friction ϕ, with a stress correction path normal to the yield curve ($\gamma = \arctan(\mu)$).

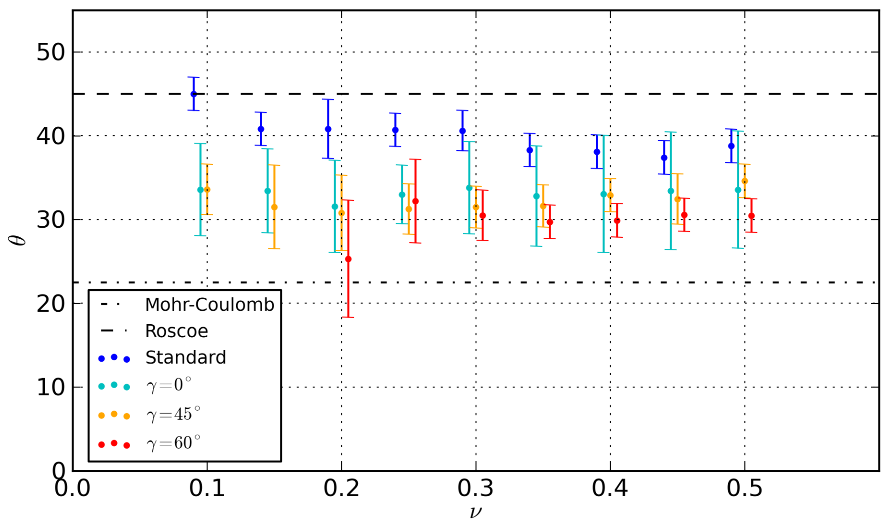

Figure 4.11: Sensitivity of the fracture angles (θ, degrees) on the Poisson ratio (ν, unitless), in uniaxial loading experiments using different correction path angle (γ). The theoretical fracture angle from the Mohr-Coulomb and Roscoe theories are indicated by dashed and dash-dotted lines for reference.

4.6 Discussion

The results presented above show that the generalized stress correction scheme reduces the growth of the residual error associated with the damage parameterization. Despite the improvement, some asymmetries are still present in the simulations ($\epsilon_{asym} < 10^{-2}$). This is due to the memory in the damage parameter (i.e. an integrated quantity) where residual errors accumulate and influence the temporal evolution of the solution. In regions of heavily damaged ice, the accumulated errors in the damage parameter result in large errors in the stress state due to the cubic dependence of the Maxwell viscosity η on d (Eq. 4.9). Future work includes replacing this formulation with a function that decreases the sensitivity of the Maxwell viscosity η for small changes in d around $d = 1$.

Overall, the use of a decohesive stress tensor yields smaller simulated fracture angles, without significantly impacting the material deformations. Using a large correction path angle γ ($> 45°$), however, significantly slows the damage production and reduces the simulated sensitivity of the fracture angle to the mechanical strength parameters. Based on these results, we suggest using a correction path that is normal to the yield criterion ($\gamma = \arctan \mu$). This value brings the simulated fracture angles closer to observations (see black points in Fig. 4.9) and reduces the amplification of residual errors, while correcting the super-critical stresses towards the closest point on the yield curve.

The simulation results show that in the MEB model, the damage develops at short time scales during which the elastic component of the rheology is important, while most of the deformations occur post-fracture over a longer time scale in the heavily damaged ice. This is in stark contrast with plastic models, in which a flow rule simultaneously dictates both the fracture development and the relative amount of shear and normal deformations occurring in the fractures. The decoupling between the development of damage and the post-fracture deformations in the MEB model explains that the type of deformations in the fracture remains similar [uniaxial convergence, i.e. ridging, contrary to observation, *Stern et al.*, 1995] despite the use of different stress correction path γ. This behaviour stems from the dominance of the viscous regime post-fracture: lead opening cannot occur when the stress state is compressive and remains limited to locations where tensile stresses are present, such as at the intersection of lines of fracture. This is contrary to granular theories, in which the distribution of contact normals determines the amount of ridging or lead opening (i.e. dilatancy) that is occurring when forced in uniaxial compression [*Balendran and Nemat-Nasser*, 1993]. This indicates that the decohesive stress tensor cannot be used to influence the deformations associated to the fracture of ice in the MEB rheology unless other parameterizations, such as including a decohesive strain tensor during the fractures [e.g., see *Schreyer et al.*, 2006; *Sulsky and Peterson*, 2011], are added to the rheology.

The viscous dissipation timescale (λ) in our model is set based on observations [$\sim 10^5$, *Tabata*, 1955; *Hata and Tremblay*, 2015a], and is one order of magnitude smaller than in other MEB implementations [*Dansereau et al.*, 2016; *Rampal et al.*, 2019]. The results from the model are robust to the exact value of λ for a range $10^5 - 10^7$; the increase λ being compensated by larger damage values along the fracture lines. For even larger λ values, divergence deformations persist longer in the simulation and the transition from elastic- to viscous-dominated regime occurs later in the simulation (see Fig. 4.12), decreasing the overall convergence along the fractures lines. If the transition to the viscous regime is removed (e.g. by setting $\alpha = 1$), divergence dominates throughout the simulations and reach large values as the leads open. The elastic wave are however no-longer dissipated in the fractures, leading to large and noisy deformation fields (divergence/convergence). These findings call for a different viscosity-dependence on damage leading to both dissipation of elastic waves and a more realistic post-fracture deformation field.

Note that the results presented above neglect heterogeneity in the ice cover, a factor that is responsible for much of the brittle material behaviour in progressive damage models [*Amitrano and Helmstetter*, 2006]. Heterogeneity was neglected in the analysis above to isolate the growth of the residual errors. While including heterogeneity does not change the overall physics and sensitivity to the damage parameterization, it creates irregular sliding planes instead of the linear diamond shape fractures (Fig. 4.13a), naturally creating contact points where ridging occurs with lead opening elsewhere along the fracture lines. This results in a form of granular dilatancy typical of granular materials.

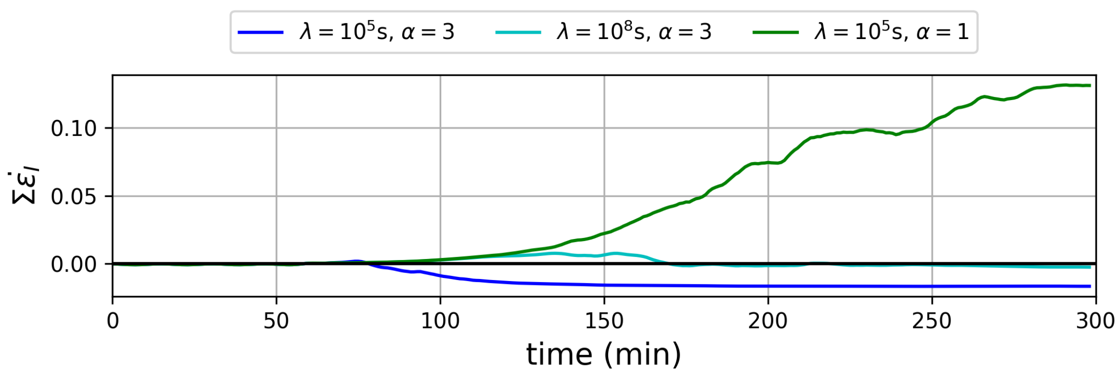

Figure 4.12: Time evolution of the mean normal strain rate invariant integrated over the ice cover (day^{-1}) using a stress correction path normal to the yield curve ($\gamma = \arctan(\mu)$) with $\alpha = 3$ (blue), $\alpha = 1$, and a longer viscous dissipation time-scale ($\lambda = 10^8$ s).

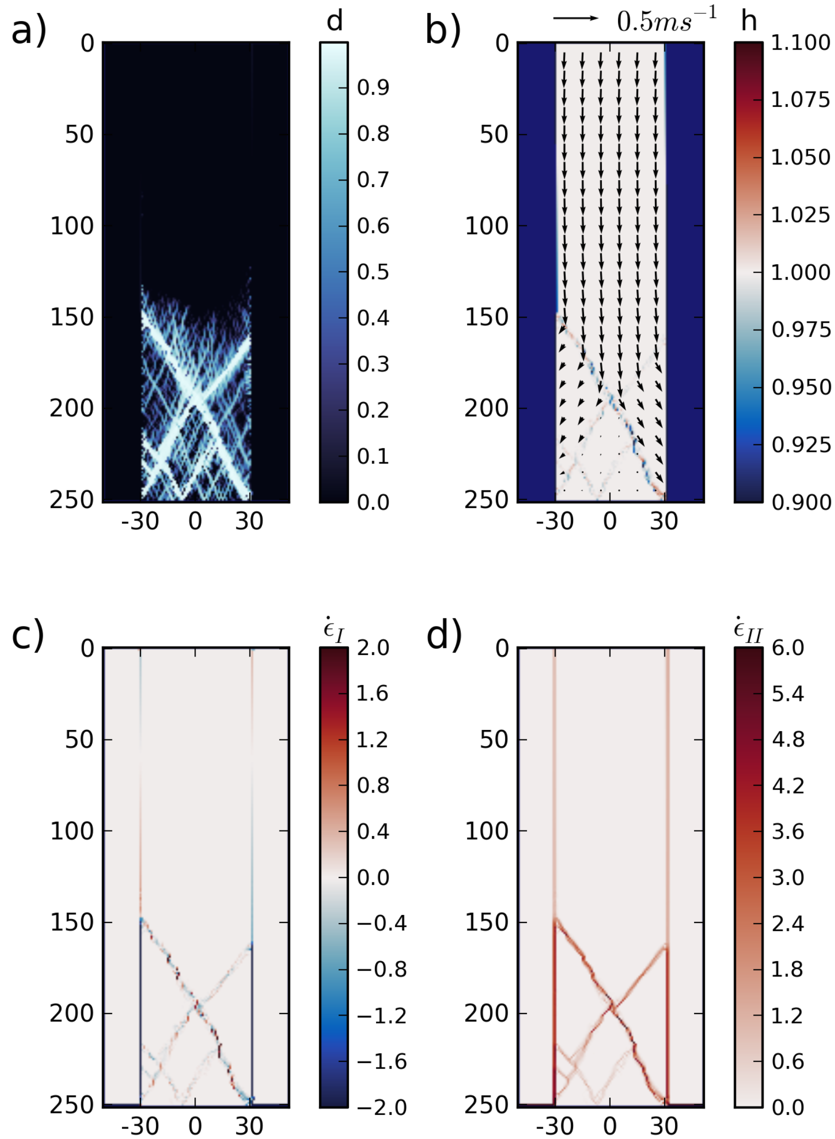

Figure 4.13: a) Damage (unitless), b) ice thickness (m, color) and velocity vectors (m s^{-1}), c) mean normal strain rate invariant ($\dot{\epsilon}_I$, day^{-1}) and d) maximum shear strain rate invariant ($\dot{\epsilon}_{II}$, days^{-1}) after two hours of integration in using the generalized stress correction scheme with $\gamma = 45°$ and including heterogeneity in the initial material cohesion field. The heterogeneous cohesion (c_0) field is defined locally at each grid cell by picking a random number between 7.0 and 13.0 kN m^{-2}. The remaining initial conditions are the same as all other simulations.

4.7 conclusion

We propose a generalized stress correction scheme for the damage parameterization to reduce the growth of residual errors in the MEB sea ice model. To this end, we scale the damage factor Ψ based on the super-critical maximum shear stress invariant (σ'_{II}) only, together with a decohesive stress tensor defining the path from the super-critical stress state to the yield curve. The sensitivity of the fracture angles and sea-ice deformations to these changes are investigated in the context of the uniaxial compression experiment similar to those presented in *Ringeisen et al.* [2019].

Our results show that in the MEB rheology, most of the deformations occur post-fracture in heavily damaged ice, where the viscous term is dominant. This causes a predominance of convergence (ridging) in the fractures, contrary to laboratory experiments of granular materials and satellite observations of sea ice. The use of a decohesive stress tensor influences the fracture angle of sea ice, but does not influence the type of deformation rates (convergence and shear), nor the simulated dilatancy. Future work will involve the modification of the non-linear relationship between the Maxwell viscosity and the damage. We also show that the sensitivity of the fracture angle to the Poisson ratio, seen when using the standard damage parameterization, disappears when using the generalizes stress correction scheme with a fixed stress correction path. This suggests that in the MEB model, the stress concentration and fracture propagation is governed by the stress correction rather than by the relaxation of the mechanical properties associated with the damage.

Based on our results, using the generalized damage parameterization with a stress correction path normal to the yield curve reduces the growth of residual errors and allows for the production of longer term simulations with post-fracture deformations. Using this stress correction path also reduces the fracture angles by $\sim 5°$, bringing them in the range of observations. Despite these improvements, some error growth remains inherent to the formulation of the damage parameterization. Whether this might be improved by removing the dependency of the damage parameters on the damage factor (and on the super-critical stress state) will be explored in future work.

Chapter 5

A comparison of sea-ice deformations, fractures and arches simulated by the Viscous-Plastic and Maxwell Elasto-Brittle models

This paper investigates the influence of the rheology on the simulated sea ice deformations and fractures, in the context of ideal landfast ice simulations ran with our Viscous-Plastic and Maxwell Elasto-Brittle models. In particular, we investigate the different location of the simulates ice arches in a channel in the VP and MEB models. This paper will be submitted in early 2021 for publication in The Cryosphere Discussions.

A comparison of sea-ice deformations, fractures and arches simulated by the Viscous-Plastic and Maxwell Elasto-Brittle models

Mathieu Plante[1] and Bruno Tremblay[1]

[1]Department of Atmospheric and Oceanic Sciences, McGill University, Montréal, Québec, Canada

The manuscript reproduced here is in preparation for submission to the journal The Cryosphere Discussions.

Abstract

The influence of the rheology on sea-ice deformations and the formation of landfast ice arches is investigated by comparing ideal simulations performed with the standard Viscous Plastic (VP) rheology and the generalized Maxwell Elasto-Brittle (MEB) rheology, both implemented in the McGill Sea Ice Model version 5. First, the simulated deformations in the different regimes of the rheologies (viscous creep or plastic in the VP model, visco-elastic or post-fracture viscous in the MEB model) are investigated in 1D lead opening and ridging experiments. Results show that both rheologies produce small viscous creep deformations in the simulated landfast ice and present a similar transition to large deformations when the ice fractures, caused by a decrease of the elastic and viscous coefficients. In ideal ice arches simulations, both models produce similar fractures when using equivalent yield curves. The differences between simulations mostly relate to the rates of deformation along the fractures: the normal flow rule of the VP model creates linear ridges and smoother ice deformations, while the non-linear post-fracture viscosity in the MEB model creates non-linear (concave) ridges and larger local variations in the deformations. Ice arches form upstream of a channel after 2-3 days of time integration when the ice upstream of the channel is capable of sustaining the normal load and stops ridging. The formation of the ice arches thus depends on the included compressive and shear strength, which increase with the ice thickness. An arching lead however only opens if the ice in the channel downstream is drifting. The tendency to form stable ice arches downstream of the channel in the MEB model is caused by the post-fracture deformations within the channel, creating local ridges with sufficient strength for new ice arches to form. Results are insensitive to changes in the VP model maximum viscosity, contrary to what has been previously reported.

5.1 Introduction

When forced into narrow passages, sea ice jams and creates an ice arch, sustaining a landfast ice cover upstream [*Kwok*, 2005; *Vincent*, 2019]. The area downstream of these ice arches subsequently opens into a semi-permanent area of open water, or polynya, and becomes an important gathering location for marine mammals [*Carmack and Macdonald*, 2002]. In the Canadian Arctic Archipelago, much of the ice cover becomes landfast for several months via this process [*Melling*, 2002; *Galley et al.*, 2012], limiting maritime transport but allowing safe on-ice transport routes between northern communities until their break up in the melt season.

In sea-ice models, the formation of ice arches depends on the rheology determining the relationship between ice stress and deformations for the different regimes defined by the yield curve. In most coupled models, the sea ice component uses the standard Viscous Plastic rheology [or modifications thereof, *Hibler*, 1979; *Hunke*, 2001] with an elliptical yield curve and normal flow rule. In the standard model, the ellipse does not have sufficient cohesion and/or shear strength to sustain an ice arch at key locations, such as Lancaster Sound or Nares Strait [*Dumont et al.*, 2008]. To improve the representation of landfast ice arches, the yield curve can be modified either by decreasing the ellipse ratio or by increasing the bi-axial tensile strength [*Dumont et al.*, 2008; *Lemieux et al.*, 2016; *Olason*, 2016]. Despite these changes, the simulated landfast ice break-up and onset remains poorly represented in areas subjected to strong surface forcings such as tides [in the CAA, *Lemieux et al.*, 2018] or stormy weather [e.g. in the Kara sea, *Olason*, 2016; *Lemieux et al.*, 2016]. In the Kara sea, increasing the parameterized maximum viscosity, which defines the transition between the viscous and plastic regimes in the VP model, was shown to improve the representation of landfast ice [*Olason*, 2016]. This sensitivity is not found in other VP models [*Lemieux* *et al.*, 2018], which raises the question as to whether the numerical implementation of a given model influences the simulated landfast ice cover.

In recent years, different approaches for the ice fracture have been developed for sea-ice models. Among these new approaches, many included a form of material memory of the past fractures to influence the localisation of future deformations [*Schreyer et al.*, 2006; *Sulsky and Peterson*, 2011; *Rampal et al.*, 2016; *Dansereau et al.*, 2016]. In the Elasto-Brittle [EB *Rampal et al.*, 2016, 2019] and the Maxwell Elasto-Brittle [MEB *Dansereau et al.*, 2016] rheology, fracture is represented by a damage parameter which relaxes the elastic modulus and viscous coefficients in the constitutive equation, preconditioning the ice for large and permanent deformations. In idealized and realistic Nares strait simulations, the MEB model produces both stable arches below which a polynya forms and unstable arches that temporarily form at various positions in and upstream of the channel as part of the break up process [*Dansereau et al.*, 2017]. The stable arches and associated polynya in the MEB model are mostly located at the channel exit [*Dansereau et al.*, 2017; *Plante et al.*, 2020], contrary to the observed locations, such as upstream of Smith Sound or Robeson channel [*Vincent*, 2019].

The formation of ice arches downstream of a channel in the MEB rheology was assessed by *Plante et al.* [2020], and their stability was shown to depend on the material cohesion included in the yield criterion [*Plante et al.*, 2020]. When the ice arch collapses, shear fractures form upstream of the channel at some angle from the coast, forming a funnel between which the ice is drifting. Whether stable ice arches can form within this funnel in longer simulations, as typically observed, was not investigated due to the growth of residual errors associated with the damage parameterization [*Plante et al.*, 2020]. This issue was improved, but not completely removed, by the use of a generalized stress correction scheme in the damage parameterization [*Plante and Tremblay*, 2020].

In this paper, we compare the behaviour of both the VP and MEB rheologies in simple and idealized simulations where one of the three modes of failure (tensile, compressive, shear) is isolated. We do this comparison using the same numerical implementation within the McGill Sea Ice Model [*Tremblay and Mysak*, 1997; *Lemieux et al.*, 2008; *Plante et al.*, 2020]. First, 1D ridging and lead opening simulations are used to describe and compare the material behaviour simulated by the two rheologies in different deformation regimes (e.g. visco-elastic in the MEB model, viscous-plastic in the VP model). We then revisit the ideal ice bridge experiment of [*Plante et al.*, 2020] in the context of long-term simulations (∼10 days) using the VP and the MEB model with the generalized stress correction scheme [*Plante and Tremblay*, 2020] to study the formation and position of ice arches that form post-fracture in the funnel created upstream of the channel as part of the landfast ice collapse.

This paper is organized as follows. The MEB and VP rheologies are described briefly in section 2. The different experiments used in the analysis are described in section 3. Results from idealized experiments are presented in section 4 followed by a discussion of the simulated ice arches and their sensitivity to various model parameters in section 5. The main findings and conclusions are summarised in section 6.

5.2 Model

In the McGill Sea Ice Model, we solve a simplified version of the vertically integrated 2D momentum equation for sea ice , as:

$$\rho_i h \frac{\partial \boldsymbol{u}}{\partial t} = \nabla \cdot \boldsymbol{\sigma} + \boldsymbol{\tau}, \tag{5.1}$$

where ρ_i is the ice density, h is the mean ice thickness, $\boldsymbol{u}$ $(= u\hat{\boldsymbol{\imath}} + v\hat{\boldsymbol{\jmath}})$ is the ice velocity vector, $\boldsymbol{\sigma}$ is the vertically integrated internal stress tensor and $\boldsymbol{\tau}$ is the total external surface forcing (from winds and ocean currents). In this analysis, we exclude the ice grounding, the Coriolis and the advection of momentum terms. These simplifications are acceptable in the context of idealized experiments but would cause errors in realistic simulations [*Turnbull et al.*, 2017].

Following *Plante et al.* [2020], the total surface stress $\boldsymbol{\tau}$ – representing both the surface stress ($\boldsymbol{\tau}_a$) and the drag of a still ocean under the drifting ice – is written as:

$$\boldsymbol{\tau} \approx \boldsymbol{\tau}_a - \rho_w C_{dw} |\boldsymbol{u}| \boldsymbol{u}, \tag{5.2}$$

where ρ_w is the water density and C_{dw} is the water drag coefficient.

The temporal evolution for the mean ice thickness h (volume per grid cell area) and concentration A are written as:

$$\frac{\partial h}{\partial t} + \nabla \cdot (h\boldsymbol{u}) = 0 \tag{5.3}$$

$$,\frac{\partial A}{\partial t} + \nabla \cdot (A\boldsymbol{u}) = 0, \tag{5.4}$$

where the thermodynamics source terms are neglected. Model constants and mechanical strength parameters are listed in Table 5.1.

Table 5.1: Default Model Parameters

Parameter	Definition	Simulations	Value
Δx	Spatial resolution	Common	2 km
Δt	Time step)	VP / MEB	60 s / 0.5 s
ρ_a	Air density	Common	1.3 kg m^{-3}
ρ_i	Sea ice density	Common	9.0×10^2 kg m^{-3}
ρ_w	Sea water density	Common	1.026×10^3 kg m^{-3}
C_{da}	Air drag coefficient	Common	1.2×10^{-3}
C_{dw}	Water drag coefficient	Common	5.5×10^{-3}
T_d	Damage time scale	MEB	2 s
T_h	Damage healing time scale	MEB	10^5 s
Y	Young Modulus	MEB	10^9 N m^{-2}
ν	Poisson ratio	MEB	0.3
λ_0	Viscous relaxation time	MEB	10^5 s
ϕ	Angle of internal friction	MEB	45°
γ	Correction path angle	MEB	$\arctan(\sin\phi)$
c_0	Cohesion	MEB	10 kN m^{-2}
α	Non-linear viscosity parameter	MEB	3
σ_{c_0}	Compressive strength	MEB_{eq}	78 kN m^{-2}
Δ_{min}	Creep limit	VP	2.0×10^{-9} s
P^*	Compressive strength	VP_{std} / VP_{eq}	27.5 / 73.4 kN m^{-2}
T^*	Tensile strength	VP_{std} / VP_{eq}	0.0 / 5.0 kN m^{-2}
S^*	Shear strength	VP_{std} / VP_{eq}	13.75 / 28.0 kN m^{-2}
e	Ellipse ratio	VP_{std} / VP_{eq}	2 / 1.4

5.2.1 Maxwell elasto-brittle rheology

The constitutive equation in the MEB rheology is written as:

$$\frac{\partial \boldsymbol{\sigma}}{\partial t} + \frac{1}{\lambda}\boldsymbol{\sigma} = \mathbf{C}_{MEB} : \dot{\boldsymbol{\epsilon}}, \tag{5.5}$$

where λ is the viscous time relaxation, ":" denotes the double dot product of tensors, $\dot{\boldsymbol{\epsilon}}$ is the strain rate tensor and $\mathbf{C}$ is the elastic tensor, defined as:

$$\mathbf{C} = \frac{E}{1-\nu^2}\begin{pmatrix} 1 & \nu & 0 \\ \nu & 1 & 0 \\ 0 & 0 & 1-\nu \end{pmatrix}, \tag{5.6}$$

where E is the vertically integrated elastic stiffness and ν ($= 0.33$) is the Poisson ratio.

The elastic stiffness E and viscous relaxation time λ in Eq. 5.5 are written as :

$$E = Yhe^{-a(1-A)}(1-d), \tag{5.7}$$

$$\lambda = \lambda_0(1-d)^{\alpha-1}, \tag{5.8}$$

where Y ($=$ 1 GPa, or 10^9 N m^{-2}) is the Young Modulus of undeformed sea ice, d ($0 < d < 1$) is the damage parameter used to represent the fracture of ice, $a = 20$ is the standard parameter ruling sea ice concentration dependencies [*Hibler*, 1979], λ_0 ($= \eta_0/Y = 10^5$) is the viscous relaxation time scale in undamaged sea ice and η_0 is the viscosity of undeformed see ice. Note that the viscous relaxation time scale λ determines the relative importance of the elastic and viscous stress terms. In the standard rheology [*Dansereau et al.*, 2016], it is set so that the elastic component is dominant in the undamaged sea ice (when d=0) but not in the heavy damaged sea ice (when $d \sim 1$), where post-fracture viscous deformations dominate [*Plante and Tremblay*, 2020]. Below, we remove the elastic component in some simulations by increasing the Young Modulus to $Y = 10^{14}$ N m^{-2} and the relaxation time scale to $\lambda_0 = 1.0$ s, without changing the viscosity η_0, effectively isolating the permanent viscous creep from the reversible elastic deformations.

In the MEB rheology, the ice fracture is parameterized in terms of a damage parameter d that increases when the internal stress state exceeds the yield criterion [*Rampal et al.*, 2016]. The MEB rheology is usually used with a Mohr-Coulomb yield curve where the shear strength is linearly related to the normal stress (red curve in Fig. 5.1). A cut-off on the compressive strength can also be used with the Mohr-Coulomb curve (orange curve in Fig. 5.1). The Mohr-Coulomb and compressive strength criteria (denoted by F_{mc} and F_{p} respectively) are written as:

$$F_{\text{mc}}(\sigma) = \sigma_{II} + \mu\sigma_I - c_0 h e^{-a(1-A)} < 0, \tag{5.9}$$

$$F_{\text{p}}(\sigma) = \sigma_{II} - \sigma_I - \sigma_{c0} h e^{-a(1-A)} < 0, \tag{5.10}$$

where $\mu = \sin\phi$ is the coefficient of internal friction of ice, ϕ ($= 45°$) is the angle of internal friction, c_0 is the cohesion of sea ice, $a = 20$ is the standard parameter ruling sea ice concentration dependencies [*Hibler*, 1979] and σ_{c0} is the compressive strength of ice. In this study, the cohesion c_0 is set to 10 kN m^{-2} [*Plante et al.*, 2020], and the compressive strength σ_{c0} is set to 78 kN m^{-2} so that it corresponds to the maximum uni-axial compressive strength in equivalent VP experiments (see section 5.2.1.1 below). Hereafter, we use the subscript *std* and *eq* to refer to simulations ran with and without including compressive strength cut-off in the yield curve.

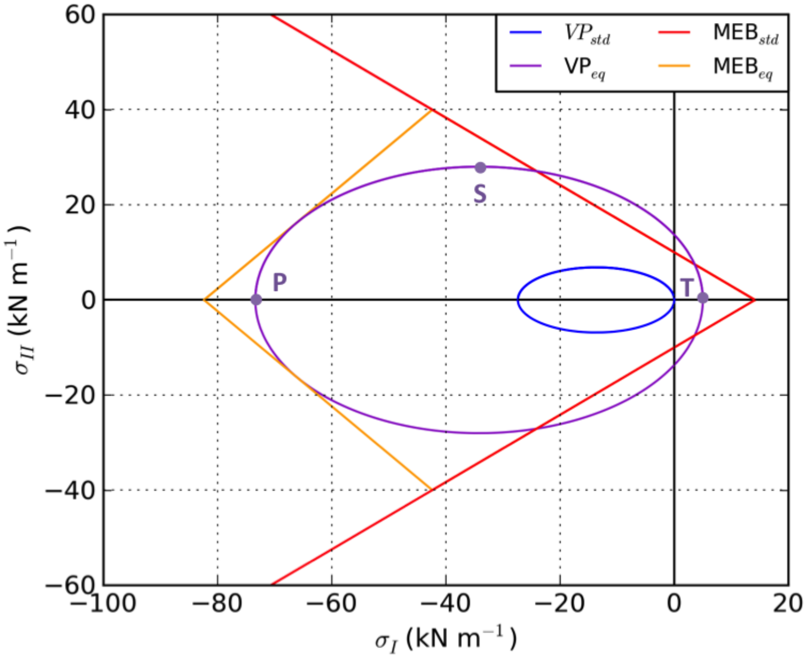

Figure 5.1: Different yield criteria used in the VP and MEB simulations, in the stress invariant space. The standard yield curves used with the VP and MEB rheologies are presented in blue and red respectively. To run simulations with equivalent strength parameters, the ellipse is increased in size (purple curve) and a compressive strength criterion is added to the Mohr-Coulomb yield curve (orange).

The temporal evolution of the damage parameter d is parameterized as a relaxation term with time scale T_d (= 1 s) and a linear thermodynamic healing term acting on longer time scales T_h [= 10^5 s *Maykut and Untersteiner*, 1971]:

$$\frac{\partial d}{\partial t} = \frac{(1-\Psi)(1-d)}{T_d} - \frac{d}{T_h}, \tag{5.11}$$

where Ψ is a damage factor ($0 < \Psi < 1$) defined as the scaling factor required to bring a super-critical stress state back on the yield curve. Following *Plante and Tremblay* [2020], we define a generalized stress correction scheme with Ψ written as:

$$\Psi = \begin{cases} \frac{c+\mu\gamma\sigma'_{II}-\mu\sigma'_I}{(1+\mu\gamma)\sigma'_{II}} & \text{if } \sigma'_I < \sigma'_{II}\tan\gamma \\ \frac{\sigma_c}{\sigma'_I-\sigma'_{II}} & \text{if } \sigma'_I - \sigma'_{II} < \sigma_c \\ \frac{c}{(\sigma'_{II}+\mu\sigma'_I} & \text{otherwise,} \end{cases} \tag{5.12}$$

where (σ'_I,σ'_{II}) are the super-critical stress invariant prior to the correction, γ (= $\arctan\mu$) is the stress correction path angle (see Fig. 5.2a) and c (= $c_0 h e^{-a(1-A)}$) is the vertically integrated cohesion. In this model, we use the standard stress correction when the stress exceeds the compressive cut-off (Fig. 5.2b).

When fracture occurs, the prognostic equation for the corrected stress state is defined as:

$$\frac{\partial \boldsymbol{\sigma'}}{\partial t} = -\frac{(1-\Psi)\boldsymbol{\sigma'} + \boldsymbol{\sigma}_D}{T_d}, \tag{5.13}$$

where $\boldsymbol{\sigma}_D$ represents the decohesion stress tensor. The reader is referred to *Plante and Tremblay* [2020] for more details.

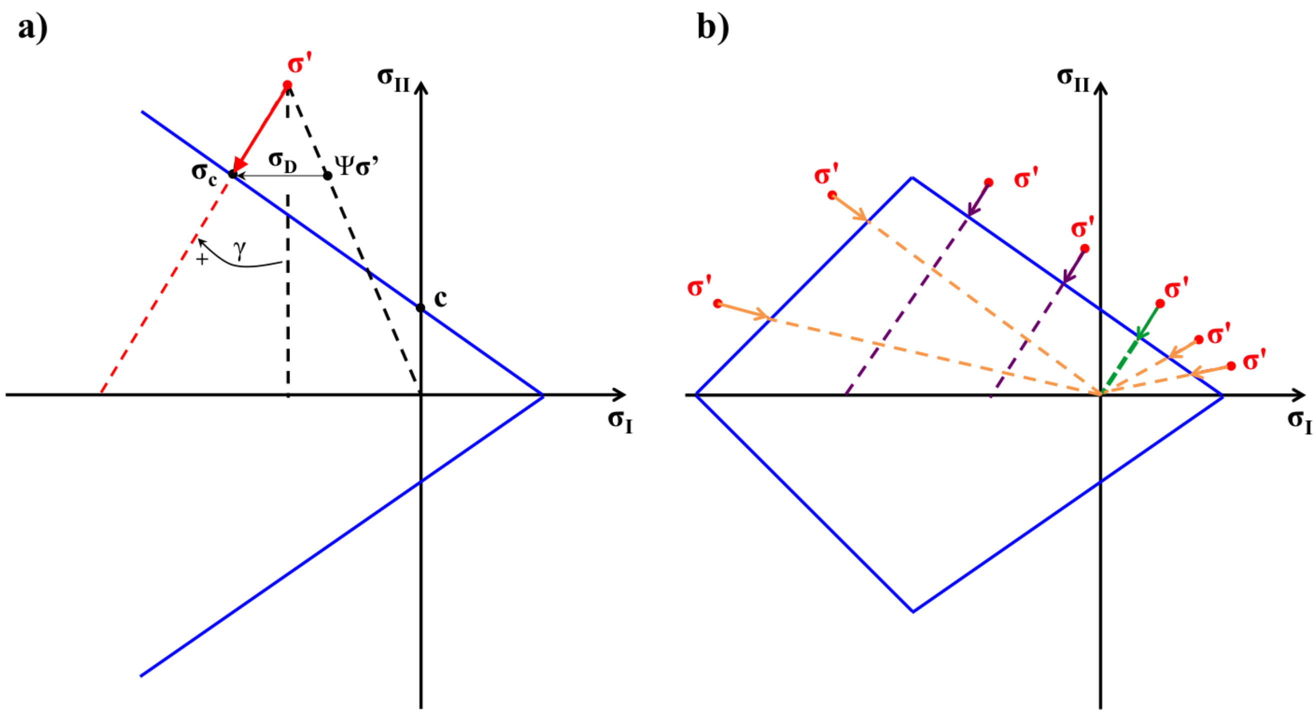

Figure 5.2: a) Mohr-Coulomb yield criterion in stress invariant space. $\boldsymbol{\sigma}'$ is the uncorrected super-critical stress state, $\boldsymbol{\sigma}_c$ the critical stress state for a given correction path angle γ (red dashed line) and c is the cohesion. The decohesion stress tensor $\boldsymbol{\sigma}_D$ is defined as the difference between $\boldsymbol{\sigma}_c$ and the scaled super-critical stress ($\Psi\boldsymbol{\sigma}'$). b) Generalized stress correction paths for various super-critical stresses $\boldsymbol{\sigma}'$. Paths to the origin (orange) are used for large tensile stresses and for the compressive strength criterion. A correction path normal to the yield curve is used otherwise (purple). The green line indicates the points where both formulations represent the same path.

If we set $d = 0$ and $\Psi = 1$ at all times, the ice behaves like a visco-elastic material with constant elastic stiffness and viscosity. We refer to this as "fracture component disabled" in the following.

5.2.1.1 Viscous-Plastic rheology

The constitutive equation of the VP rheology is usually written in Einstein tensor notation as :

$$\sigma_{ij} = 2\eta\dot{\epsilon}_{ij} + (\zeta - \eta)\dot{\epsilon}_{ij}\delta_{kk} + \delta_{ij}P_p/2, \tag{5.14}$$

where,

$$\dot{\epsilon}_{ij} = \frac{1}{2}\left[\frac{\partial u_i}{\partial x_j} + \frac{\partial u_j}{\partial x_i}\right], \tag{5.15}$$

σ_{ij} and ϵ_{ij} are the internal stresses and strain rates acting in the jth direction on a plane perpendicular to the ith direction, η and ζ are the shear and bulk viscous coefficients respectively, δ_{ij} is the Kronecker delta, P_p $(= (P+T)/2)$ is the ice pressure, P is the vertically integrated compressive strength of sea ice and T is the vertically integrated tensile strength of sea ice. To ease comparison with the MEB rheology, Eq. 5.14 can be rewritten in matrix form as:

$$\boldsymbol{\sigma} = \mathbf{C}_{\mathrm{VP}} : \dot{\boldsymbol{\epsilon}} + \frac{P_p}{2}\mathbf{I}, \tag{5.16}$$

where

$$\mathbf{C}_{\mathrm{VP}} = \begin{pmatrix} \zeta + \eta & \zeta - \eta & 0 \\ \zeta - \eta & \zeta + \eta & 0 \\ 0 & 0 & 2\eta \end{pmatrix}, \tag{5.17}$$

$\mathbf{C}_{\mathrm{VP}}$ is the non-linear viscous coefficient tensor and $\mathbf{I}$ is the identity tensor.

The viscous coefficients are defined as:

$$\zeta = \frac{P+T}{2\Delta} \qquad , \qquad \eta = \frac{\zeta}{e^2}, \tag{5.18}$$

where Δ (s) can be derived from the yield curve and the normal flow rule as:

$$\Delta = max\ (\ \Delta_{min}\ ,\ [\ (\dot{\epsilon}_{11}^2 + \dot{\epsilon}_{22}^2)(1+e^{-2}) + 4e^{-2}\dot{\epsilon}_{12}^2 + 2\dot{\epsilon}_{11}\dot{\epsilon}_{22}(1-e^{-2})\ ]^{\frac{1}{2}}), \tag{5.19}$$

where Δ_{min} (= 2.0x10^{-9} s) determines the maximum viscosity (ζ_{max},η_{max}) in the (linear) viscous creep regime. In the plastic regime the (non-linear) viscous coefficients are inversely proportional to the strain-rates, such that the stress state is strain-rate independent and lies on the yield criterion.

The transition between the viscous and plastic regimes is defined by the yield curve, defined in standard VP model as an ellipse (with aspect ratio e) in stress invariant space (σ_I,σ_{II}). Following [*Bouchat and Tremblay*, 2017], we write the yield criterion in general terms of the vertically integrated compressive strength (P), tensile strength [T, *Beatty and Holland*, 2010] and the shear strength S (see Fig. 5.1), as:

$$F_{\mathrm{vp}} = \left[\frac{\sigma_I + \left(\frac{P-T}{2}\right)}{\left(\frac{P+T}{2}\right)}\right]^2 + \left[\frac{\sigma_{II}}{S}\right]^2 - 1 = 0, \tag{5.20}$$

where,

$$P = P^* h e^{-a(1-A)}, \tag{5.21}$$

$$T = T^* h e^{-a(1-A)}, \tag{5.22}$$

$$S = S^* h e^{-a(1-A)}, \tag{5.23}$$

P^* is the bi-axial compressive strength, T^* is the bi-axial tensile strength and S^* is the maximum shear strength. The ellipse aspect ratio, defined as the major over minor axis of the ellipse, can be written a:

$$e = \frac{P^* + T^*}{2S^*}. \tag{5.24}$$

In the standard VP model, $T^* = 0.0$ kN m^{-2}, $P^* = 27.5$ kN and $S^* = 6.875$ kN m^{-2}, (e=2, blue curve in Fig. 5.1), resulting in a much smaller yield envelope than the Mohr Coulomb criterion used in the MEB with the standard strength parameters (i.e. see Fig. 5.1). In order to compare the MEB and VP rheologies with similar yield envelope, we define a second ellipse with T^*=5kN m^{-2}, P^*=73.4 kN m^{-2} and S^* =28 kN m^{-2} ($e = 1.4$, purple curve in Fig. 5.1). This yield curve has mechanical strength parameters in line with [*Dumont et al.*, 2008; *Lemieux et al.*, 2016; *Olason*, 2016] but with a biaxial compressive strength much larger than usually used in sea-ice models, although still in the range of observations [*Richter-Menge and Elder*, 1998; *Tremblay and Hakakian*, 2006].

Note that the plastic flow rule is written in the same form as a Newtonian (viscous) compressible constitutive relation, albeit with viscous coefficients that are inversely proportional to the strain rates. Large (plastic) deformations, therefore, are the result of decreasing viscous coefficients in a manner analogous to the damage parameter that decreases the elasticity and viscosity of ice in the MEB rheology. The plasticity in the VP model can thus be compared to the MEB damage by defining:

$$d_{\text{VP}} = 1 - \frac{\zeta}{\zeta_{max}}, \tag{5.25}$$

such that d_{VP} is identical equal to zero when the ice deformation rates are small (viscous regime) but tends to 1 when the deformation rates are large (plastic regime). Note that the plastic damage builds up instantaneously, and immediately relaxes to 0 once the loading becomes sub-critical. That is, the memory of past deformations in the VP model rests entirely in the changes in ice thickness and concentration via the continuity equations, an important difference with the MEB rheology where memory resides somewhat in the elastic stresses but more importantly in the damage parameter. Note that this damage memory is not intrinsically associated with elasticity, and can be implemented in VP (or other) models.

In the VP rheology, the fracture component is disabled by setting $d_{\mathrm{VP}} = 0$ ($\Delta = \Delta_{min}$), such that the ice remains in the viscous regime independently of the stress state. This corresponds to the viscous creep experiment of [*Beatty and Holland*, 2010].

5.3 Methods

5.3.1 Numerics

The VP and MEB models are both implemented in the McGill Sea Ice Model using an Eulerian, 2nd order finite difference numerical scheme [*Tremblay and Mysak*, 1997; *Lemieux et al.*, 2014; *Plante et al.*, 2020]. The equations are discretized in space using an Arakawa C-grid and in time using a semi-implicit backward Euler scheme. A solution to the non-linear momentum and constitutive equations are found using a Picard solver. This solver uses an outer loop in which the non-linear terms are updated at each iteration based on the solution to the linearized equations, until the L2-norm of the solution converges to a set residual tolerance (ϵ_{res}). The linearized equations are solved using a preconditioned Flexible General Minimum RESidual method [*Lemieux et al.*, 2008, FGMRES]. When using the VP rheology, the residual tolerance ϵ_{res} is set to 10^{-3} N/m^2. When using the MEB rheology, it is set to 10^{-6} N/m^2 to limit the growth of residual errors and the development of asymmetry in the solution – allowing for longer-term integration. The prognostic equations for h, A and d are solved simultaneously using the IMplicit-EXplicit (IMEX) approach [*Lemieux et al.*, 2014].

5.3.2 Ideal experiments

We document the sensitivity of the simulated sea-ice deformations and fractures on the rheology using ideal simulations: a 1D ice ridging and lead opening experiment and a 2D landfast ice arch experiment. The ideal simulations are run with both the VP model and the MEB model with the generalized stress correction scheme. For each model, the experiments are repeated using: 1. the standard yield curve, 2. the material-equivalent yield curve, and 3. the material-equivalent yield curve with different elastic or viscous coefficients.

5.3.2.1 1D lead opening or ridging experiments

The first experiment consist in 1D simulations in which the ice is forced along the long-axis (N-S) of a rectangular domain (20 x 400 km) with a no-slip (Dirichlet, u=v=0) boundary at the bottom, an open (Neumann, du/dn=dv/dn=0) boundary at the top and periodic boundaries at the sides (Fig. 5.3a). The initial conditions for sea ice are zero ice velocity, uniform 1m ice thickness, 100 % concentration and zero damage. The spatial resolution is 2 km and the time step is set to 60 s in the VP model and 0.5 s in the MEB model, in accord with their respective Courant–Friedrichs–Lewy (CFL) criterion [*Williams et al.*, 2017; *Plante et al.*, 2020]. A constant surface forcing ($\tau_a = 0.62$ N m^{-2} for the lead opening experiment and $\tau_a = -0.62$ N m^{-2} for the ridging experiment, see arrows in Fig. 5.3a) is imposed on the entire ice surface for 5 h, then removed ($\tau_a = 0$ N m^{-2}) for the next 5 h to differentiate the permanent from the reversible deformations. The change in the surface forcing is stepped without ramping to investigate the elastic-wave response in the MEB model.

In the following, we run the 1D lead opening and ridging simulations twice – with and without d and d_{VP} set to zero – to isolate the viscous regime from the plastic regime in the VP model and the visco-elastic regime from the post-fracture viscous regime in the MEB model. This is done to compare the transition between the small and large deformation regimes in the two models and the resulting material discontinuity.

5.3.2.2 Ice arch experiments

In the second experiment, we revisit the ideal ice bridge simulation of *Plante et al.* [2020] in the context of longer simulations under a constant wind forcing. This domain is 200 x 800 km with a narrow channel 200 km long and 60 km wide at the center, located 300 km away from the top and bottom boundaries (Fig. 5.3). The boundary conditions are periodic on the left and right boundaries, closed (Dirichlet, u=v=0) on the top boundary and open (Neumann conditions, du/dn=dv/dn=0) on the bottom boundary. The initial conditions for sea ice are zero ice velocity, uniform 1m ice thickness, 100 % concentration and zero damage. The spatial resolution is 2 km and the time step of 60 s for the VP model and 0.5 s for the MEB model. A southward forcing is imposed on the ice surface, ramped up from 0 to 0.625 N m^{-2} in a 2h period, then kept constant for the remaining of the 10-day long simulations. This unrealistically large forcing serves to produce simulations with extensive ice fractures and to determine their influence on the formation of stable ice arches. In particular, the tendency of the MEB and VP models to produce ice arches at different locations (upstream of the channel in the standard VP model, downstream of the channel in the MEB model) is investigated. Our findings will serve to determine the model components that can used to improve the ice arches simulated under realistic conditions in future work.

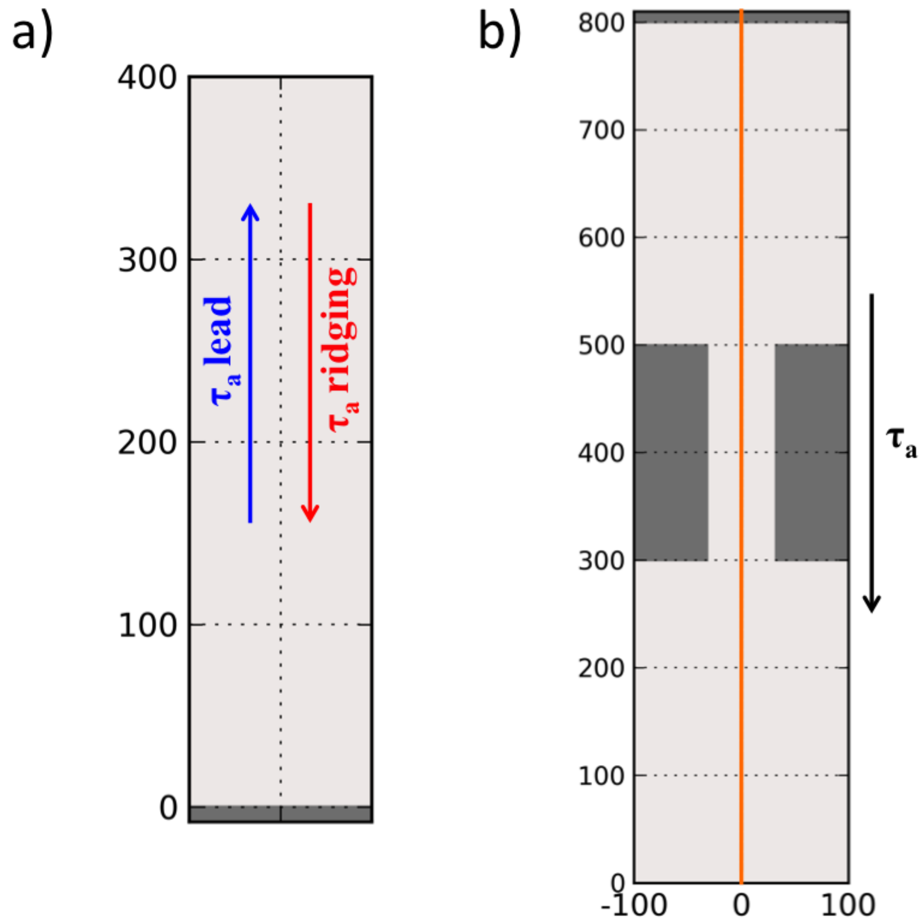

Figure 5.3: a) Schematic of the 1D lead opening and ridging experiment domain, which corresponds to 400x20 km piece of ice pulled from and pushed into a land boundary (Dirichlet conditions with u,v=0) by an external surface forcing. An open (Neumann, with du/dn, dv/dv=0) boundary is placed at the top, and the 1D conditions are created by using lateral periodic boundaries. (b) Domain used in the ice bridge simulations, with a solid (Dirichlet) wall to the north, open (Neumann) boundary to the south and periodic boundaries to the East and West. A narrow channel (with 60 km width and 200 km length) is placed in the middle of the domain, with 300km large basin on either sides.

5.4 Results

5.4.1 1D lead opening and ridging

We first perform the lead opening and ice ridging experiments with the ice fracture component turned off (d=d_{VP}=0), such that the ice is in the viscous or elastic-dominated regimes in the VP and MEB models respectively. The sea ice in this case corresponds to a slab of infinitely strong landfast ice in which onle small deformations are present.

Both models show very small landfast ice deformations that are symmetric between the lead opening and ridging experiments (Fig 5.4 and 5.5). In the VP model, the viscous creep response to the forcing is in agreement with results from [*Beatty and Holland*, 2010] and causes a total deformation of 0.520 mm at the land boundary after 5h of time integration when using the standard yield curve, and 0.151 mm when using the material-equivalent yield curve (Fig. 5.4c). These values are in close agreement to the analytical values (0.523 mm and 0.152 mm respectively, see Appendix section 5.7). Note that the deformations remain present after the forcing is removed (Fig. 5.4a) and have the potential of growing to non-negligible values over a seasonal time scale, even when using a smaller forcing (e.g. in the order of centimeters after days of cumulative forcing when using τ_a = 0.1 n m s^{-2}, which corresponds to a wind of 28.8 km h^{-1}).

In the MEB model, the landfast ice sees an immediate elastic response with propagating elastic waves superposed on a smaller viscous creep (Fig. 5.5a). The model resolves well the elastic waves excited by the step increase in forcing and their dissipation over the viscous time-scale λ (∼1 day, Fig. 5.5b). The reversible elastic deformations return to zero when the forcing is removed, leaving only the viscous deformations in the long term. Reducing the elastic deformation by increasing Y without changing the viscous creep η_0 (e.g. dashed curves in Fig. 5.5 where $Y = 10^{14}$ N m^{-2} and $\lambda = 1.0$ s are used) isolates well the viscous

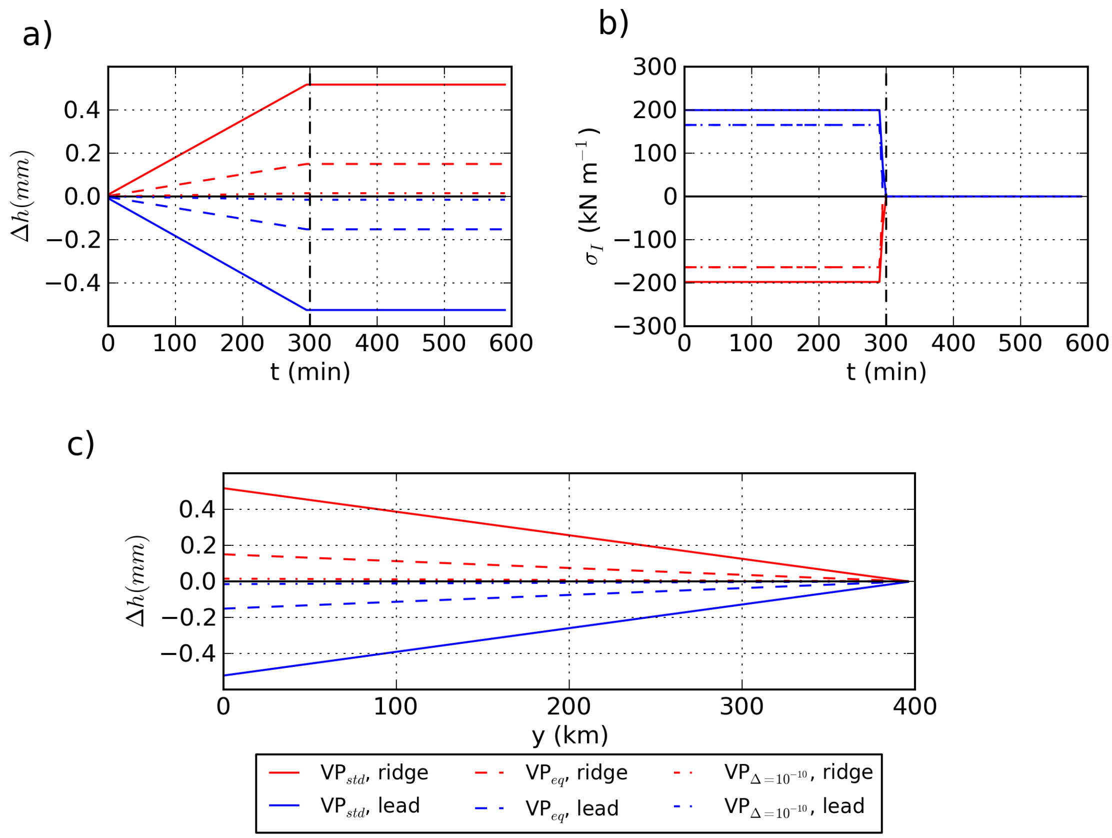

Figure 5.4: Ice deformations and stresses in the lead opening (blue curves) and ridging (red curves) experiments, in the VP simulations without the fracture component (d_{VP}=0 and $\Delta = \Delta_{min}$ at all times). Solid lines corresponds to simulations made with the standard yield parameters, dashed lines indicate the simulations made with equivalent ellipse yield parameters and dash-dotted lines indicate the simulations performed with a reduced creep ($\Delta = 10^{-10}$ s). a) Evolution of the sea ice deformation at the land boundary. b) Evolution of the normal internal stress at the land boundary. c) Ice deformation in the entire domain after 5h of time integration. The dashed black line indicate the moment when the surface forcing is removed.

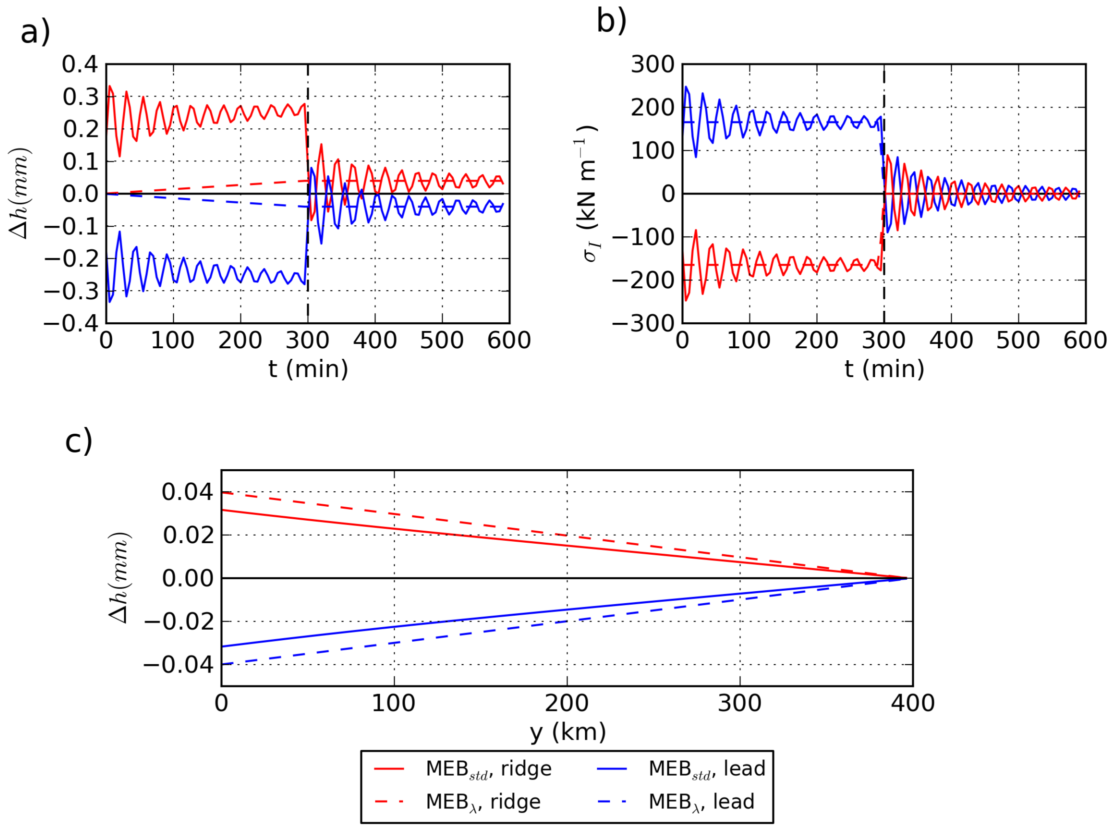

Figure 5.5: Ice deformations and stresses in the lead opening (blue curves) and ridging (red curves) experiments, in the MEB simulations without the fracture component (d=0 at all times). Solid lines corresponds to simulations made with the standard (Y,λ) parameters, and dashed lines indicate the simulations made with negligible elastic component ($Y = 10^{14}$ kN m^{-2},λ=1s). a) Evolution of the sea ice deformation at the land boundary. b) Evolution of the normal internal stress at the land boundary. c) Ice deformation in the entire domain after 5h of time integration. The dashed black line indicate the moment when the surface forcing is removed.

deformations that are combined with the elastic wave response in the control simulation. The total viscous-creep deformation at the land boundary after 5h of time integration is 0.0399 mm in the MEB simulations (Fig. 5.4c), in agreement with the theoretical value of 0.0400 mm (see Appendix 5.8). The difference in the deformation between the control simulation and the viscous-creep-dominated experiment in Fig. 5.4c corresponds to the remaining Elastic deformations that are not yet fully dissipated by the end of the simulation. Note that the total viscous creep deformation in the MEB simulations is one order of magnitude smaller than in the VP model with due to the larger viscosity ($\eta_0 = 10^{14}$ Ns m^{-2}, compare to ζ_{max}=(P+T)/2Δ_{min}=1.91x10^{13} Ns m^{-2} in the VP model with the material-equivalent ellipse).

The simulations are repeated in a second experiment with the fracture component included. Both the VP and MEB rheologies produce large and localised deformations close to the boundary where d and $d_{\mathrm{VP}} \sim 1$ (see Fig 5.6 for the VP model and 5.7 for the MEB model). This indicates that the elastic waves excited by the step increase in forcing in the MEB rheology do not significantly impact the fracture development in this simple 1D experiment. The material response is asymmetric between the lead opening and ridging experiments due to the weak tensile and strong compressive strength of sea ice. In the lead opening experiment (blue curves in Fig. 5.6 and 5.7), the fractures decrease the contact with the land boundary and the ice accelerates away from the coast, reaching free drift (see zero internal stress in Fig. 5.6d and 5.6d). The rate of lead opening is thus not sensitive to the rheology, rather being determined by the velocity of the downstream ice. In the ridging experiments (red curves in 5.6 and 5.7), the increasing ice thickness in the fractures increases the stress load locally, causing the ridging area to gradually progress upstream over time [see also *Williams et al.*, 2017].

In the VP simulations, a strong but constant gradient in ice velocity develops within the fracture, leading to the a linear increase in ice thickness in accord with results from [*Williams et al.*, 2017]. Note that the the decrease in d_{VP} from the fractures to the boundary in Fig 5.7a is associated with the use of replacement pressure in the linear-viscous regime [$P_p = P_r = 2\Delta\zeta_{max}$, or $\zeta = P_r/2\Delta_{min}$, *Hibler and Ip*, 1995]. In the standard simulation, the ice velocity reaches 0.3104 m s^{-1} upstream of the fracture and the ridging is spread over a width of ∼35 km, with a maximum thickness of 1.433 m at the solid boundary after 5h of time-integration. Using the material-equivalent ellipse presents similar d_{VP} but smaller deformation rates that are spread over a wider area, reducing the slope in ice thickness (Fig. 5.6c). In this simulation, the ice velocity reaches 0.257 m s^{-1} upstream of the fracture and the ridging is spread over a width of ∼45 km with a maximum thickness of 1.24 m at the solid boundary after 5h of time-integration.

In the MEB model, no ridging occurs in the control simulation with standard model parameters. Ridging occurs if a compression cut-off is used with the Mohr-Coulomb yield curve, in which case, the fractures are similar to those produced by the VP model, except for their concave shape (Fig. 5.7c). After 5h of time-integration, the ice velocity reached 0.27 m s^{-1} upstream of the fracture and the ridge is spread over a width of ∼35 km with a maximum thickness of 1.56 m at the solid boundary.

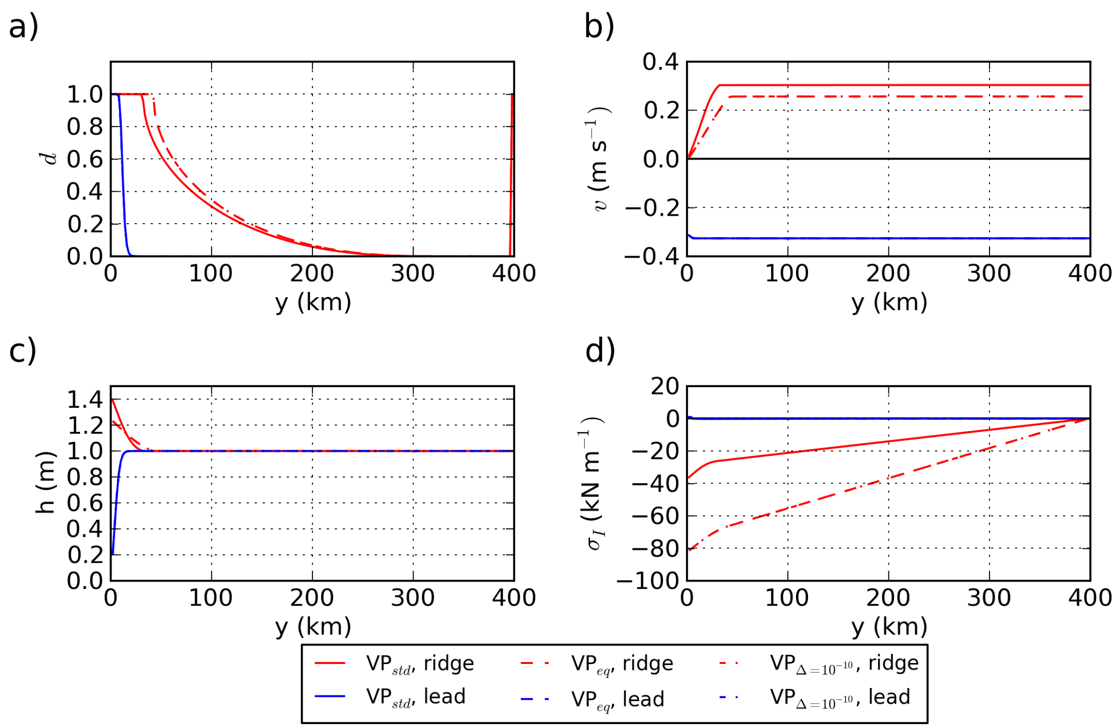

Figure 5.6: Ice damage (a), velocity (b), thickness (c), and normal internal stresses (d) in the lead opening (blue curves) and ridging (red curves) experiments made with the VP rheology, including the fracture component. Solid lines corresponds to simulations made with the standard yield parameters, dashed lines indicate the simulations made with equivalent ellipse yield parameters and dash-dotted lines indicate the simulations performed with a reduced creep ($\Delta = 10^{-10}$ s).

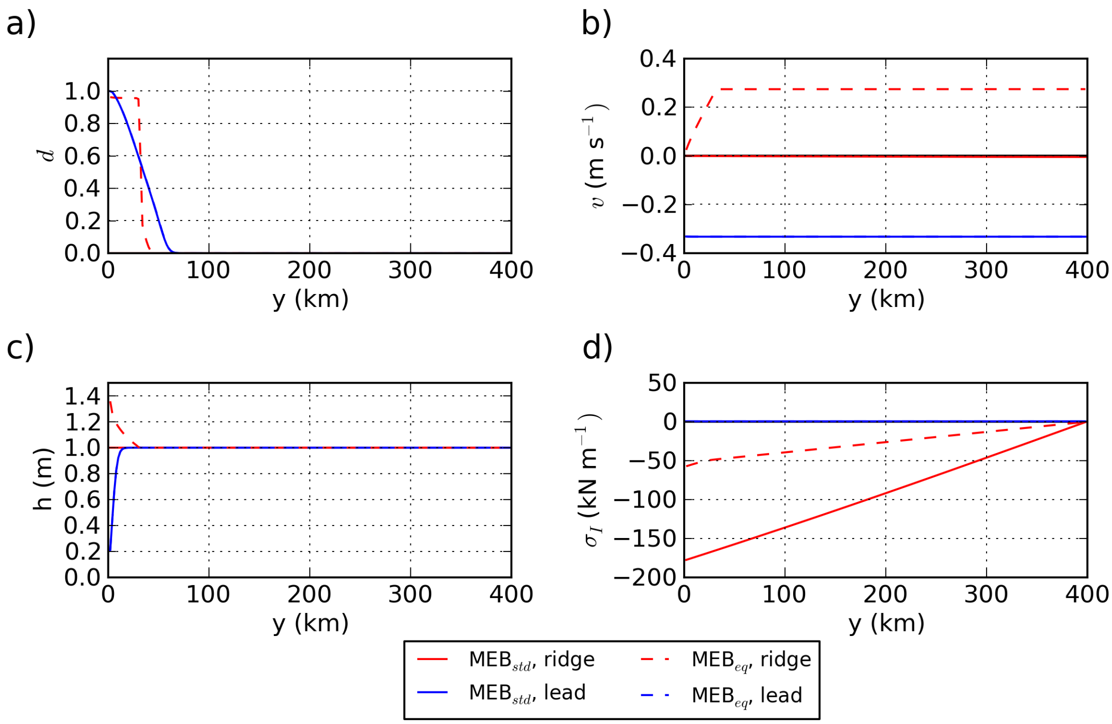

Figure 5.7: Ice damage (a), velocity (b), thickness (c), and normal internal stresses (d) in the lead opening (blue curves) and ridging (red curves) experiments made with the MEB rheology, including the fracture component. Solid lines corresponds to simulations made with the standard Mohr-Coulomb yield curve, and dashed lines indicate the simulations made with the compressive strength criterion.

5.4.2 Ice arch experiments

The ice arch experiments investigate the longer-term deformations simulated by the rheologies in a 2-D context. As in the 1D simulations, results show that using the different rheology and yield curves influences the ridging behaviour but has little influence on the lead opening forming a downstream ice arch. All simulations show an ice arch downstream of the channel (left panels in Fig. 5.8 and 5.9), until the landfast ice within the channels collapses [*Plante et al.*, 2020]. The different ridging behaviour however causes important differences between the simulations following the collapse of the ice bridge, in and upstream of the channel.

In the VP model simulation with the standard yield curve (5.8a), the ridges first develop adjacent to the upstream island coasts and progressively expands northward but never leads to a clean linear shear failure at some angle from the coast, as seen in simple uniaxial loading experiments [*Ringeisen et al.*, 2019]. Instead, a curve-shaped ridge form as the ice continues to flow in a funnel and through the channel, without forming ice arches. Using the material-equivalent ellipse causes changes in ridging that are consistent with results from the 1D experiment, with smaller ice thickness, the increased compressive strength causes a reduction of the ridging area upstream of the channel with smaller deformation rates. As the thickness increases, the shear strength of ice becomes sufficient to sustain the forcing upstream of the channel, where an ice arch forms after 6 days of simulation (Fig. 5.8b, right pannel), in accord with *Dumont et al.* [2008].

In the MEB model simulation with the standard Mohr-Coulomb yield criterion (i.e. without the compression cut-off), the ridging is localised around two lines of shear fractures that are oriented at 45° from the y-axis (5.9a). The ice upstream then flows through the resulting funnel. This is more in line with observations except for the fracture angle that is too large. In this simulation, there is less ridging due to the infinite compressive (and

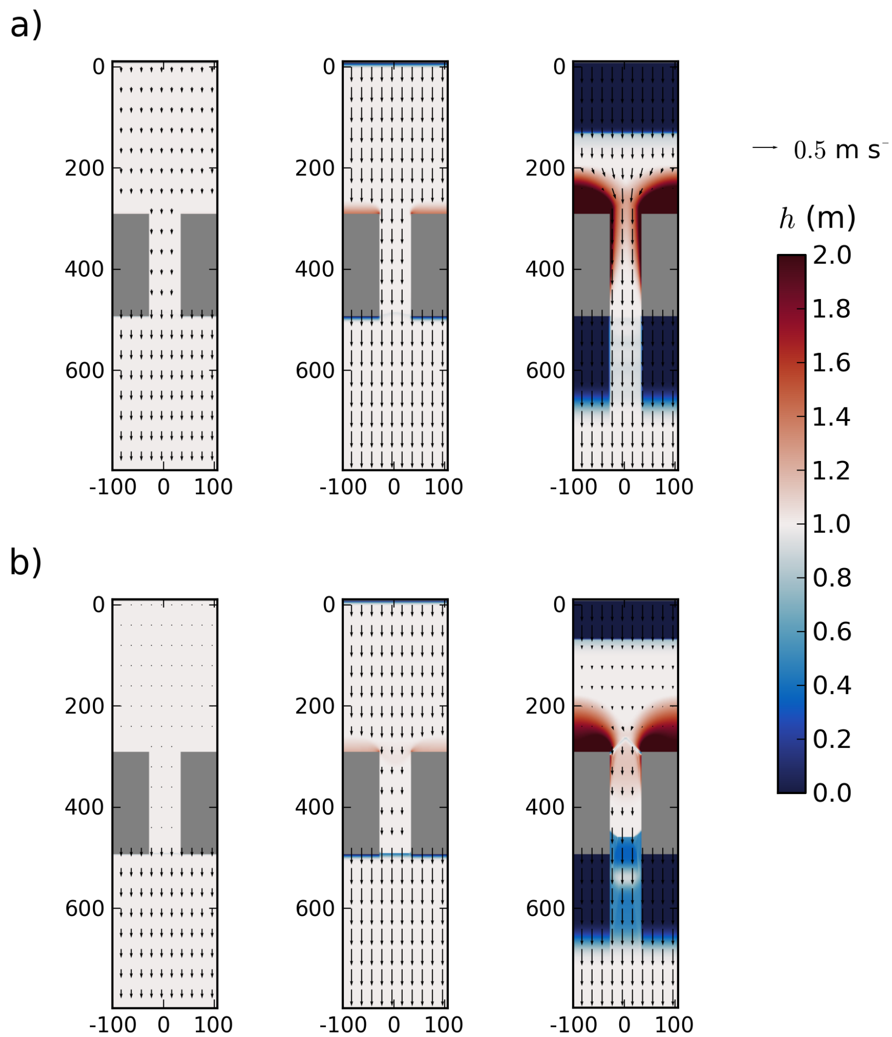

Figure 5.8: Ice thickness (color) and drift (arrows) at different stages of the ice arch simulations using the VP rheology. Left: after 50 minutes, centre: after 5 hours, right: after 7 days. a) Using the VP rheology and the standard ellipse. b) using the VP rheology and the equivalent ellipse with larger material strength

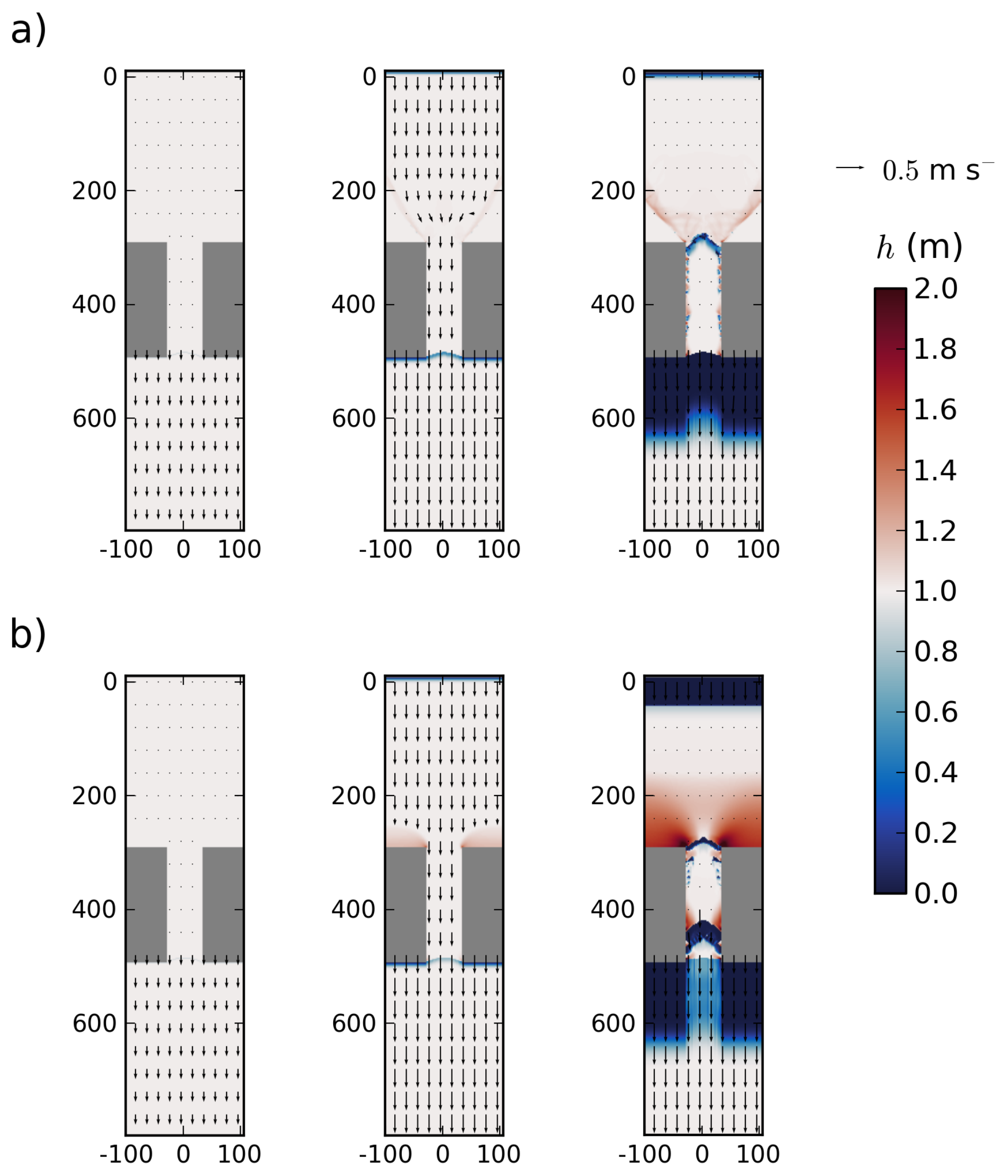

Figure 5.9: Ice thickness (color) and drift (arrows) at different stages of the ice arch simulations using the MEB rheology. Left: after 50 minutes, centre: after 5 hours, right: after 7 days. a) Using the standard Mohr-Coulomb criterion. b) Using the Mohr-Coulomb criterion with the compressive cut-off.

associated shear) strength. The ridging occurs as part of the post-fracture viscous deformation in the shear fractures [*Plante and Tremblay*, 2020], and stops over the damage healing time-scale once the shear strength becomes sufficient to sustain the forcing upstream of the channel. In this case, the ice arch forms after 2 days of simulation. Note that the ice arch downstream of the channel also re-forms, as post-fracture ridging along the channel coast sufficiently increased the ice strength to sustain the arch after 4 days of simulation. When the yield criterion is used with the compressive strength cut-off, the sea ice deformations are closer to those from the VP simulations (see Fig. 5.9b). The ridging occurs directly upstream of the islands and continues over a longer period during which the ice drifts in the upstream basin. This delays the formation of the ice arch upstream of the channel, which forms after 3 days of simulation. Note the use of a compressive strength cut-off does not prevent the post-fracture ridging occurring along the channel sides, such that other ice arch also form downstream of the channel.

In all simulations, the formation of an ice arch upstream of the channel occurs when the ice is sufficiently strong in compression (and shear) to sustain the forcing. This allows tension to develop on the condition that ice drift continues in the channel downstream. This is seen in our simulation by the development of a positive gradient in ice velocity upstream of the channel entrance, also associated with the building of tension (red curves in Fig. 5.10). This also happens when using the VP model with the standard ellipse but to a much lesser extent, as ridging (with ice drift upstream) continuously occurs throughout the simulation (blue curves in Fig. 5.10).

Repeating the simulations with different Δ_{min} values does not result in differences in the fracture and deformations in the ice arch simulations (see superposed curves in Fig 5.11), contrary to results report by *Olason* [2016]. We hypothesize that the reported increased landfast ice stability when using a large maximum viscosity results from the difficulty of the model to find a converged solution, leading to an increased heterogeneity that helps the formation ice arches downstream of channels, in a manner similar to the post-deformation deformations seen in our results with the MEB rheology.

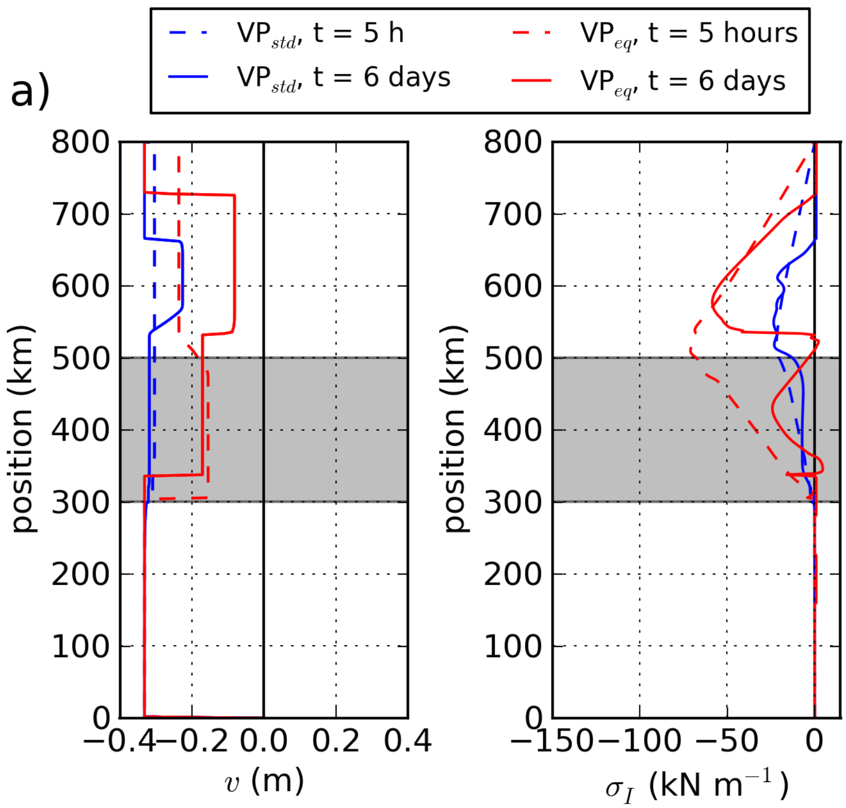

Figure 5.10: Ice velocity and internal normal stress in the ice bridge experiments along the transect running in the middle of the channel (see orange line in Fig. 5.3b), after 5 hours (dashed lines) and 6 days (solid lines) of time integration, in simulations using the VP rheology. Blue lines represent simulations ran with the standard yield curve. Red lines represent simulations ran with the material-equivalent yield curve.

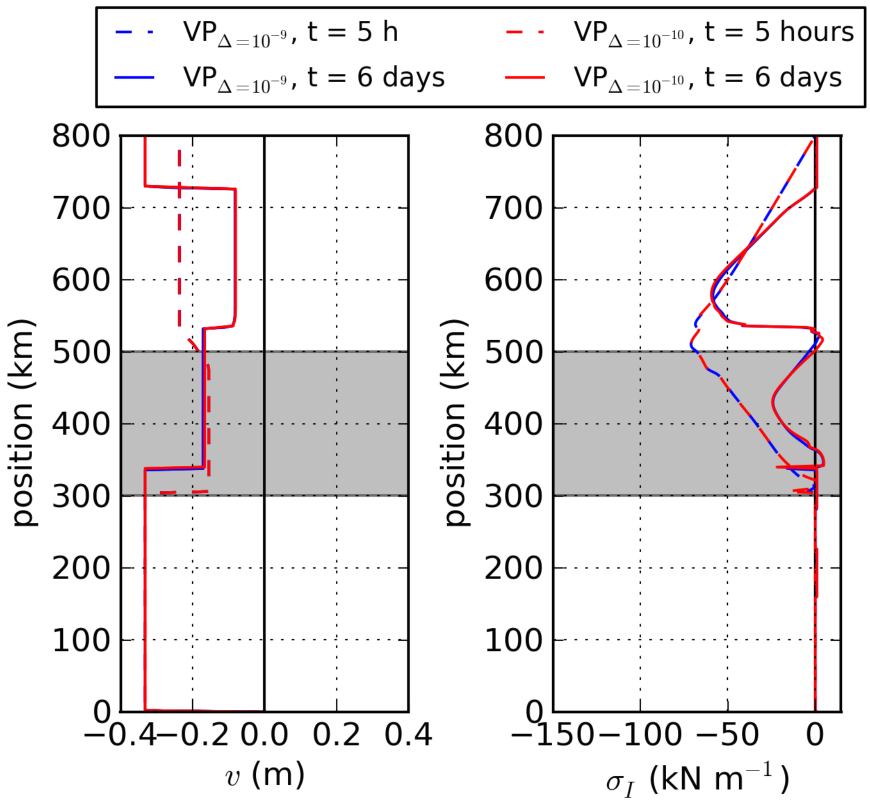

Figure 5.11: Same as Fig. 5.10 but in VP simulation using the standard ellipse and different values for Δ_{min}: the standard $\Delta_{min} = 10^{-9}$ s (blue curves) and a reduced $\Delta_{min} = 10^{-10}$ s (red curves). The curves are mostly superposed, as the change in Δ_{min} did not significantly affect the solutions.

5.5 Discussion

Both the VP and MEB rheology efficiently produce two distinct deformation regimes that create discontinuities in ice deformations. Prior to or outside of the fractures, they simulate small but time-dependent viscous creep deformations that represent well the solid character of sea ice. The transition to large deformations is also similar in both rheologies, representing the fracture as a material discontinuity (or damage) in the elastic stiffness and viscous coefficients, and allowing for large local deformations. The differences between the simulations are mostly related to the development of these large deformation rates in the fractures over time. In the VP model, the use of a plastic flow rule and the absence of damage memory causes the large deformation rates to be synchronous with fracturing, and produces deformations that are in overall smoother than in the MEB model. In the MEB rheology, the large deformations occur post-fracture based on viscous coefficients that depend non-linearly on the damage, resulting in the building of non-linearity and larger local variations in the deformations.

Despite these differences, the location of the fractures are similar between the VP and MEB simulations when using material-equivalent yield curves, and all produce ice arches upstream of the channel. The most important difference between the simulations is the formation of shear fractures when using the MEB model with infinite compressive (and shear) strength. Note however that shear fracture lines are simulated by the VP rheology in uniaxial compression experiments [*Ringeisen et al.*, 2019]. That fact that these shear fracture lines are not formed in the ice arch simulations is attributed to the fact that the land boundary corners corresponds to lesser shear stress concentrators for the surrounding ice, than the corners of the ice sample in the uniaxial compression experiment. Also, the fact that the shear fractures do form in the MEB model when used with infinite compressive strength but not when using the compression cut-off suggests that they could also be simulated by the VP model by using a yield curve with very large compressive strength (P^*) and ellipse ratio (e). This will be tested in future simulations.

Based on our results, the development of the ice arch upstream of a channel presents two requirements. First, the material strength (compressive and shear) of the ice upstream of the channel must be sufficient to sustain the forcing load. In our simulations, this was achieved over time by the ridging of ice, increasing the ice strength with ice thickness. This can also be achieved by reducing the surface forcing following the collapse of landfast ice in the channel downstream. Second, the ice must be in drift in the channel downstream for the arching tensile fracture to develop. This condition was naturally met in *Dumont et al.* [2008] by setting the channel as ice free in the initial conditions. In the MEB model, this condition is only temporarily met as post-fracture deformations occur within the channel and creates ridges that are large enough for the formation of other ice arches inside the channel. This occurred in all our MEB simulations independently of the use of the compression cut-off and despite the use of a very large forcing. This explains the tendency of the ice arches to be located downstream of the channels in the MEB model, contrary to the observed locations.

Note that two listed conditions call for a weak material cohesion (for ice drift to occur in the channel) and large compressive strength (for the development of shear fractures and ice arches upstream of the channel). This combination is naturally present using the Mohr-Coulomb criterion but is more challenging using an ellipse yield curve in which the compressive and shear strength of are co-dependent [*Bouchat and Tremblay*, 2017]. Decreasing the shear strength and increasing the compressive strength is also contrary to the recommendations of [*Bouchat and Tremblay*, 2017] for the accurate representation of ice deformation statistics in the Arctic (i.e. reducing the compressive strength or increasing the shear strength). Note however that in realistic simulations, the two conditions are often naturally met by the presence of stronger surface forcings in the channels. For instance, many recurrent ice arches in the CAA are located upstream of channels where the tidal forcing is especially strong [*Hannah et al.*, 2009].

5.6 Conclusion

The influence of the rheology on the simulated sea ice deformations is analysed in the context ideal landfast ice simulations that are run using the VP and MEB rheologies, which are both implemented in the McGill Sea Ice Model. The deformations simulated by the two rheologies are first compared in 1D lead opening and ridging experiments. We then revisit the ideal ice bridge simulations of *Plante et al.* [2020] in long term (10-days) simulations to look at the formation of ice arches in a narrow channel.

Results show that the differences between the rheologies are mostly related to the ridging occurring in the fractures. Under compression, the ridging is affected by the dependency of the sea ice viscosity on the material damage, which causes non-linear deformation shapes in the MEB model but smoother ice deformations in the VP model. We show that the formation of ice arches upstream of the channel depends on two criteria: the compressive and shear strength must be superior to the internal stresses upstream of the channel, and the ice in the channel downstream must be free to drift. This is a limitation when using the standard VP rheology given its small compressive strength. In the MEB model, the post-fracture deformations occurring in the channel produces ridges with sufficient strength to sustain a large forcing, leading to a tendancy to the stable ice arches to be located downstream of the channels, contrary to observations. We also demonstrate that the maximum viscosity have no impact on the production of fractures and the formation of the ice arches.

5.7 Appendix A: Analytic creep deformation in the VP model

We consider a 1D ice cover in the y-direction with an open boundary at the top (dv/dy=0) and land boundary (v=0) at the bottom, forced with a constant forcing τ_y in y-direction. Assuming that the ice is in the viscous regime in the entire domain [*Beatty and Holland*, 2010], the changes in ice thickness resulting from the viscous creep in the VP model can be approximated using the 1D steady-state version of the momentum (Eq. 5.1) and the VP constitutive (Eq. 5.16) equations. That is, we have:

$$\frac{\partial \sigma_{yy}}{\partial y} + \tau_y = 0, \tag{5.26}$$

with,

$$\sigma_{yy} = (\zeta + \eta)\dot{\epsilon}_{yy} + \frac{P_p}{2}, \tag{5.27}$$

where σ_{yy} is the normal stress in the y-direction, $\dot{\epsilon}_{yy}$ is the normal strain rate in the y-direction, and where we have neglected the $\partial/\partial x$ and the $\partial/\partial t$ terms. Combining Eq. 5.26 with 5.27, we get:

$$(\zeta + \eta)\frac{\partial \dot{\epsilon}_{yy}}{\partial y} + \frac{1}{2}\frac{\partial P_p}{\partial y} + \tau_y = 0. \tag{5.28}$$

Integrating to a distance L from the open boundary where $\dot{\epsilon}_{yy} = 0$, and assuming that the ice strength is equal in the domain, we approximate the viscous deformation rate as:

$$\dot{\epsilon}_{yy}|_L = -\frac{\tau_y L}{(\zeta + \eta)} = -\frac{2\tau_y L \Delta_{min}}{(e^{-2} + 1)(P + T)} \tag{5.29}$$

where $\dot{\epsilon}_{yy}|_L$ is the strain rate at distance L from the open boundary and where the viscous coefficient were expended using Eq. 5.18.

The change in ice thickness can then be determined by integrating Eq. 5.29 over a time Δt:

$$\Delta h|_L = -\frac{2\tau_y L \Delta_{min} \Delta t}{(e^{-2}+1)(P+T)} \tag{5.30}$$

5.8 Appendix B: Analytic creep deformation in the MEB model

We repeat the derivation above to determine the change in ice thickness resulting from the viscous creep in the MEB model, using the 1D steady-state version of the momentum (Eq. 5.1) and MEB constitutive (Eq. 5.5) equations. That is, we have:

$$\frac{\partial \sigma_{yy}}{\partial y} + \tau_y = 0, \tag{5.31}$$

with,

$$\sigma_{yy} = \frac{E}{\lambda(1-\nu^2)}\dot{\epsilon}_{yy}, \tag{5.32}$$

where σ_{yy} is the normal stress in the y-direction, $\dot{\epsilon}_{yy}$ is the normal strain rate in the y-direction, and where we have neglected the $\partial/\partial x$ and the $\partial/\partial t$ terms. Combining Eq. 5.31 with 5.32, we get:

$$\frac{E}{\lambda(1-\nu^2)}\frac{\partial \dot{\epsilon}_{yy}}{\partial y} + \tau_y = 0. \tag{5.33}$$

Integrating to a distance L from the open boundary, where $\dot{\epsilon}_{yy} = 0$, we approximate the viscous deformation rate as:

$$\dot{\epsilon}_{yy}|_L = -\frac{\tau_y L \lambda(1-\nu^2)}{E} \tag{5.34}$$

where $\dot{\epsilon}_{yy}|_L$ is the strain rate at distance L from the open boundary.

The change in ice thickness can then be determined by integrating Eq. 5.34 over a time Δt:

$$\Delta h|_L = -\frac{\tau_y L \lambda \Delta t (1 - \nu^2)}{E} \tag{5.35}$$

Chapter 6

Conclusion

6.1 Summary

In this thesis, we aimed at improving the representation of landfast ice in sea-ice models by determining the role of a damage parameterization on the simulated ice fracture and on the formation of landfast ice arches. We produced ideal simulations with the Maxwell Elasto-Brittle model to identify the model components and strength parameters that are needed to better simulate the landfast ice cover. We described the growth of residual errors in the standard damage parameterization, which we improved by developing a generalized stress correction scheme. We compared the simulated deformations in the MEB and the Viscous-Plastic (VP) models to study the influence of fracture parameterizations on the simulated sea-ice deformations both in and about fracture lines. These are necessary steps not only to improve the representation of landfast ice in sea-ice models but also to guide future model developments in the context of the increasing demand for high-resolution sea-ice forecasts.

In Chapter 2, the formation of ice arches in the Arctic is documented using ice charts from the National Ice Center (NIC) and satellite observations. In particular, brightness temperature imagery is used to identify the role of ice arching in the formation of the landfast ice cover across the Arctic. We find that the large landfast ice cover are formed via the formation of ice arches between offshore areas where ice is locally grounded. We find that ice grounding occurs early in the freezing season over shallow shoals, which later provide anchor points from which ice arches can form and sustain the landfast ice. We demonstrate that the region of large landfast ice variability corresponds to large ice arches that easily collapse under a strong surface forcing. These observations suggest that the current grounding parameterization underestimates grounding early in the season, overestimates it in the winter and underestimates their persistence into the melt season.

In Chapter 3, we perform ideal ice arch simulations using the MEB rheology, implemented onto a Finite Difference framework. As this is the first implementation of this rheology and the damage parameterization on the framework most commonly used in climate or coupled models, we also present our numerical implementation in the McGill Sea Ice Model version 5. This provides a base for future implementations in community-shared sea-ice models such as CICE or MITgcm. In the idealized ice bridge simulations, we confirmed the tendency of the MEB rheology to form ice arches downstream of a channel in short-term simulations. The ice arches sustain a stable landfast ice bridge in the channel, with size that best corresponds to observations when using a cohesion in the range of 5-10 kN m^{-2}. This provides a useful bound on the material strength parameters used in a Mohr-Coulomb yield criterion. We show that the ice bridge collapse is associated to the formation of compressive fracture lines upstream of the channel, with orientations that do not correspond to granular theories. We also find that ridging generates a problematic growth of the residual model errors, caused by the stress correction scheme in the standard damage parameterization.

In Chapter 4, we developed a generalised stress correction scheme that reduces the growth of the residual errors in the damage parameterization. The generalized stress correction scheme uses a decohesion stress tensor to bring the super-critical stress back to the yield curve following any stress correction path. We showed that using a stress correction path that is normal to the yield curve improves both the growth of the residual errors and the orientation of the simulated lines of fracture. In uniaxial loading tests, we found that the decohesion stress tensor influences the development of fractures in the MEB model but not the deformations along the fractures. The large deformation rates simulated by the MEB rheology mostly occur post-fracture and dissociated from the development of damage, an important difference with the classical VP rheology in which large deformation only occurs simultaneously with fracturing,.

Finally in Chapter 5, we used the VP model and the generalized MEB model, both implemented on the same numerical platform, to determine the influence of the different fracture physics on the simulated sea-ice deformations. In 1D simulations, we showed that both model produce small viscous creep deformations in landfast ice and present a similar transition to the large deformations associated with fractures. The large deformations however differ between the models, the normal flow rule of the VP model producing linear ridges ans smooth deformations in the fractures, while the non-linear post-fracture viscous deformation causes non-linear concave ridges and larger local variations in the deformations. We also used the VP and generalized MEB models to performed ice bridge simulations in the context of longer-term post-fracture simulations. We found that both models produce similar ice arches upstream of the channel when they use equivalent yield envelopes. The upstream ice arch forms when the ice strength – which increases with the ice thickness – is superior to the compression upstream of the channel, while the ice is drifting within the channel downstream. The tendency of the MEB model to produce ice arches downstream in the channel is attributed to post-fracture deformations occurring within the channel, create ridges with sufficient strength for the formation of other arches. We also showed that the fractures and deformations in our simulations are not sensitive to the VP model maximum viscosity defining the transition between viscous and plastic deformations, contrary to what was previously reported.

6.2 Future Work

In this thesis, we showed that the growth of residual errors is reduced but not removed when using the generalized stress correction scheme. The remaining growth is attributed to the non-linear dependency of the Maxwell viscosity term on the damage parameter, such that the integrated errors largely influence the post-fracture deformations. This issue can be resolved by modifying the viscosity term.

We also demonstrated in this thesis that the inclusion of a decohesion stress tensor does not influence the post-fracture deformations. The next step is to determine whether the sea-ice deformation statistics in pan-Arctic simulations are also non-sensitive to the use of the generalized stress correction scheme. The deformation statistics obtained with the generalised MEB rheology for pan-Arctic simulations will be compared to those reported in [*Bouchat and Tremblay*, 2020] to determine the extent at which the reported inter-model differences are explained by the different numerical implementations. The orientation of the ice fracture in the pan-Arctic simulations could also be investigated to determine if they capture well the observed statistics and determine the correction path that best represent them. This will be an important step to determine the numerical components that influences the sea ice deformations and guide future model developments.

The ice arch observations presented in this thesis can also be used to define the model parameters that produce the right amount of ice arching and ice grounding in different stages of the landfast ice formation and break-up. Realistic Laptev sea simulations that include the ice grounding parameterization of [*Lemieux et al.*, 2015] will be run to reproduce specific events in the landfast ice seasonal cycle, and the grounding and ice strength parameter will be tuned to produce the right combination of ice grounding and ice arching as seen in the MODIS observations. This will give a seasonal evolution of the tuned parameters can be used to redefine their parameterized relationship with ice thickness, and ultimately improve the representation of the landfast ice onset and break-up in dynamical sea-ice models.

Finally, while the current thesis focused sea ice dynamics and its impact on the simulated landfast ice, the break up of landfast ice in the melt season is largely dependent on the sea ice thermodynamics. Much remains to be determined in the influence of small-scale features in the landfast ice break up in spring, such as the inter-play between the winter dynamics (which preconditions the landfast ice with local weaknesses) and thermodynamics factors such as the snow cover and melt ponds. To better understand how to parameterized the landfast ice fracture in high-resolution models, field observations could be collected to observe the dynamic preconditioning of landfast ice, their impact on the local internal stresses and thermodynamics, such that we can better define the large scale mechanical properties of landfast ice throughout the melt season.

Bibliography

Aksenov, Y., E. E. Popova, A. Yool, A. J. G. Nurser, T. D. Williams, L. Bertino, and J. Bergh (2017), On the future navigability of Arctic sea routes : High-resolution projections of the Arctic Ocean and sea ice, *Marine Policy*, *75*, 300–317, doi:10.1016/j.marpol.2015.12.027.

Amitrano, D., and A. Helmstetter (2006), Brittle creep, damage and time to failure in rocks, *Journal of Geophysical Research : Solid Earth*, *111*, B11,201, doi:10.1029/2005JB004252.

Amitrano, D., J.-R. Grasso, and D. Hantz (1999), From diffuse to localised damage through elastic interaction, *Geophysical Research Letters*, *26*, 2109–2112.

Arthur, J. R. F., T. Dunstan, Q. A. J. L. Al-Ani, and A. Assadi (1977), Plastic deformation and failure in granular media, *Géotechnique*, *27*(1), 53–74, doi:10.1680/geot.1977.27.1.53.

Balendran, B., and S. Nemat-Nasser (1993), DOUBLE SLIDING MODEL FOR CYCLIC MATERIALS , EFFECTS DEFORMATION INCLUDING OF GRANULAR, *J. Mech. Phys. Solids*, *41*(3).

Barber, D., and R. Massom (2007), Chapter 1 The Role of Sea Ice in Arctic and Antarctic Polynyas, in *Polynyas: Windows to the World*, *Elsevier Oceanography Series*, vol. 74, edited by W. Smith and D. Barber, pp. 1 – 54, Elsevier, doi:https://doi.org/10.1016/S0422-9894(06)74001-6.

Bardet, J. (1991), Orientation of shear bands in frictional soils, *Journal of Engineering Mechanics - ASCE*, *117*(7), 1466–1484, doi:10.1061/(ASCE)0733-9399(1991)117:7(1466).

Bareiss, J., and K. Gorgen (2005), Spatial and temporal variability of sea ice in the Laptev Sea: Analyses and review of satellite passive-microwave data and model results, 1979 to 2002, *Global and Planetary Change*, *48*(1-3), 28–54, doi:10.1016/j.gloplacha.2004.12.004.

Bareiss, J., H. Eicken, A. Helbig, and T. Martin (1999), Impact of river discharge and regional climatology on the decay of sea ice in the Laptev sea during spring and early summer, *Arctic, Antarctic, and Alpine Research*, *31*(3), 214–229.

Barnes, P. W., D. M. Rearic, and E. Reimnitz (1984), Ice gouging characteristics and processes, in *The Alaskan Beaufort Sea Ecosystem and Environments*, edited by P. Barnes, D. Schell, and E. Reimnitz, pp. 185–212, Academic Press London, UK.

Barry, R., R. Moritz, and J. Rogers (1979), The fast ice regimes of the Beaufort and Chukchi Sea coasts, Alaska, *Cold Regions Science and Technology*, *1*(2), 129–152, doi:10.1016/0165-232X(79)90006-5.

Beatty, C. K., and D. M. Holland (2010), Modeling Landfast Sea Ice by Adding Tensile Strength, *American Meteorological Society*, *40*, 185–198, doi:10.1175/2009JPO4105.1.

Bouchat, A., and B. Tremblay (2017), Using sea-ice deformation fields to constrain the mechanical strength parameters of geophysical sea ice, *Journal of Geophysical Research: Oceans*, *122*(7), 5802–5825, doi:10.1002/2017JC013020.

Bouchat, A., and B. Tremblay (2020), Scaling and statistical properties of sea-ice deformation fields from models participating in the FAMOS Sea-Ice Rheology Experiment, *To be submitted to JGR*.

Bouillon, S., and P. Rampal (2015), Presentation of the dynamical core of neXtSIM, a new sea ice model, *Ocean Modelling*, *91*, 23–37, doi:10.1016/j.ocemod.2015.04.005.

Carmack, E. C., and R. W. Macdonald (2002), Oceanography of the Canadian Shelf of the Beaufort Sea : A Setting for Marine Life, *Arctic*, *55*(supplement 1), 29–45.

Carrier, A., J.-L. Got, A. Peltier, V. Ferrazzini, T. Staudacher, P. Kowalski, and P. Boissier (2015), A damage model for volcanic edifices: Implications for edifice strength, magma pressure, and eruptive processes, *Journal of Geophysical Research: Solid Earth*, *120*(1), 567–583, doi:10.1002/2014JB011485.

Coulomb, C. (1773), Test on the applications of the rules of maxima and minima to some problems of statics related to architecture, *Mem Math Phys*, *7*, 343–382.

Cowie, P. A., C. Vanneste, and D. Sornette (1993), Statistical physics model for the spatiotemporal evolution of faults, *Journal of Geophysical Research: Solid Earth*, *98*(B12), 21,809–21,821, doi:10.1029/93JB02223.

Damsgaard, A., A. Adcroft, and O. Sergienko (2018), Application of Discrete Element Methods to Approximate Sea Ice Dynamics, *Journal of Advances in Modeling Earth Systems*, *10*(9), 2228–2244, doi:10.1029/2018MS001299.

Dansereau, V., J. Weiss, P. Saramito, and P. Lattes (2016), A Maxwell elasto-brittle rheology for sea ice modelling, *The Cryosphere*, *10*, 1339–1359, doi:10.5194/tc-10-1339-2016.

Dansereau, V., J. Weiss, P. Saramito, P. Lattes, and E. Coche (2017), Ice bridges and ridges in the Maxwell-EB sea ice rheology, *The Cryosphere*, *11*, 2033–2058.

Dansereau, V., V. Démery, E. Berthier, J. Weiss, and L. Ponson (2019), Collective Damage Growth Controls Fault Orientation in Quasibrittle Compressive Failure, *Phys. Rev. Lett.*, *122*, 085,501, doi:10.1103/PhysRevLett.122.085501.

Dedrick, K., K. Partington, M. Van Woert, C. Bertoia, and D. Benner (2001), u . s . National / Naval Ice Center Digital Sea Ice Data and Climatology, *Canadian Journal of Remote Sensing*, *27*(5), 457–475, doi:10.1080/07038992.2001.10854887.

Dethleff, D., P. Loewe, and E. Kleine (1998), The Laptev Sea flaw lead — detailed investigation on ice formation and export during 1991/1992 winter season, *Cold Regions Science and Technology*, *27*, 225–243.

Divine, D. V., R. Korsnes, and A. P. Makshtas (2004), Temporal and spatial variation of shore-fast ice in the Kara Sea, *Continental Shelf Research*, *24*(15), 1717–1736, doi:10.1016/j.csr.2004.05.010.

Dmitrenko, I., K. Tyshko, S. Kirillov, H. Eicken, J. Holemann, and H. Kassens (2005), Impact of flaw polynyas on the hydrography of the Laptev Sea, *Global and Planetary Change*, *48*(1-3), 9–27, doi:10.1016/j.gloplacha.2004.12.016.

Dumont, D., Y. Gratton, and T. E. Arbetter (2008), Modeling the Dynamics of the North Water Polynya Ice Bridge, *Journal of Physical Oceanography*, *39*, 1448–1461, doi:10.1175/2008JPO3965.1.

Dumont, D., Y. Gratton, and T. E. Arbetter (2010), Modeling Wind-Driven Circulation and Landfast Ice-Edge Processes during Polynya Events in Northern Baffin Bay, *Journal of Physical Oceanography*, *40*, 1356–1372, doi:10.1175/2010JPO4292.1.

Eicken, H., I. Dmitrenko, K. Tyshko, a. Darovskikh, W. Dierking, U. Blahak, J. Groves, and H. Kassens (2005), Zonation of the Laptev Sea landfast ice cover and its importance in a frozen estuary, *Global and Planetary Change*, *48*(1-3), 55–83, doi:10.1016/j.gloplacha.2004.12.005.

Ernsdorf, T., D. Schröder, S. Adams, G. Heinemann, R. Timmermann, and S. Danilov (2011), Impact of atmospheric forcing data on simulations of the Laptev Sea polynya dynamics using the sea-ice ocean model FESOM, *Journal of Geophysical Research*, *116*(C12), C12,038, doi:10.1029/2010JC006725.

Galley, R. J., B. G. T. Else, S. E. L. Howell, J. V. Lukovich, and D. G. Barber (2012), Landfast Sea Ice Conditions in the Canadian Arctic : 1983 – 2009, *Arctic*, *65*(2), 133–144.

Girard, L., S. Bouillon, J. Weiss, D. Amitrano, T. Fichefet, and V. Legat (2011), A new modeling framework for sea-ice mechanics based on elasto-brittle rheology, *Annals of Glaciology*, *52*(57), 123–132, doi:10.3189/172756411795931499.

Haas, C., W. Dierking, T. Busche, and J. Hoelemann (2005), ENVISAT ASAR monitoring of pylynia processes and sea ice production in the Laptev sea, *Tech. rep.*, Alfred Wegener Institute.

Hannah, C. G., F. Dupont, and M. Dunphy (2009), Polynyas and Tidal Currents in the Canadian Arctic Archipelago, *Arctic*, *62*(1), 83–95, doi:10.14430/arctic115.

Hata, Y., and L. B. Tremblay (2015a), Anisotropic internal thermal stress in sea ice from the Canadian Arctic Archipelago, *Journal of Geophysical Research: Oceans*, *120*, 5457–5472, doi:10.1002/2015JC010819.Received.

Hata, Y., and L. B. Tremblay (2015b), A 1.5-D anisotropic sigma-coordinate thermal stress model of landlocked sea ice in the Canadian Arctic Archipelago, *Journal of Geophysical Research: Oceans*, *120*, 8251–8269, doi:10.1002/2015JC010820.Received.

Herman, A. (2016), Discrete-Element bonded-particle Sea Ice model DESIgn, version 1.3a – model description and implementation, *Geoscientific Model Development*, *9*(3), 1219–1241, doi:10.5194/gmd-9-1219-2016.

Hibler, W., J. Hutchings, and C. Ip (2006), Sea-ice arching and multiple flow States of Arctic pack ice, *Annals of Glaciology*, *44*, 339–344, doi:10.3189/172756406781811448.

Hibler, W. D. (1979), A dynamic thermodynamic sea ice model, *Journal of Physical Oceanography*, *9*(7), 815–846.

Hibler, W. D., and C. Ip (1995), The effect of sea ice rheology on Arctic buoy drift, *Ice mechanics, 1995: Presented at the 1995 Joint ASME Applied Mechanics and Materials Summer Meeting, Los Angeles, California, June 28-30, 1995*, *204*, 815–846.

Hibler III, W. D., and E. M. Schulson (2000), On modeling the anisotropic failure and flow of flawed sea ice, *Journal of Geophysical Research: Oceans*, *105*(C7), 17,105–17,120, doi:10.1029/2000JC900045.

Hunke, E. C. (2001), Viscous–Plastic Sea Ice Dynamics with the EVP Model: Linearization Issues, *Journal of Computational Physics*, *170*(1), 18 – 38, doi:https://doi.org/10.1006/jcph.2001.6710.

Hunke, E. C., and J. Dukowicz (1997), An Elastic – Viscous – Plastic Model for Sea Ice Dynamics, *Journal of Physical Oceanography*, *27*, 1849–1867.

Hutter, N., M. Losch, and D. Menemenlis (2018), Scaling Properties of Arctic Sea Ice Deformation in a High-Resolution Viscous-Plastic Sea Ice Model and in Satellite Observations, *Journal of Geophysical Research: Oceans*, *123*(1), 672–687, doi:10.1002/2017JC013119.

Hutter, N., L. Zampieri, and M. Losch (2019), Leads and ridges in Arctic sea ice from RGPS data and a new tracking algorithm, *The Cryosphere*, *13*(2), 627–645, doi:10.5194/tc-13-627-2019.

Hutter, N., A. Bouchat, F. Dupont, D. Dukhovskoy, N. Koldunov, Y. Lee, C. Lique, W. Maslowski, P. Myers, E. Olason, T. Rasmussen, B. Tremblay, and Q. Wang (2020), Leads and pressure ridges simulated by high-resolution sea-ice models within the FAMOS Sea Ice rheology experiments (SIREx), *To be submitted to JGR*.

Ip, C. F. (1993), Numerical investigation of different rheologies on sea-ice dynamics, *PhD thesis*, *1*, 242 pp.

Itkin, P., M. Losch, and R. Gerdes (2015), Landfast ice affects the stability of the Arctic halocline: Evidence from a numerical model, *Journal of Geophysical Research: Oceans*, *120*, 2622–2635, doi:10.1002/2014JC010353.Received.

Itkin, P., G. Spreen, S. M. Hvidegaard, H. Skourup, J. Wilkinson, S. Gerland, and M. A. Granskog (2018), Contribution of Deformation to Sea Ice Mass Balance: A Case Study From an N-ICE2015 Storm, *Geophysical Research Letters*, *45*(2), 789–796, doi:10.1002/2017GL076056.

Jakobsson, M., L. A. Mayer, B. Coakley, J. A. Dowdeswell, S. Forbes, B. Fridman, H. Hodnesdal, R. Noormets, R. Pedersen, M. Rebesco, H.-W. Schenke, Y. Z. A, D. Accettella, A. Armstrong, R. M. Anderson, P. Bienhoff, A. Camerlenghi, I. Church, M. Edwards, J. V. Gardner, J. K. Hall, B. Hell, O. B. Hestvik, Y. Kristoffersen, C. Marcussen, R. Mohammad, D. Mosher, S. V. Nghiem, M. T. Pedrosa, P. G. Travaglini, , and P. Weatherall (2012), The International Bathymetric Chart of the Arctic Ocean (IBCAO) Version 3.0, *Geophysical Research Letters*, doi:doi:10.1029/2012GL052219.

Johnson, M., A. Proshutinsky, Y. Aksenov, A. T. Nguyen, R. Lindsay, C. Haas, J. Zhang, N. Diansky, R. Kwok, W. Maslowski, S. Häkkinen, I. Ashik, and B. de Cuevas (2012), Evaluation of Arctic sea ice thickness simulated by Arctic Ocean Model Intercomparison Project models, *Journal of Geophysical Research*, *117*, C00D13, doi:10.1029/2011JC007257.

Jung, T., N. D. Gordon, P. Bauer, D. H. Bromwich, M. Chevallier, J. J. Day, J. Dawson, F. Doblas-Reyes, C. Fairall, H. F. Goessling, M. Holland, J. Inoue, T. Iversen, S. Klebe, P. Lemke, M. Losch, A. Makshtas, B. Mills, P. Nurmi, D. Perovich, P. Reid, I. A. Renfrew, G. Smith, G. Svensson, M. Tolstykh, and Q. Yang (2016), Advancing Polar Prediction Capabilities on Daily to Seasonal Time Scales, *Bulletin of the American Meteorological Society*, *97*(9), 1631–1647, doi:10.1175/BAMS-D-14-00246.1.

Karimi, K., and J.-L. Barrat (2018), Correlation and shear bands in a plastically deformed granular medium, *Scientific Reports*, *8*(1), 4021, doi:10.1038/s41598-018-22310-z.

Kimmritz, M., S. Danilov, and M. Losch (2016), The adaptive EVP method for solving the sea ice momentum equation, *Ocean Modelling*, *101*, 59 – 67, doi:https://doi.org/10.1016/j.ocemod.2016.03.004.

Koldunov, N. V., S. Danilov, D. Sidorenko, N. Hutter, M. Losch, H. Goessling, N. Rakowsky, P. Scholz, D. Sein, Q. Wang, and T. Jung (2019), Fast EVP Solutions in a High-Resolution Sea Ice Model, *Journal of Advances in Modeling Earth Systems*, *11*(5), 1269–1284, doi:10.1029/2018MS001485.

Kozo, T. L. (1983), Initial model results for Arctic mixed layer circulation under a refreezing lead, *Journal of Geophysical Research: Oceans*, *88*(C5), 2926–2934, doi:10.1029/JC088iC05p02926.

Kozo, T. L. (1991), The hybrid polynya at the northern end of Nares Strait, *Geophysical Research Letters*, *18*(11), 2059–2062, doi:10.1029/91GL02574.

Kubat, I., M. Sayed, S. Savage, and T. Carrieres (2006), Flow of Ice Through Converging Channels, *International Journal of Offshore and Polar Engineering*, *16*(4), 268–273.

Kwok, R. (2005), Variability of Nares Strait ice flux, *Geophysical Research Letters*, *32*(24), doi:10.1029/2005GL024768.

Kwok, R., and G. F. Cunningham (2010), Contribution of melt in the Beaufort Sea to the decline in Arctic multiyear sea ice coverage: 1993-2009, *Geophysical Research Letters*, *37*(20), n/a–n/a, doi:10.1029/2010GL044678.

Kwok, R., E. C. Hunke, W. Maslowski, D. Menemenlis, and J. Zhang (2008), Variability of sea ice simulations assessed with RGPS kinematics, *Journal of Geophysical Research: Oceans*, *113*(C11), doi:10.1029/2008JC004783.

Laliberté, F., S. E. L. Howell, and P. J. Kushner (2016), Regional variability of a projected sea ice-free Arctic during the summer months, *Geophysical Research Letters*, *43*(1), 256–263, doi:10.1002/2015GL066855.

Langleben, M. (1962), Young's modulus for sea ice, *Canadian Journal of Physics*, *40*(1), 1–8.

Ledley, T. S. (1988), A coupled energy balance climate-sea ice model: Impact of sea ice and leads on climate, *Journal of Geophysical Research: Atmospheres*, *93*(D12), 15,919–15,932, doi:10.1029/JD093iD12p15919.

Lemieux, J.-F., B. Tremblay, S. Thomas, J. Sedláček, and L. A. Mysak (2008), Using the preconditioned Generalized Minimum RESidual (GMRES) method to solve the sea-ice momentum equation, *Journal of Geophysical Research*, *113*, C10,004, doi:10.1029/2007JC004680.

Lemieux, J.-f., D. A. Knoll, M. Losch, and C. Girard (2014), A second-order accurate in time IMplicit – EXplicit (IMEX) integration scheme for sea ice dynamics, *Journal of Computational Physics*, *263*, 375–392, doi:10.1016/j.jcp.2014.01.010.

Lemieux, J.-F., L. B. Tremblay, F. Dupont, M. Plante, G. C. Smith, and D. Dumont (2015), A basal stress parameterization for modeling landfast ice, *Journal of Geophysical Research: Oceans*, *120*, 3157–3173, doi:10.1002/2014JC010678.Received.

Lemieux, J.-F., F. Dupont, P. Blain, F. Roy, G. C. Smith, and G. M. Flato (2016), Improving the simulation of landfast ice by combining tensile strength and a parameterization for grounded ridges, *Journal of Geophysical Research: Oceans*, *121*(October), doi:10.1002/2016JC012006.

Lemieux, J.-F., J. Lei, F. Dupont, F. Roy, M. Losch, C. Lique, and F. Laliberté (2018), The Impact of Tides on Simulated Landfast Ice in a Pan-Arctic Ice-Ocean Model, *Journal of Geophysical Research: Oceans*, *123*, 1–16, doi:10.1029/2018JC014080.

Lemieux, J.-F., B. Tremblay, and M. Plante (2020), Toward a method for downscaling sea ice pressure, *The Cryosphere Discussions*, *2020*, 1–26, doi:10.5194/tc-2020-134.

Lewis, J. K. (1993), A model for thermally-induced stresses in multi-year sea ice, *Cold Regions Science and Technology*, *21*, 337–348.

Li, X., S. K. Krueger, C. Strong, G. G. Mace, and S. Benson (2020), Midwinter Arctic leads form and dissipate low clouds, *Nature Communications*, *11*(1), 206, doi:10.1038/s41467-019-14074-5.

Lieser, J. L. (2004), A numerical model for short-term sea ice forecasting in the Arctic, Ph.D. thesis, Universitat Bremen, Bremen, Germany.

Losch, M., D. Menemenlis, J.-M. Campin, P. Heimbach, and C. Hill (2010), On the formulation of sea-ice models. Part 1: Effects of different solver implementations and parameterizations, *Ocean Modelling*, *33*(1), 129 – 144, doi:https://doi.org/10.1016/j.ocemod.2009.12.008.

Lüpkes, C., T. Vihma, G. Birnbaum, and U. Wacker (2008), Influence of leads in sea ice on the temperature of the atmospheric boundary layer during polar night, *Geophysical Research Letters*, *35*(3), doi:10.1029/2007GL032461.

Macdonald, R. W. (2000), Arctic estuaries and ice: a positive-negative estuarine couple, in *The Freshwater Budget of the Arctic Ocean*, edited by E. Lewis, E. Jones, P. Lemke, T. Prowse, and P. Wadhams, pp. 383–407, Kluwer Academic Publishers, Dordrecht.

Mahoney, A., H. Eicken, A. G. Gaylord, and L. Shapiro (2007), Alaska landfast sea ice: Links with bathymetry and atmospheric circulation, *Journal of Geophysical Research*, *112*(C2), C02,001, doi:10.1029/2006JC003559.

Mahoney, A. R., H. Eicken, A. G. Gaylord, and R. Gens (2014), Landfast sea ice extent in the Chukchi and Beaufort Seas: The annual cycle and decadal variability, *Cold Regions Science and Technology*, doi:10.1016/j.coldregions.2014.03.003.

Main, I. G. (2000), A damage mechanics model for power-law creep and earthquake aftershock and foreshock sequences, *Geophysical Journal International*, *142*(1), 151–161, doi:10.1046/j.1365-246x.2000.00136.x.

Marko, J. R., and R. E. Thomson (1977), Rectilinear leads and internal motions in the ice pack of the western Arctic Ocean, *Journal of Geophysical Research (1896-1977)*, *82*(6), 979–987, doi:10.1029/JC082i006p00979.

Martin, S., and D. Cavalieri (1989), Contributions of the Siberian Shelf Polynyas to the Arctic Ocean Intermediate and Deep Water, *Journal of Geophysical Research*, *94*(C9), 12,725–12,738.

Matsumura, Y., and H. Hasumi (2008), Brine-Driven Eddies under Sea Ice Leads and Their Impact on the Arctic Ocean Mixed Layer, *Journal of Physical Oceanography*, *38*(1), 146–163, doi:10.1175/2007JPO3620.1.

Maykut, G. A. (1982), Large-scale heat exchange and ice production in the central Arctic, *Journal of Geophysical Research: Oceans*, *87*(C10), 7971–7984, doi:10.1029/JC087iC10p07971.

Maykut, G. A., and N. Untersteiner (1971), Some results from a time-dependent thermodynamic model of sea ice, *Journal of Geophysical Research (1896-1977)*, *76*(6), 1550–1575, doi:10.1029/JC076i006p01550.

McPhee, M. G. (1979), The effect of the oceanic boundary layer on the mean drift of pack ice: application of a simple model, *Journal of Physical Oceanography*, *9*, 388–400.

Melling, H. (2002), Sea ice of the northern Canadian Arctic Archipelago, *Journal of Geophysical Research*, *107*(C11), 3181, doi:10.1029/2001JC001102.

Mohr, O. (1900), Welche Umstände bedingen die Elastizitätsgrenze und den Bruch eines Materials, *Zeitschrift des Vereins Deutscher Ingenieure*, *46*, 1572–1577.

Moore, G. W. K., and K. McNeil (2018), The Early Collapse of the 2017 Lincoln Sea Ice Arch in Response to Anomalous Sea Ice and Wind Forcing, *Geophysical Research Letters*, *45*(16), 8343–8351, doi:10.1029/2018GL078428.

Murakami, S. (2012), Continuum damage mechanics : a continuum mechanics approach to the analysis of damage and fracture, doi:10.1007/978-94-007-2666-6.

Mussells, O., J. Dawson, and S. Howell (2017), Navigating pressured ice: Risks and hazards for winter resource-based shipping in the Canadian Arctic, *Ocean and Coastal Management*, *137*, 57 – 67, doi:https://doi.org/10.1016/j.ocecoaman.2016.12.010.

Mysak, L. A., and F. Huang (1992), A Latent-and Sensible-Heat Polynya Model for the North Water, Northern Baffin Bay, *Journal of Physical Oceanography*, *22*(6), 596–608, doi:10.1175/1520-0485(1992)022⟨0596:ALASHP⟩2.0.CO;2.

National Ice Center, . (2006, updated 2009), National Ice Center Arctic sea ice charts and climatologies in gridded format, Edited and compiled by F. Fetterer and C. Fowley. Boulder, Colorado USA: National Snow and Ice Data Center, http//dx.doi.org/10.7265/N5X34VDB.

Nürnberg, D., I. Wollenburg, D. Dethleff, H. Eicken, H. Kassens, T. Letzig, E. Reimnitz, and J. Thiede (1994), Sediments in Arctic sea ice: Implications for entrainment, transport and release, *Marine Geology*, *119*(3-4), 185–214, doi:10.1016/0025-3227(94)90181-3.

Olason, E. (2016), A dynamical model of Kara Sea land-fast ice, *Journal of Geophysical Research: Oceans*, *121*(5), 3141–3158, doi:10.1002/2016JC011638.

Pfirman, S., R. Colony, D. Nürnberg, H. Eicken, and I. Rigor (1997), Reconstructing the origin and trajectory of drifting Arctic sea ice, *Journal of Geophysical Research*, *102*(C6), 575–586.

Pizzolato, L., S. E. L. Howell, J. Dawson, F. Laliberté, and L. Copland (2016), The influence of declining sea ice on shipping activity in the Canadian Arctic, *Geophysical Research Letters*, *43*(23), 12,146–12,154, doi:10.1002/2016GL071489.

Plante, M., and B. Tremblay (2020), A generalized stress correction scheme for the MEB rheology: impacts on sea-ice fracture angles and deformations, *To be submitted to The Cryospher Discussion*.

Plante, M., B. Tremblay, M. Losch, and J.-F. Lemieux (2020), Landfast sea ice material properties derived from ice bridge simulations using the Maxwell elasto-brittle rheology, *The Cryosphere*, *14*(6), 2137–2157, doi:10.5194/tc-14-2137-2020.

Pritchard, R. S. (1988), Mathematical characteristics of sea ice dynamics models, *Journal of Geophysical Research: Oceans*, *93*(C12), 15,609–15,618, doi:10.1029/JC093iC12p15609.

Rampal, P., S. Bouillon, E. Ólason, and M. Morlighem (2016), neXtSIM: a new Lagrangian sea ice model, *The Cryosphere*, *10*(3), 1055–1073, doi:10.5194/tc-10-1055-2016.

Rampal, P., V. Dansereau, E. Olason, S. Bouillon, T. Williams, and A. Samaké (2019), On the multi-fractal scaling properties of sea ice deformation, *The Cryosphere Discussions*, *2019*, 1–45, doi:10.5194/tc-2018-290.

Rasmussen, T., K. Nicolai, and E. Kaas (2010), Modelling the sea ice in the Nares Strait, *Ocean Modelling*, *35*(3), 161–172, doi:10.1016/j.ocemod.2010.07.003.

Reimnitz, E., L. Toimil, and P. Barnes (1978a), Arctic continental shelf morphology related to sea-ice zonation, Beaufort Sea, Alaska, *Marine Geology*, *28*, 179–210.

Reimnitz, E., L. J. Toimil, and P. W. Barnes (1978b), Stamukhi Zone Processes: Implications for Developing the Arctic Offshore Area, *Journal of Petroleum Technology*, *30*(07), 982–986, doi:10.2118/6945-PA.

Reimnitz, E., D. Dethleff, and D. Nürnberg (1994), Contrasts in Arctic shelf sea-ice regimes and some implications :, *Marine Geology*, *119*, 215–225.

Reimnitz, E., H. Eicken, T. Martin, and E. R. K. Reimnitz (1995), Multiyear Fast Ice along the Taymyr Peninsula, Siberia, *48*(4), 359–367.

Rice, J. R. (2010), *Solid Mechanics*, Harvard University 2010.

Richter-Menge, J. A., and B. Elder (1998), Characteristics of pack ice stress in the Alaskan Beaufort Sea, *Journal of Geophysical Research*, *103*(98), 21,817–21,829.

Richter-Menge, J. A., S. L. McNutt, J. E. Overland, and R. Kwok (2002), Relating arctic pack ice stress and deformation under winter conditions, *Journal of Geophysical Research: Oceans*, *107*(C10), SHE 15–1–SHE 15–13, doi:10.1029/2000JC000477.

Ringeisen, D., M. Losch, L. B. Tremblay, and N. Hutter (2019), Simulating intersection angles between conjugate faults in sea ice with different viscous–plastic rheologies, *The Cryosphere*, *13*(4), 1167–1186, doi:10.5194/tc-13-1167-2019.

Ringeisen, D., L. B. Tremblay, and M. Losch (2020), Non-normal flow rules affect fracture angles in sea ice viscous-plastic rheologies, *The Cryosphere Discussions*, *2020*, 1–24, doi:10.5194/tc-2020-153.

Roscoe, K. H. (1970), The Influence of Strains in Soil Mechanics, *Géotechnique*, *20*(2), 129–170, doi:10.1680/geot.1970.20.2.129.

Rozman, P., J. A. Hölemann, T. Krumpen, R. Gerdes, C. Köberle, T. Lavergne, S. Adams, and F. Girard-Ardhuin (2011), Validating satellite derived and modelled sea-ice drift in the Laptev Sea with in situ measurements from the winter of 2007/2008, *Polar Research*, *30*(1), 7218, doi:10.3402/polar.v30i0.7218.

Ryan, P. A., and A. Münchow (2017), Sea ice draft observations in Nares Strait from 2003 to 2012, *Journal of Geophysical Research: Oceans*, *122*(4), 3057–3080, doi:10.1002/2016JC011966.

Schreyer, H. L., D. L. Sulsky, L. B. Munday, M. D. Coon, and R. Kwok (2006), Elastic-decohesive constitutive model for sea ice, *Journal of Geophysical Research: Oceans*, *111*(11), C11S26, doi:10.1029/2005JC003334.

Schulkes, R. M. S. M. (1995), A Note on the Evolution Equations for the Area Fraction and the Thickness of a Floating Ice Cover, *J. Geophys. Res.*, *100*(C3), 5021–5024.

Schulson, E. M. (2004), Compressive shear faults within arctic sea ice: Fracture on scales large and small, *Journal of Geophysical Research: Oceans*, *109*(C7), doi:10.1029/2003JC002108.

Schulson, E. M., a. L. Fortt, D. Iliescu, and C. E. Renshaw (2006), Failure envelope of first-year Arctic sea ice: The role of friction in compressive fracture, *Journal of Geophysical Research: Oceans*, *111*(11), C11S25, doi:10.1029/2005JC003235.

Selyuzhenok, V., T. Krumpen, A. Mahoney, M. Janout, and R. Gerdes (2015), Seasonal andinterannual variability of fast ice extent in the southeastern Laptev Sea between 1999 and 2013, *Journal of Geophysical Research: Oceans*, *120*, 7791–7806, doi:10.1002/2015JC011135.Received.

Selyuzhenok, V., A. Mahoney, T. Krumpen, G. Castellani, and R. Gerdes (2017), Mechanisms of fast-ice development in the south-eastern Laptev Sea: a case study for winter of 2007/08 and 2009/10, *Polar Research*, *36*(1), 1411,140, doi:10.1080/17518369.2017.1411140.

Shroyer, E. L., R. M. Samelson, L. Padman, and A. Münchow (2015), Modeled ocean circulation in Nares Strait and its dependence on landfast-ice cover, *Journal of Geophysical Research: Oceans*, *120*(12), 7934–7959, doi:10.1002/2015JC011091.

Sodhi, D. S. (1997), Ice arching and the drift of pack ice through restricted channels, *Cold Regions Research and Engineering Laboratory (CRREL) Rep. 77-18*, p. 11 pp.

Stern, H. L., D. A. Rothrock, and R. Kwok (1995), Open water production in Arctic sea ice: Satellite measurements and model parameterizations, *Journal of Geophysical Research: Oceans*, *100*(C10), 20,601–20,612, doi:10.1029/95JC02306.

Sukhorukov, K. (1996), Experimental investigations of relaxation properties of sea ice internal stresses, in *The proceedings of the sixth (1996) international offshore and polar engineering conference*, pp. 354–361.

Sulsky, D., and K. Peterson (2011), Toward a new elastic – decohesive model of Arctic sea ice, *Physica D Nonlinear Phenomena*, *240*(20), 1674–1683, doi:10.1016/j.physd.2011.07.005.

Sulsky, D., H. Schreyer, K. Peterson, R. Kwok, and M. Coon (2007), Using the material-point method to model sea ice dynamics, *Journal of Geophysical Research*, *112*, C02S90, doi:10.1029/2005JC003329.

Tabata, T. (1955), A measurement of Visco-Elastic Constants of Sea Ice, *Journal of the Oceanographical Society of Japan*, *11*(4), 185–189.

Tang, C. (1997), Numerical simulation of progressive rock failure and associated seismicity, *International Journal of Rock Mechanics and Mining Sciences*, *34*(2), 249 – 261, doi: https://doi.org/10.1016/S0148-9062(96)00039-3.

Timco, G. W., and W. F. Weeks (2010), A review of the engineering properties of sea ice, *Cold Regions Science and Technology*, *60*(2), 107–129, doi:10.1016/j.coldregions.2009.10.003.

Tran, H. D., D. L. Sulsky, and H. L. Schreyer (2015), An anisotropic elastic-decohesive constitutive relation for sea ice, *International Journal for Numerical and Analytical Methods in Geomechanics*, *39*(February), 988–1013, doi:10.1002/nag.

Tremblay, L.-B., and M. Hakakian (2006), Estimating the Sea Ice Compressive Strength from Satellite-Derived Sea Ice Drift and NCEP Reanalysis Data, *Journal of Physical Oceanography*, *36*(11), 2165–2172.

Tremblay, L.-B., and L. A. Mysak (1997), Modeling Sea Ice as a Granular Material , Including the Dilatancy Effect, *Journal of Physical Oceanography*, *27*, 2342–2360.

Tucker, W. B., and D. K. Perovich (1992), Stress measurements in drifting pack ice, *Cold Regions Science and Technology*, *20*, 119–139.

Turnbull, I. D., R. Z. Torbati, and R. S. Taylor (2017), Relative influences of the metocean forcings on the drifting ice pack and estimation of internal ice stress gradients in the Labrador Sea, *Journal of Geophysical Research: Oceans*, *122*(7), 5970–5997, doi:10.1002/2017JC012805.

Vardoulakis, I. (1980), Shear band inclination and shear modulus of sand in biaxial tests, *International Journal for Numerical and Analytical Methods in Geomechanics*, *4*(2), 103–119, doi:10.1002/nag.1610040202.

Vihma, T. (2014), Effects of Arctic Sea Ice Decline on Weather and Climate: A Review, *Surveys in Geophysics*, *35*(5), 1175–1214, doi:10.1007/s10712-014-9284-0.

Vincent, R. F. (2019), A Study of the North Water Polynya Ice Arch using Four Decades of Satellite Data, *Scientific Reports*, *9*(1), 20,278, doi:10.1038/s41598-019-56780-6.

Wang, J., K. Mizobata, X. Bai, H. Hu, M. Jin, Y. Yu, M. Ikeda, W. Johnson, W. Perie, and A. Fujisaki (2014), A modeling study of coastal circulation and landfast ice in the nearshore Beaufort and Chukchi seas using CIOM, *Journal of Geophysical Research: Oceans*, *119*(6), 3285–3312, doi:10.1002/2013JC009258.

Wang, K. (2007), Observing the yield curve of compacted pack ice, *Journal of Geophysical Research: Oceans*, *112*(C5), doi:10.1029/2006JC003610.

Wang, M., and J. E. Overland (2012), A sea ice free summer Arctic within 30 years: An update from CMIP5 models, *Geophysical Research Letters*, *39*(18), doi:10.1029/2012GL052868.

Weeks, W. F., and A. Assur (1967), The mechanical properties of sea ice, *Cold Regions Science and Engineering*, *II*(Section C).

Weiss, J., E. M. Schulson, and H. L. Stern (2007), Sea ice rheology from in-situ , satellite and laboratory observations : Fracture and friction, *Earth and Planetary Science Letters*, *255*, 1–8, doi:10.1016/j.epsl.2006.11.033.

Wilchinsky, A. V., and D. L. Feltham (2004), A continuum anisotropic model of sea-ice dynamics, *Proceedings of the Royal Society of London. Series A: Mathematical, Physical and Engineering Sciences*, *460*(2047), 2105–2140, doi:10.1098/rspa.2004.1282.

Wilchinsky, A. V., H. D. B. S. Heorton, D. L. Feltham, and P. R. Holland (2015), Study of the Impact of Ice Formation in Leads upon the Sea Ice Pack Mass Balance Using a New Frazil and Grease Ice Parameterization, *Journal of Physical Oceanography*, *45*(8), 2025–2047, doi:10.1175/JPO-D-14-0184.1.

Williams, J., L. B. Tremblay, and J.-f. Lemieux (2017), The effects of plastic waves on the numerical convergence of the viscous – plastic and elastic – viscous – plastic sea-ice models, *Journal of Computational Physics*, *340*, 519–533, doi:10.1016/j.jcp.2017.03.048.

Yu, Y., H. Stern, C. Fowler, F. Fetterer, and J. Maslanik (2014), Interannual Variability of Arctic Landfast Ice between 1976 and 2007, *Journal of Climate*, *27*, 227–243, doi: 10.1175/JCLI-D-13-00178.1.

Zhang, J., and W. D. Hibler (1997), On an efficient numerical method for modeling sea ice dynamics, *Journal of Geophysical Research*, *102*(C4), 8691–8702.